Departament d'Enginyeria Electrònica
UNIVERSITAT POLITÈCNICA DE CATALUNYA

"SURFACE PASSIVATION OF CRYSTALLINE SILICON BY AMORPHOUS SILICON CARBIDE FILMS FOR PHOTOVOLTAIC APPLICATIONS"

Tesi doctoral presentada per a l'obtenció
del títol de Doctor

Rafel Ferré i Tomàs

Co-directors: Ramon Alcubilla González
Michael Vetter

Gener 2008

Acknowledgements

I would like to thank to my supervisor, Ramon Alcubilla, for introducing me in the solar cells field. He has been always available, at any time, teaching, discussing and helping. I cannot express all my gratitude to him for everything he did for me. Michael Vetter, also my supervisor, spent many hours with me inside the clean room and brought me several times to Germany, where I could widen my vision of solar cells technology. Isidro, Pablo and Albert worked hard, but also spent, like Stephanie, Cristóbal, Kim, Sandra, and Servane, nice moments during these last four years. And of course, I need to mention Moisés, Jordi, David, Delfina, Gerard, Ivaldo, Loreto, Lukasz, Mónica and all the others (many) who shared as PhD students uncertainties about future, discussions, experiences and a nice climate office. I cannot forget our clean room technicians: Miguel, Xavi, Javi and Juan Carlos.

I am extremely grateful to Andres Cuevas for hosting me in his group at the ANU, Canberra, and also for his patience at my uncountable amount of questions. There I met many interesting people like Derk, Dan, Jason, Evan, Helmut, and specially Fede, who was an excellent teacher, colleague and friend. To him I also acknowledge the collaboration of his group at the EHU, Bilbao, led by Juan Carlos Gimeno. Thorsten Trupke and Robert Bardos, from UNSW, Sydney, provided photoluminescence measurements of silicon carbide passivated samples.

I also would like to express my acknowledgement to Jan Schmidt for hosting me at the ISFH, Hameln, and for his always very interesting comments. Also from ISFH thanks to Robert Bock, who provided ECV measurements, Barbara Terheiden, who reviewed the manuscript of the present thesis, and Karsten Bothe, for help in corona charge measurements. And to all the technicians, who kindly offered his help at any time with extreme professionalism. Quique became a good friend sharing nice discussions, not always about science, which were specially helpful for somebody who does not speak German, yet.

Thanks to Stefan Glunz and his group in ISE, Freiburg, whose collaboration let us achieve together the first 20% efficient solar cell with silicon carbide rear side passivation. Thanks to Pere Roca i Cabarrocas and Jérôme Damon-Lacoste, from LPICM, École Politechnique, Paris, for ellipsometry measurements. Thanks to Jordi Andreu and his group at UB, Barcelona, for offering his collaboration and to Jordi Escarré for simulations of optical measurements. Also at UB I left many friends, like Olga and Andreu.

Apart from the professional help, I would like to express my acknowledgement to all my family, specially my mother, but also my father, sister, brother in law and Alex, who was born just when this thesis started. To all my friends in Amposta and now, from many places in the world, in all sincerity: gràcies! And the last, but for me the most important one: thanks Rita for sharing these moments with me.

This work was funded by the Spanish Ministry of Education and Science under contracts TIC2002-04184-C02-01 and TEC2005-02716/MIC.

Abstract

During the last two decades the photovoltaic market has rapidly increased, partly because of a new vision of solar energy as a useful and competitive source of electricity production and partly because of the reduction of manufacture costs while keeping efficiencies high. Crystalline silicon solar cells are the most widely studied cells and up to date they offer one of the best performances in terrestrial applications. The key issue of cost reduction in these cells is the reduction of silicon costs, by using thinner substrates and/or by working with solar-grade low-cost silicon material. In both cases reduction of recombination of charge carriers at the surface, what is called surface passivation, is compulsory to achieve the high efficencies (> 20%) expected.

The state of the art in surface passivation is done by thin films of amorphous silicon nitride grow by Plasma Enhanced Chemical Vapour Deposition (PECVD). This material offers excellent surface passivation in most of the solar cell schemes and antireflective properties at the same time. Despite silicon nitride is very well established in photovoltaic field, in this thesis we offer an alternative that is based on *amorphous silicon carbide* (*a*-SiC), also grown by PECVD. The passivation properties of silicon carbide have been already studied in our group finding that excellent results can be obtained when the films are rich in silicon, especially for those doped with phosphorus to form a *n*-type material. Because this feature leads to undesirable absorption of solar light within the films that does not contribute to the photocurrent, silicon carbide would then be relegated to passivate only the rear side of the solar cell.

The aim of this work is to improve surface passivation properties developed previously at UPC, and add compulsory requisites for the application of crystalline solar cells. These requisites are: uniformity, transparency and antireflective properties, stability under long term operation and stability under high temperature steps (allowing screen printing processes). Also it is the willing to provide a better understanding of the fundamental properties of these films.

The main results achieved are enumerated hereafter:

- Surface passivation improves with the film thickness and then saturates for films thicker than 50 nm. The mechanism responsible for this improvement is not an increase of the electric charge in the film, as in principle could be thought, but a

better saturation of defects by the presence of hydrogen. The amount of charge density seems to be independent of the film.

- Experiments of corona charge reveal some treats about the nature of the charge density to provide the field effect passivation. The origin of the charge seems to be a continuous density of states at the interface, rather a fixed charge allocated in the film.
- None of the attempts using carbon rich films, which are transparent and with antireflective properties, resulted in excellent surface passivation. Such attempts included variation of the deposition parameters, dilution of plasma with hydrogen, and introduction of nitrogen of in the phosphorus doped *a*-SiC films. Therefore, up to now it becomes apparent that it is a fundamental property of silicon carbide films the necessity to be rich in silicon to perform surface passivation.
- The way to combine surface passivation and antireflective properties was applying stacks of different *a*-SiC layers: one silicon rich and one carbon rich. The thickness of the silicon rich layer was optimized to reach a trade-off between passivation and lost of photocurrent due to the absorption in the film. The stacks were used to passivate *p*-type bases, with reasonably good results, and n^+-type emitters, with very good results.
- A new material was tested: a ternary alloy of silicon, carbon and nitrogen doped with phosphorus. This material was applied to *n*- and *p*-type bases and n^+-type emitters, presenting the best results in surface passivation achieved by our group, and comparable to surface passivation record achieved by amorphous silicon carbide. Best composition was rich in silicon, and again the use stacks of silicon rich and carbon rich films was combined successfully.
- Stability against thermal processes was tested on different passivation schemes. After the treatment, the passivation is strongly reduced for single silicon rich films, which were offering good initial results. On the other hand, the stacks with a second carbon rich film maintain reasonably well the surface passivation properties.
- The good dielectric properties of the carbon rich films, not provided by the silicon rich ones, resulted crucial to perform the first silicon solar cell with *a*-SiC rear side passivation with efficiencies above 20%.

Table of contents

Introduction

There are two reasons for which I started research in photovoltaics. First, I enjoy research and developing new ideas. Second, I was really hoping to contribute, even though it was with the smallest thing, to something beneficial for the environment. This idea was honest (and still is nowadays) when many years ago I wanted to believe those who claimed that solar could be more than an exotic and curious way of producing energy. Actually, in his essay about global-solar economy, Hermann Scheer sees the use of all renewable energies concepts as the *only way* to get rid of the fossil resources dependence, which will extinguish sooner than later, but also as a way to keep the same quality of life for all people [1].

Today the old prejudices about photovoltaic solar energy have been put aside and it is widely recognized that it can more than fulfil all the requirements of electrical energy in the whole world. The governments of countries have created subventions to promote the use of solar electricity and the photovoltaic industries have extraordinarily grown to cover the big incoming demand of solar modules. And they are still growing: it is believed that by 2010 there will be factories able to produce a number of solar modules per year which nominal solar power would be more than 1 Gigawatt [2]. Today a 100 Megawatt factory is considered a big factory. Solar is, then, on the way of being competitive to conventional energy sources. However, further reduction of the costs, high conversion efficiencies or both are still required to achieve this objective. In the following lines we explain how our research is directly related to this idea. We start from the basic description and operation of solar cells, and then we introduce the concept of surface passivation of crystalline silicon, the topic of this thesis.

A solar cell consists of the union of two semiconductor materials, one doped with donor impurities, which provide negative charge carriers or *electrons* (*n*-type doped) and the other doped with acceptor impurities, which provide positive charge carriers or *holes* (*p*-type doped). Any incident source of light with photon energy higher than the energy band gap of the bulk material will be absorbed, generating electrons and holes in excess inside the cell. These travel together until they reach the *p-n* junction, in which they are separated thus producing an electric current, or until they annihilate themselves in any recombination process. The ratio of separated charge carriers pairs to recombined carriers depends on the material as well as on every specific design of cell. To produce the highest possible electrical current it is required to maintain the recombination to a minimum. After separation in the junction, recombination can still occur if two carrier of different type meet again.

The wide variety of cell concepts existing can be grouped in three families according to the level of maturity achieved. Then, there are *first generation* solar cells, which gather those cells made of *crystalline* semiconductor materials, such as silicon or gallium arsenide, with a typical thickness of several hundreds of microns and high conversion efficiencies. *Second generation* gathers the so called *thin film* cells. Normally, they are made of *amorphous films* deposited on top of glass, with thicknesses less than 2 µm and much lower efficiencies than the first generation cells, although they can be produced at a much competitive price. Finally, *third generation* solar cells gather all new concepts that are still remaining in a laboratory level, such as organic solar cells or cells with nanocrystal structures. In the three generations the design can involve single junction (homo or heterojunctions) or multiple junction solar cells with different energy band gaps to seize a major part of the solar spectrum. Depending on the design they can operate under direct illumination or under concentrated light, what normally increase the cell efficiency.

Belonging to the first generation group we can find *crystalline silicon* solar cells. Under non-concentrated light conditions they offer the optimal trade-off between cell efficiency, simple performance and manufacturing costs. This is the reason why they still hold around 90% of the market. A record efficiency of 24.7% measured at *standard test* *conditions* was reached in 2001 by the University of New South Wales (UNSW) using the PERL concept [3]. The theoretical efficiency limit of a crystalline silicon solar cell under these conditions was calculated at 33%. A more realistic and practical limit was estimated at 29% [4]. We are not far then from the real limit, and it could be thought that the research on crystalline silicon solar cells is practically finished. However, a wide variety of new concepts, designs and crystalline silicon materials have been developed to achieve high efficiencies at low costs. In all cases reduction of the thickness of the silicon wafer thickness is compulsory to lower the costs, causing a strong recombination of carriers at the surfaces unless they are passivated. Surface passivation, then, becomes a key issue to achieve high conversion efficiencies in crystalline silicon solar cells.

In this thesis we explore surface passivation by means of amorphous silicon carbide films. This material is relatively new in solar cells, and probably it will still take some time before breaking through the photovoltaic industry. In this work some issues are addressed with the aim to help to shorten the way of silicon carbide towards real applications. Those are the study of passivation of low resistive wafers and emitters, the use of transparent layers to be applied at the sunned side of the cell and the study of the stability under thermal processes.

Chapter 1 reviews recombination mechanisms in crystalline silicon, surface passivation strategies and the method to characterize both by measuring the lifetime of minority carriers. Chapter 2 reviews the most important materials that are state of the art of surface passivation, such as silicon oxide, amorphous silicon and silicon nitride, as well as the previous results achieved by silicon carbide. Chapter 3, 4, and 5 discuss the development of different types of amorphous silicon carbide and their application to bases and emitters. Also, information about fundamental properties of the material is provided. Chapter 6 analyzes extensively the stability of silicon carbide with time and under a wide variety of thermal processes. Finally, Chapter 7 summarizes the principal results obtained and suggests further work to improve the capabilities of silicon carbide.

CHAPTER 1

Recombination and surface passivation in crystalline silicon

1.1 Introduction

In crystalline silicon generation of charge carriers in excess, electrons and holes, is provided by thermal activity, electrical excitation, or light excitation. Opposite to this generation there is the recombination of such carriers, in which the annihilation of electrons and holes is assisted by several mechanisms. The rate at which this electrons and holes are annihilated, i.e., the recombination rate, is defined by the relation:

$$U = \frac{\Delta n}{\tau} \tag{1.1}$$

where Δn is the density of carrier in excess per unit volume (or excess carrier density) and τ is the lifetime of such carriers.

It is an objective of the solar cell development to minimize all recombination processes, so that the light generated carriers increase their contribution to the photocurrent. In other words, the *conversion efficiency* of the solar cell is increased when the recombination of photogenerated carriers decreases. Such conversion efficiency depends strongly on the spectrum, illumination intensity and the device temperature. Therefore, it is very useful to define the measurement conditions in order to compare the properties of different cells. The *standard test conditions* are defined by the AM1.5D or AM1.5G solar spectra with a device temperature of 25 °C. Spectrum AM1.5 refers to the illumination provided by the sunlight at the sea level under specific conditions [5]. The index D indicates that only the direct light coming from the sun is used, while the index G stands for the spectrum taking into account the diffuse light, too. The AM1.5G spectrum is also known as 1 sun illumination and it will be used in this thesis frequently.

Between the three fundamental recombination processes present in semiconductors, two of them are intrinsic and therefore they are unavoidable. The third one is related to the presence of defects, present majorly at the surface of the material. Surface passivation will be presented in this thesis as the strategy to reduce recombination at the surface to have a large positive impact to the solar cells performance.

In this Chapter we review the recombination mechanisms in silicon and the strategies for surface passivation. Then, methods for lifetime measurements will be introduced as a powerful tool for characterization of recombination and surface passivation in crystalline silicon.

1.2 Recombination mechanisms in silicon

Three fundamental recombination mechanisms occur in semiconductors:

(1) Band to band radiative recombination
(2) Auger recombination
(3) Recombination through defects in the bandgap

The two first mechanisms depend only on the concentration of free carriers (electrons and holes) present in the bulk silicon, while the third one is explicitly dependent on the number of defects. Therefore, at given doping density and illumination level mechanisms (1) and (2) are inherent to the silicon properties, and the only way to reduce the total recombination is by reducing the number of defects during the manufacture process. The free carrier concentration are given by:

$$n \equiv n_0 + \Delta n \approx N_D + \Delta n \quad \text{for } n\text{-type material} \tag{1.2.a}$$

$$p \equiv p_0 + \Delta p \approx N_A + \Delta p \quad \text{for } p\text{-type material} \tag{1.2.b}$$

where n_0, p_0 are the electron and hole concentrations at equilibrium, N_D, N_A, the donor and acceptor densities, and Δn, Δp, the excess carrier densities (also called injection densities, or injection level) for electron and holes, respectively. In the absence of trapping effects or any electric field both excess carrier densities, for electron and holes, are equal, since generation involves the creation of electron-hole pairs, i.e. $\Delta n = \Delta p$.

1.2.1 Radiative recombination

Radiative recombination is the inverse process of optical generation. The annihilation of an electron-hole pair leads to the creation of a photon with an energy close to the bandgap energy (see Fig 1.1). It depends directly on the availability of electrons and holes and it is given by:

$$U_{rad} = B\left(n\,p - n_i^2\right) \tag{1.3}$$

where B is the coefficient of radiative recombination and n_i is the intrinsic carrier concentration. Since silicon is an indirect bandgap semiconductor, the process must be assisted by a phonon to simultaneously conserve energy and momentum. Therefore the process involves four particles (two charge carriers, one photon and one phonon) and has a low probability of occurring. This causes a low value of B, which is calculated to be 2×10^{-15} cm^3 s^{-1} by [6,7] at 300 K. However, experimental determinations indicate a significant higher value, $B = 9.5 \times 10^{-15}$ cm^3 s^{-1} [8] or 1.1×10^{-14} cm^3 s^{-1} [9]. The discrepancy may be attributed to the use of a value of n_i higher than accepted in the calculations [10]. Also excitonic effects are not taken into account in such calculations and are thought to enhance the recombination rate, being this manifested in a higher value of B.

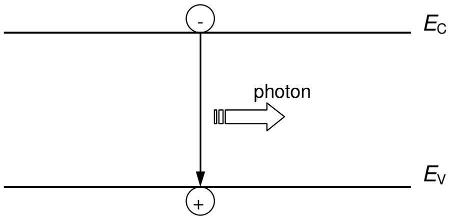

Figure 1.1. Radiative recombination

Another issue to take into account is that the radiation emitted during recombination can be reabsorbed before escaping from the silicon, thus the radiative recombination is slightly inferior than predicted. This effect, called *photon recycling*, is especially manifested in direct bandgap semiconductors and provokes a decrease of the radiative coefficient B. In silicon, it is commonly accepted to use the value $B = 2 \times 10^{-15}$ cm^3 s^{-1} [4].

Combining equations (1.1) to (1.3), it is possible to define the radiative lifetime for each doping type at low and high injection conditions, respectively:

$$\tau_{rad,li} = \frac{1}{B\,N_{dop}} \tag{1.4.a}$$

$$\tau_{rad,hi} = \frac{1}{B\,\Delta n} \tag{1.4.b}$$

where N_{dop} refers to the density of donor (N_{D}) or acceptor (N_{A}) atoms for n-type or p-type silicon. Hence, radiative lifetime is kept constant at low injection density and is inversely proportional to the excess carrier density at high injection level.

Despite the analysis of solar cells is usually performed at 300 K, it is important to note that the radiative recombination is temperature depending through the coefficient B. Such dependence has been explored widely in the literature [8,11-13]. It is also well known that B is enhanced by the Coulombic attraction between electrons and holes, and decreases with both the injection and the dopant density. Recently, Altermatt *et al.* [14] have provided theoretical calculations for such temperature and carrier densities dependencies. In their model, the Debye potential was incorporated to describe the screening effects between electrons and holes. Band to band radiative recombination is the weakest mechanism in silicon and can be masked by the other two, especially Auger recombination at high injection conditions. For our calculations, it is a good approximation to use a constant value of $B = 2 \times 10^{-15}$ cm^3 s^{-1}.

1.2.2 Auger recombination

1.2.2.1 Basic model for Auger recombination

Auger recombination is a process involving three particles, one electron and two holes, or vice-versa. The excess energy resulting from the band to band recombination between an electron and a hole is transferred to a third carrier [15], as shown in Fig 1.2. In its simplest analysis, the carriers are assumed to be non-interactive free particles [16]. The two recombination processes (*electron-electron-hole* and *electron-hole-hole*) are proportional to the carrier densities:

$$U_{eeh} = C_n\left(n^2 p - n_0^{\ 2} p_0\right) \tag{1.5.a}$$

$$U_{ehh} = C_p\left(np^2 - n_0 p_0^{\ 2}\right) \tag{1.5.b}$$

being the total Auger recombination:

$$U_{Auger} = U_{eeh} + U_{ehh} = C_n\left(n^2 p - n_0^{\ 2} p_0\right) + C_p\left(np^2 - n_0 p_0^{\ 2}\right) \tag{1.6}$$

where C_n and C_p are the so-called Auger coefficients. Neglecting $n_0^2p_0$ and $n_0p_0^2$ the corresponding lifetime can be written as:

$$\tau_{Aug} = \frac{1}{\left[C_n (N_D + \Delta n)^2 + C_p (N_D + \Delta n)\Delta n\right]} \qquad \text{for } n\text{-type } c\text{-Si} \tag{1.7.a}$$

$$\tau_{Aug} = \frac{1}{\left[C_n (N_A + \Delta n)\Delta n + C_p (N_A + \Delta n)^2\right]} \qquad \text{for } p\text{-type } c\text{-Si} \tag{1.7.b}$$

At low injection level densities the Auger lifetime depends on the square doping density as ($\tau_{\text{Auger}} \sim 1/N_{\text{dop}}^2$):

$$\tau_{Auger,low} = \frac{1}{C_n N_D^{\ 2}} \qquad \text{for } n\text{-type } c\text{-Si} \tag{1.8.a}$$

$$\tau_{Auger,low} = \frac{1}{C_p N_A^{\ 2}} \qquad \text{for } p\text{-type } c\text{-Si} \tag{1.8.b}$$

but it is independent on the excess carrier density. On the other hand, at high injection level range lifetime is only dependent on the square of the excess carrier density ($\tau_{\text{Auger}} \sim 1/\Delta n^2$), being independent on the doping density:

$$\tau_{Auger,high} = \frac{1}{C_a \Delta n^2} \qquad \text{for } n\text{- and } p\text{-type } c\text{-Si} \tag{1.9}$$

where C_a is the so-called ambipolar coefficient. Under the assumption of non interactive particles the ambipolar coefficient is defined as $C_a = C_n + C_p$. The most commonly employed values for the Auger coefficients are those determined by Dziewior and

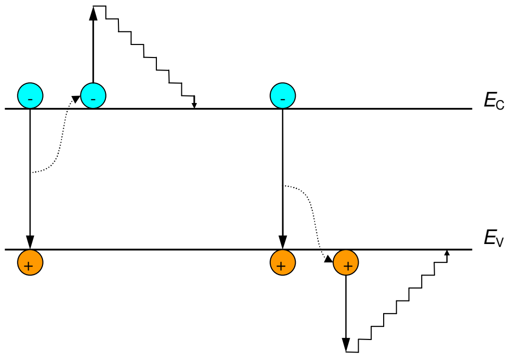

Figure 1.2. Auger recombination

Schmid [17], $C_n = 2.8\ 10^{-31}$ cm^6 s^{-1} and $C_p = 0.99\ 10^{-31}$ cm^6 s^{-1}, resulting in $C_a = 3.79\ 10^{-31}$ cm^6 s^{-1}. These values were taken from the fittings of lifetime measurements ($\tau \sim 1/N_{dop}^{2}$) of highly doped *n* and *p*-type wafers at low injection densities, and are valid for $N_{dop} > 5 \times 10^{18}$ cm^{-3}. Other authors also report an inverse quadratic dependence between Auger lifetime and doping concentration for *n*-type [18] and *p*-type [19] silicon, valid for $N_{dop} > 10^{17}$ cm^{-3}.

1.2.2.2 Coulomb enhanced Auger recombination

For doping densities lower than 10^{17} cm^{-3} the measured recombination lifetime at low injection is lower than expected. Hangleiter and Häcker [15] relaxed the assumption of three non-interacting, quasi-free particles by considering Coulombic interaction between electron and holes, in which excitons are formed. The Auger recombination rate is strongly enhanced because of an increased density of electrons (holes) in the vicinity of a hole (electron). As the concentration of majority carriers increases this Coulomb-enhanced Auger recombination is weakened due to the screening between electron-hole interactions. The basic correction consists of incorporating the enhancement factors g_{eeh} and g_{ehh} at low injection densities:

$$\tau_{Auger,li} = \frac{1}{g_{eeh}\, C_n\, N_D^{\ 2}} \equiv \frac{1}{C_n^*\, N_D^{\ 2}} \qquad \text{for } n\text{-type } c\text{-Si} \qquad (1.10.a)$$

$$\tau_{Auger,li} = \frac{1}{g_{ehh}\, C_p\, N_D^{\ 2}} \equiv \frac{1}{C_p^*\, N_A^{\ 2}} \qquad \text{for } p\text{-type } c\text{-Si} \qquad (1.10.b)$$

Using the Auger coefficients of Dziewior and Schmid [17], Altermatt *et al.* [20] determined the g_{eeh} and g_{ehh} enhancement factors as a function of the doping densities at low level injection:

$$g_{eeh}(N_D) = 1 + 44\left\{1 - \tanh\left[\left(\frac{N_D}{5\cdot 10^{16}\,cm^{-3}}\right)^{0.34}\right]\right\} \tag{1.11.a}$$

$$g_{ehh}(N_A) = 1 + 44\left\{1 - \tanh\left[\left(\frac{N_A}{5\cdot 10^{16}\,cm^{-3}}\right)^{0.29}\right]\right\} \tag{1.11.b}$$

With the enhancement factors g_{eeh} and g_{ehh} included in the model, the Auger lifetime does not follow the quadratic dependence with the doping density. Actually, fits of experimental data for *n*-type silicon at low injection densities show that the exponent in N_{D} is significantly lower [21]:

$$\tau_{Auger,li} = \frac{1}{1.9\cdot 10^{-24}\, N_D^{1.65}} \tag{1.12}$$

At high injection densities there are also some discrepancies between the $1/n^2$ dependence predicted and the experimental evidences. Firstly, the measured value for the ambipolar coefficient C_{a} has been found to be larger than the sum of the low injection coefficients, $C_{\mathrm{n}} + C_{\mathrm{p}}$. Values of measured C_{a} range between 2.8×10^{-30} cm^6 s^{-1} and 1.9×10^{-30} cm^6 s^{-1} [22][23]. Secondly, C_{a} seems to decrease as the injection level increases [24].

1.2.2.3 General models for Auger lifetime

With the aim to provide a general determination of Auger lifetime valid for all doping densities at any injection level, some authors have suggested different models based on the Coulomb-enhanced effect:

Schmidt *et al.* [25] and Altermatt *et al.* [23] used the enhancement factors g_{eeh} and g_{ehh}. These factors were assumed to be dependent only on the screening behaviour of the charge carriers. This allowed them to replace the doping density in equation (1.11) by $n+p$. A good agreement is found for intermediately doped *p*-type silicon, though the Auger recombination rate is overestimated at low level injection for highly doped silicon. Moreover, this model has not been tested in *n*-type silicon.

The simulation tool PC1D [26] incorporates a model that fixes the Auger coefficients C_{n} and C_{p} for low injection conditions and the C_{a} for high injection conditions. Then, effective Auger coefficients are defined by weighting C_{a}, C_{n} and C_{p} with the doping densities and carrier densities to be employed in equation (1.8) and (1.9):

$$C_n^{eff} = C_{n,lli}\left(\frac{N_D}{N_D+p}\right)+\frac{C_a}{2}\left(\frac{p}{N_D+p}\right) \tag{1.13.a}$$

$$C_p^{eff} = C_{p,lli}\left(\frac{N_A}{N_A+n}\right)+\frac{C_a}{2}\left(\frac{n}{N_A+n}\right) \tag{1.13.b}$$

With the coefficients provided by the PC1D the Auger recombination rate tends to be underestimated. However, the user has the possibility to modify $C_{\mathrm{n,lli}}$, $C_{\mathrm{p,lli}}$ and C_{a}. In Chapter 5 we employ this option for the analysis of surface recombination velocity in *n*-type emitters.

From the model provided by PC1D, Glunz *et al.* incorporate corresponding enhancement factors and replace $C_{\mathrm{n,lli}}$, $C_{\mathrm{p,lli}}$ with $g_{\mathrm{eeh}}C_{\mathrm{n,lli}}$, $g_{\mathrm{ehh}}C_{\mathrm{p,lli}}$. The model tends however to underestimate the recombination rate at mid and high injection levels and overestimates it at very high injection level.

Up to now, the most complete parameterisation for the Auger recombination rate for all the injection level range, doping type, and doping level is that provided by Kerr and Cuevas [27,28]. The model is valid at 300 K. On the one hand, for the low injection level range, the highest experimental lifetime data from the literature are fitted with $1/n^{1.65}$ dependence for the doping density, with different fitting parameters for *n*- and *p*-type silicon. In this case, radiative recombination is assumed to be negligible, so that the lifetime is directly attributed to the Auger recombination. On the other hand, for high injection level range, the radiative recombination cannot be neglected, as its $1/n$ dependence becomes stronger as the excess carrier density increases. Therefore, this last is subtracted (equation (1.3) with $B = 9.5 \times 10^{-15}$ cm^3 s^{-1}) from the experimental lifetime data. Then, the parameterisation for the Auger lifetime at high injection densities is obtained, with $1/n^{1.8}$ dependence with the excess carrier density and with the same parameter for both material types. To provide a physical basis to the model, a complete parameterisation that considers a three-particle interaction, characteristic of Auger, is suggested:

$$U_{Auger} = np\left[C_1(n_0)n_0 + C_2(p_0)p_0 + C_3(\Delta n)\Delta n\right] \tag{1.14}$$

From the aforementioned data fitting at high and low injection level densities, this automatically leads to

$$U_{Auger} = np\left[1.8\times10^{-24}n_0^{0.65} + 6\times10^{-25}p_0^{0.65} + 3\times10^{-27}\Delta n^{0.8}\right] \tag{1.15}$$

As Auger and radiative recombination are intrinsic processes, it can be assumed that the total recombination rate in silicon is provided by the sum equations (1.3) and (1.15):

$$U_{intrinsic} = U_{Auger} + U_{rad} =$$

$$= np\left[1.8\times10^{-24} n_0^{0.65} + 6\times10^{-25} p_0^{0.65} + 3\times10^{-27}\Delta n^{0.8} + 9.5\times10^{-15}\right] \qquad (1.16)$$

In such model the radiative recombination is simply provided by a constant coefficient, not accounting for the Coulombic interaction that also occurs for this process. Nevertheless, the dependence is incorporated on the other terms of equation (1.16). The complete model provides an excellent determination for the intrinsic lifetime and its validity was tested carefully.

The intrinsic (Auger plus radiative) lifetime used in this thesis is that provided by Kerr parameterisation. The easiest way to implement it in any simulation tool is by the lifetime definition. Combining equations (1.1), (1.2) and (1.16), assuming that Δn = Δp and considering that the minority carrier density is equal to the excess carrier density, it follows

$$\frac{1}{\tau_{intrinsic}} = \left(N_D + N_A + \Delta n\right)\times$$

$$\times\left[1.8\times10^{-24} N_D^{0.65} + 6\times10^{-25} N_A^{0.65} + 3\times10^{-27}\Delta n^{0.8} + 2\times10^{-15}\right] \qquad (1.17)$$

This equation can be used for both wafer types by simply setting the corresponding doping density and leaving the other at zero. Note that we have changed the value of the last term of equation (1.17), which accounts the radiative recombination, from 9.5×10^{-15} in (1.16) to 2×10^{-15}. Doing this we take into account the photon recycling effect explained in section 1.2.1.

1.2.3 Recombination through defects. Shockley Read Hall theory

Imperfections in the crystalline silicon due to impurities, or crystallographic defects, such as vacancies and dislocations, produce a determined number of states within the bandgap that act as carrier *traps* for free electrons or holes. A free carrier trapped in the defect releases its excess energy by a multiphonon emission process, and can be either emitted again to its original band or recombine with an oppositely charged carrier. While the first process does not contribute to carrier recombination, the second one is a dominant mechanism in indirect bandgap semiconductors.

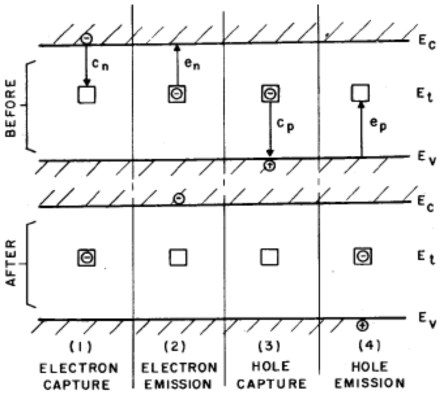

Figure 1.3. Fundamental interactions between electron, holes and defects centres to explain the Shockley Read Hall recombination process. Extracted from reference [29].

Figure 1.3 shows the four fundamental interactions between a defect centre and a charge: (1) capture of an electron, (2) emission of an electron, (3) capture of a hole and (4) emission of a hole. A recombination process occurs when step (1) and (3) or (2) and (4) take place. When the carrier is released into the same energy band where it was captured from (interaction (1) and (2) or (3) and (4)), the defect is called a *trap* and it does not contribute to carrier recombination.

The calculation of the net recombination rate was developed independently by Shockley and Read [30] and Hall [31] in the early 50's. The analysis is based on the probability of every possible interaction of the carrier with the defect. With the aim to reach an analytical solution some reasonable assumptions were made:

1. No radiative recombination or band-to-band Auger recombination.
2. The semiconductor is not degenerated.
3. The energy level of the defect does not change with its charge condition.
4. The relaxation time of the charge carriers caught by the defect is negligibly small compared to the average time between 2 emission processes.
5. The defect concentration is very small compared to the doping density.
6. Fermi-Dirac statistics apply.
7. The defects do not interact with each other.

Under these assumptions, the net recombination rate (U_{SRH}) for one trap located at an energy level of E_t is [30,31]:

$$U_{SRH} = \frac{v_{th} N_t (np - n_i^2)}{\frac{n + n_1}{\sigma_p} + \frac{p + p_1}{\sigma_n}} \tag{1.18.a}$$

$$n_1 = n_i \, e^{\frac{(E_t - E_i)}{kT}} \tag{1.18.b}$$

$$p_1 = n_i \, e^{\frac{(E_i - E_t)}{kT}} \tag{1.18.c}$$

where E_i is the intrinsic energy level, $\sigma_n(\sigma_p)$ are the capture cross sections of the defect for electons (holes), v_{th} is the thermal velocity of charge carriers (10^7 cm s^{-1} in *c*-Si at 300K) and N_t is the defect concentration per unit volume. It can be seen that under any injection conditions U_{SRH} is proportional to the defect density, as it was expected. In addition the capture cross sections σ_p and σ_n represents the efficiency of the defect to capture electrons and holes. Thus, the higher σ_p and σ_n value, the higher net recombination rate.

In order to express the SRH recombination rate by a recombination lifetime (τ_{SRH}), it is useful to define the so-called capture time constants τ_{n0} and τ_{p0} as:

$$\tau_{n0} \equiv \frac{1}{\sigma_n V_{th} N_t} \tag{1.19.a}$$

$$\tau_{p0} \equiv \frac{1}{\sigma_p V_{th} N_t} \tag{1.19.b}$$

Hence, assuming $\Delta n = \Delta p$ and applying equations (1.18) and (1.19) τ_{SRH} is:

$$\tau_{SRH} = \tau_{p0} \frac{n_0 + n_1 + \Delta n}{n_0 + p_0 + \Delta n} + \tau_{n0} \frac{p_0 + p_1 + \Delta n}{n_0 + p_0 + \Delta n} \tag{1.20}$$

A fundamental lower limit can be found if we consider very low values, when $\Delta n << n_1$, p_1. In that case τ_{SRH} can be simplified to:

$$\tau_{SRH,lower\ \lim it} = \tau_{p0} \frac{n_1}{N_A} + \tau_{n0} (1 + \frac{p_1}{N_A}) \quad \text{for } p\text{-type silicon} \tag{1.21.a}$$

$$\tau_{SRH,lower\ \lim it} = \tau_{p0} (1 + \frac{n_1}{N_D}) + \tau_{n0} \frac{p_1}{N_D} \quad \text{for } n\text{-type silicon} \tag{1.21.b}$$

From these equations, it can be seen that $\tau_{SRH,li}$ is constant at low-injection. Moreover, τ_{n0} (τ_{p0}) is a fundamental lower limit for $\tau_{SRH,li}$ in *p*-type (*n*-type) crystalline silicon, since the lowest $\tau_{SRH,low}$ value is obtained for $n_1 = p_1 = n_i$ and in that case n_1, $p_1 << N_{dop}$.

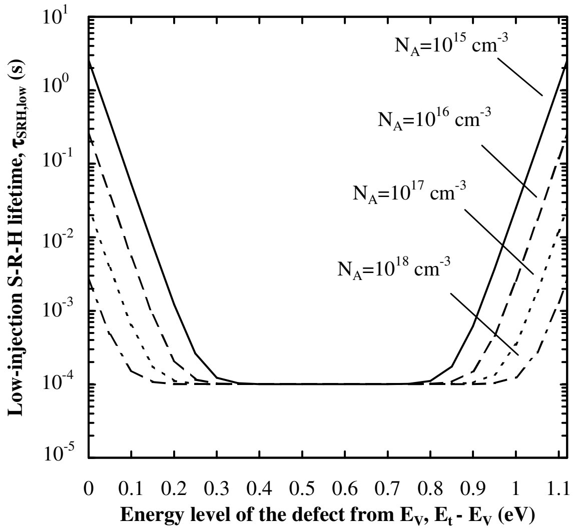

Figure 1.4. τ_{SRH} as a function of energy level of the defect with N_A as a parameter. Defects can be divided into deep and shallow defects. The former causes carrier recombination ($\tau_{SRH}\approx 10^{-4}$ s). For higher acceptor densities, the part of the energy gap which holds deep defects is bigger resulting in a reduction of τ_{SRH}. Extracted from reference [32].

The dependence of τ_{SRH} on the energy level of the defect is more complicated. In Figure 1.4, we show this dependence for a defect moving from the valence band (E_t - E_V = 0 eV) to the conduction band (E_t = 1.12 eV). For this calculation we have taken equation (1.21.a) for a *p*-type *c*-Si with $\tau_{n0} = \tau_{p0} = 100$ μs and for four different doping densities. It can be demonstrated that the obtained results are analogous for *n*-type *c*-Si. As it can be seen, defects located near midgap are more active from the point of view of net recombination leading to the lowest available value for $\tau_{SRH,li}$, i.e. $\tau_{SRH,li} = \tau_{n0}$. These are the so-called d*eep defects,* whereas defects located near the conduction or valence band are called *shallow defects*.

To understand the different behaviour of these defects, it is necessary to take a look at the fundamental transition of carriers, shown in Figure 1.3. To finish an electron-hole pair recombination process, the defect must capture an electron (hole) while it is filled by a hole (electron). In case of a defect whose energy level is located near the conduction band, electrons would have a high probability to be trapped because the energy jump is small. For the same reason, the probability of being emitted again to the conduction band is much higher than the probability of capture a hole. Hence, the contribution of these defects to the net recombination rate is very low. An analogous argumentation can be made with defects located near the valence band. As a consequence, defects located near midgap are the relevant ones from the point of view of carrier recombination.

The dependence of $\tau_{SRH,li}$ on the doping density is also shown in Figure 1.4. It can be seen that for lower doping densities, the part of the energy bandgap which holds deep defects is reduced allowing higher $\tau_{SRH,li}$ values for similar defect distribution than in highly-doped *c*-Si.

Regarding high-injection conditions, τ_{SRH} calculated from equation (1.20) is as follows:

$$\tau_{SRH,high} = \tau_{n0} + \tau_{p0} \qquad \text{for } n\text{- and } p\text{-type silicon} \qquad (1.22)$$

As it can be seen, $\tau_{SRH,hi}$ is constant and it does not depend on the energy level of the trap. Hence, all the defects have similar contribution to the net recombination rate. That means deep defects are less efficient at high-injection, whereas shallow defects are more active. The validity of the last equation is restricted to assumption number 4, which assumes a small relaxation time of carriers. A constant lifetime relates to U_{SRH} which increases linearly with the excess carrier density as it can be deduced from equation (1.1). Physically, it is not possible to maintain this dependence with a finite number of defects. Beyond a certain Δn, the Shockley-Read-Hall theory is not valid. If the capturing processes are fast enough, the traps will reach the filled state the most part of the time and in the limit (Δn tending to infinity), no recombination will be possible because all the traps will be filled. Hence, in this limit $\Delta_{SRH,hi}$ will tend to infinite. This phenomenon, known as *trap saturation*, was analyzed by Dhariwal *et al.* [33].

When studying recombination processes in the crystalline silicon it is helpful to separate the SRH recombination occurring in the bulk silicon from that occurring at the surface. Therefore, we provide a separate analysis in the following subsections.

1.2.3.1 SRH recombination in the bulk

For the bulk silicon the aforementioned equations can be directly applied. Since Auger and radiative mechanisms are also present in the bulk silicon, the total recombination rate is the sum of the separate rates. It can be easily deduced (see more details in section 1.4) that there exists an effective bulk lifetime given by the inverse sum

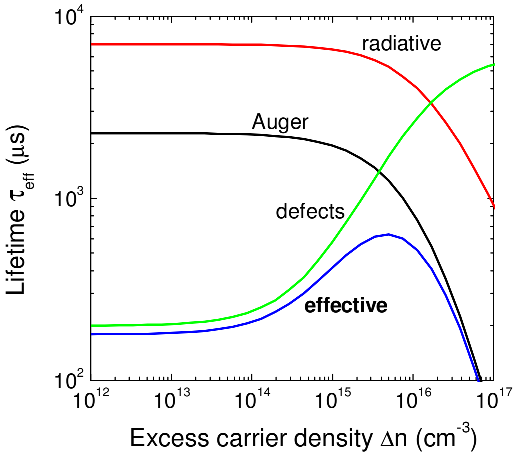

Figure 1.5. Fundamental recombination mechanism in the bulk of a silicon *p*-type wafer at 300 K ($n_i = 10^{10}$ cm^{-3}, $N_A = 1\ \Omega$ cm, $\tau_{n0} = 200\mu s$, $\tau_{p0} = 6$ ms).

of every lifetime process. Figure 1.5 shows an example of this combination for a *p*-type wafer with low relatively SRH lifetime.

The SRH lifetime depends strongly on the fabrication process. Monocrystalline silicon is desired to be a single and perfect crystalline lattice without any defect. However, the presence of dopants always ensures a certain density of recombination centres that becomes more important for low resistivity wafers. The best method to grow high quality semiconductor materials is called Float Zone (FZ). With this it is possible to achieve very high SRH lifetimes that are in the order of the Auger lifetime. Hence the, SRH contribution in the bulk can be neglected in such material when studying other recombination processes. That is why this material is commonly employed in surface recombination analysis, as in this thesis.

Float Zone technique is an improvement of a more classical growing method, the Czochralsky (Cz) technique. The SRH lifetime in these wafers is well below the Auger lifetime at low injection densities because a large amount of impurities are still present after its fabrication, especially oxygen. The high oxygen content in boron doped *p*-type , Cz(B) substrates resulted in cell performance degradation after the cells had been illuminated under 1 sun illumination for a few hours [34]. In a separate study on this Cz(B) degradation effect, Schmidt *et al.* concluded that the reaction for boron with oxygen was the cause for this effect [35]. Some alternatives to avoid this degradation effect are working with other *p*-type dopants such as gallium, indium or aluminium. It is also interesting the option of Boron doped Magnetically confined Cz grown (MCz(B)), with reduced amount of oxygen [36].

1.2.3.2 Surface recombination

The continuity of the crystal lattice is completely lost at the surface of any crystalline material. This represents a large number of silicon atoms with dangling bonds, acting as defects located within the bandgap that produce a high recombination rate. The surface recombination can be explained in terms of the SRH theory by simply replacing the bulk carrier density by the surface carrier density in equation (1.18):

$$U_s = \frac{v_{th} N_{ts} (n_s p_s - n_i^2)}{\frac{n_s + n_1}{\sigma_p} + \frac{p_s + p_1}{\sigma_n}} \tag{1.23}$$

This equation is usually presented as:

$$U_s = \frac{(n_s p_s - n_i^2)}{\frac{n_s + n_1}{S_{p0}} + \frac{p_s + p_1}{S_{n0}}} \tag{1.24.a}$$

$$S_{p0} \equiv v_{th} N_{ts} \sigma_p \tag{1.24.b}$$

$$S_{n0} \equiv v_{th} N_{ts} \sigma_n \tag{1.24.c}$$

where S_{n0} and S_{p0} are the so-called fundamental recombination velocities of electrons and holes, respectively. N_{ts} is the density of defects at the surface *per unit area* and n_s (p_s) is the density of electrons (holes) at the surface per unit volume. Note that, with this definition, the dimensions of U_s are cm^{-2} s^{-1}, whereas in the other cases the recombination was defined per unit volume.

Equations (1.24) are valid for defects with a single level. However, there are a large number of levels within the bandgap that can be considered to spread continuously from the valence band to the conduction band, each of them with a determined density and corresponding capture cross-sections. Hence, it would be more convenient to define a density of states as a function of the energy level, $D_{it}(E)$ and define the surface recombination by

$$U_S = \int_{E_V}^{E_C} \frac{v_{th}\left(n_s\, p_s - n_i^2\right)}{\frac{n_s + n_1}{\sigma_p(E)} + \frac{p_s + p_1}{\sigma_n(E)}} D_{it}(E) dE \tag{1.25}$$

In SiO_2/Si interfaces data for absorption cross section and density of states were measured through Deep Level Transient Spectroscopy (DLTS) in Metal Insulator Semiconductor (MIS) capacitors and used to evaluate equation (1.25) [37]. In other silicon interfaces fabrication of MIS structures is difficult or unviable. However, as a first approximation is sufficient to consider a single dominant defect at the midgap to evaluate surface recombination.

In order to characterize the surface recombination rate, it is useful to relate this parameter with the diffusion term of the current density equation (see for example [29] p. 50). For a *p*-type, homogeneously doped silicon, and in the absence of any electric field, the boundary condition of this equation at the surface holds:

$$qD_n \frac{d}{dx}\Delta n(x)\bigg|_{x=0} = qU_s \tag{1.26}$$

where D_n is the diffusion constant for electrons and $x = 0$ denotes the surface position. Surface recombination can be then characterized by a *surface recombination velocity*, $S(0)$, defined as:

$$U_s = S(0)\Delta n(0) \equiv S(0)\Delta n_s \tag{1.27}$$

where $\Delta n(0) \equiv \Delta n_\mathrm{s}$ is the excess minority carrier density at the surface. Due to the dimensions of U_s (cm^{-2} s^{-1}) the surface recombination is described by a surface recombination velocity measured in cm s^{-1}, instead of a recombination lifetime.

An important difference between bulk recombination via defects and surface recombination is that an electric field is usually found at the semiconductor surface. In this case, Δn_s is far away from Δp_s, since the electric field creates large differences between n_s and p_s. Hence, it is useful to introduce a virtual surface at the edge of the space charge region, and define an *effective surface recombination velocity*, S_eff, as [37,38]:

$$U_s = S_{eff}\,\Delta n \tag{1.28}$$

where $\Delta n = \Delta p$ is the minority carrier density at the limit of the space charge region created at the surface. In contrast to Δn_s, Δn can be easily measured and controlled by changing the illumination level.

Under flat band conditions, the excess carrier density of electrons and holes at the surface, Δn_s and Δp_s respectively, are equal. In addition, assuming uniform generation of carriers throughout the wafer (provided for example by IR light) and low-recombining surfaces, the excess carrier densities are constant through the full thickness of the sample. Hence, $\Delta n_s = \Delta p_s = \Delta n$. Under this particular case, equation (1.24), which represents the recombination rate at the surface with one defect located at E_t, can be expressed as follows:

$$U_s = \frac{(\Delta n + n_0)(\Delta n + p_0) - n_i^2}{\dfrac{\Delta n + n_0 + n_1}{S_{p0}} + \dfrac{\Delta n + p_0 + p_1}{S_{n0}}} \tag{1.29}$$

This equation shows that the surface recombination velocity, S (see equation (1.27)), depends on the properties of the surface states (energy level, S_{n0} and S_{p0}) and also on the injection level Δn and the doping density. The dependence on the energy level of the defect is the same to the Shockley-Read-Hall lifetime (see Figure 1.4). The main conclusion is the distinction between deep levels, which are close to midgap energies and very active from the point of view of recombination, and shallow defects, which are located near conduction or valence band and are more likely to behave as traps. This is the reason why for simplicity in the modelling of lifetime curves we consider a single defect located at the midgap position.

The dependence of surface recombination velocity, S, on the injection level, Δn, is similar to the one described for SRH bulk lifetime. That means that the surface recombination velocity is constant under low and high injection conditions. Regarding low injection, for a p-type c-Si with a doping density of N_A surface recombination is described by:

$$S_{low} = S_{n0}\left(\frac{1}{1 + \dfrac{1}{N_A}\left(p_1 + \left(S_{n0}/S_{p0}\right)n_1\right)}\right) = \frac{S_{n0}}{1 + \dfrac{K}{N_A}} \le S_{n0} \tag{1.30}$$

where K is a positive constant. It can be seen that S_{n0} becomes a fundamental upper limit of S_{low} in a p-type material. This is related to the fact that under low-injection conditions the availability of minority carriers, electrons in a p-type c-Si, is the limiting mechanism for surface recombination. In case of high-injection conditions, S_{high} is constant and equal for both n- and p-type c-Si:

$$S_{high} = \frac{S_{p0} S_{n0}}{S_{p0} + S_{n0}} = \frac{S_{n0}}{1 + \dfrac{S_{n0}}{S_{p0}}} \tag{1.31}$$

1.2.4 Recombination in heavily doped (emitters) regions

Heavily doped silicon regions are used as emitters in solar cells to provide separation of the photogenerated electron-hole pairs, achieved through a strong electric field present at the space charge region of the *p-n* junction. Consequently, a voltage appears between the two regions. Under open circuit conditions, such open circuit voltage depends on the photogenerated carriers at the edge of the space charge region as [39]:

$$np \approx \Delta n(0)\left[N_{dop} + \Delta n(0)\right] = n_i^2 \exp\left(\frac{qV_{oc}}{kT}\right) \tag{1.32}$$

where N_{dop} is the base doping and $\Delta n(0)$ is the excess carrier density at the edge of the space charge region. It becomes clear that to achieve high open circuit voltages it is necessary to use high doping for both base and emitter regions. In practical development of solar cells it is common to use *p*-type bases of 1 Ω cm and *n*-type emitters with sheet resistances between 40 and 100 Ω/sq. This represents a trade-off between high V_{oc} and low recombination losses.

Emitter recombination is not a fundamental mechanism, but the result of the other mechanisms at special given conditions. In the bulk of such heavily doped regions the main contribution to recombination is Auger (as its component goes with $1/n^3$), with some noticeable effect of the radiative recombination (that behaves like $1/n$). The SRH recombination can in principle be neglected. The whole recombination in a *p-n* junction is described by a model including two diodes, normally called the *diffusion diode* and the *recombination diode*. The diffusion diode takes into account the recombination in the emitter bulk (mainly Auger) while the recombination diode accounts for the losses in the Space Charge Region (SCR) due to a SRH process. The calculations of their current-voltage (*I-V*) characteristics give simple expression for the diffusion and recombination current densities [40]:

$$J_{dif} = J_{0e} \exp\left(\frac{qV}{kT}\right) \tag{1.33.a}$$

$$J_{rec} = J_{0rec} \exp\left(\frac{qV}{n_{rec}kT}\right) \tag{1.33.b}$$

where $J_{0\mathrm{e}}$ and $J_{0\mathrm{rec}}$ are the corresponding minority saturation current densities that characterize the two diodes, q is the electronic charge, k the Boltzmann constant, T the actual temperature and V the external voltage applied. In crystalline silicon, when a single trap level located at the intrinsic level, E_i, and identical fundamental SRH lifetimes are considered ($\tau_{n0} = \tau_{n0}$), the ideality factor takes the value $n_{rec} = 2$. For other distribution of traps along the bandgap this value may change.

It is interesting to extract a relationship between the emitter lifetime and the minority saturation current densities as a function of the injection density [41]. We first start assuming symmetrical n^+-p-n^+ or p^+-n-p^+ emitters located at both side of a base with a thickness W. Then, under open circuit conditions the total recombination *per unit surface* at the emitter is described by:

$$qU_{emitter} = J_{0e}\left(e^{V_{oc}/qkT} - 1\right) + J_{0rec}\left(e^{V_{oc}/n_{rec}qkT} - 1\right) \tag{1.34}$$

This equation takes into account all the recombination occurring between the edge of the space charge region at the base throughout all the emitter, up to the surface. On the other hand, the recombination in the whole structure is the sum of all recombination processes, being in this case the bulk and the two emitter contributions. Taking into account equation (1.1) this gives:

$$\frac{\Delta n\, W}{\tau_{eff}} = \frac{\Delta n\, W}{\tau_{bulk}} + 2U_{emitter} \tag{1.35}$$

It is assumed in this equation that Δn has a constant value throughout the wafer, this is essentially true when the diffusion length of the carriers is larger than the wafer thickness, W. Combining equations (1.29) (1.31) and (1.32) we finally reach to:

$$\frac{1}{\tau_{diff}} = \frac{2J_{0e}\left(N_{dop} + \Delta n\right)}{qW\, n_i^2} \tag{1.36.a}$$

$$\frac{1}{\tau_{rec}} = \frac{2J_{0rec}}{qW\Delta n}\left[\frac{\left(N_{dop} + \Delta n\right)\Delta n}{n_i^2}\right]^{1/n_{rec}} \tag{1.36.b}$$

Under high-injection conditions, the dominant term is the one related to J_{0e} which reduces τ_{eff} following a $1/\Delta n$ dependence. Nevertheless, at low-injection the term related to J_{rec} reduces τ_{eff} from the constant value expected where only the diffusion term is considered. The rate of this reduction depends on the value of the ideality factor. Then, τ_{eff} is decreased at low and high-injection. As a consequence, a maximum in τ_{eff} located at medium injection should be expected. An example of emitter recombination is given in Figure 1.6.

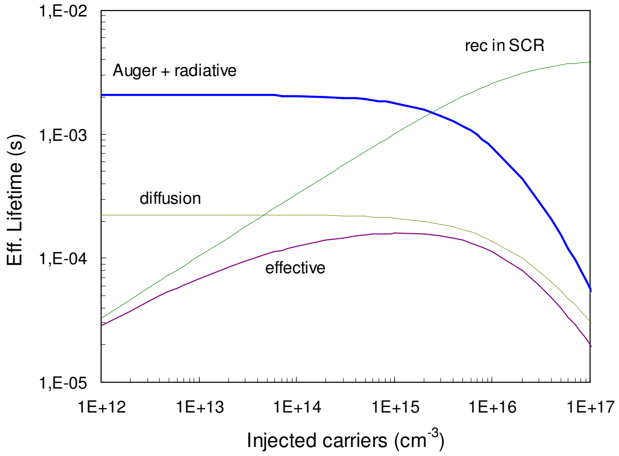

Figure 1.6. Recombination processes in a *p*-type silicon wafer ($N_A = 1.6 \times 10^{16}$ cm^{-3}) with *n*-type emitters located at the two sides. Assumptions: $J_{0e} = 5 \times 10^{-14}$ A cm^{-2}, $J_{0rec} = 5 \times 10^{-9}$ A cm^{-2}, $n_{rec} = 2$, $W = 300$ µm.

1.3 Surface passivation techniques

The high number of defects at the bare silicon surfaces makes surface recombination the dominant mechanism in silicon. The reduction of such surface recombination is called surface passivation and is a requisite to maintain the minority carrier density high and to achieve high efficiency solar cells.

As stated in equation (1.32), the open circuit voltage is directly related to the presence of carrier density at the edge of the space charge region of the *p-n* junction. When thickness of the silicon wafer is decreased to reduce costs, the probabilities of photogenerated carriers to reach the rear surface increase. Figure 1.7 shows simulated efficiencies as a function of the wafer thickness reported by Aberle [42]. There were considered different surface recombination velocity values and two different materials, one with good quality and hence a high diffusion length and the other with low diffusion length. It is evident that efficiency will increase monotonically with increasing diffusions length and by lowering surface recombination velocity. The most remarkable fact is that for low quality materials (diffusion length equal to 200 µm) and sufficiently low values of surface recombination velocity there is a thickness, at around 50 µm, that optimizes the efficiency. Therefore, the reduction of the surface recombination velocity parameter, i.e. surface passivation, is crucial for the development of high efficiency solar cells at low costs. Physically, this surface passivation is achieved by two effects: the field effect passivation and the direct saturation of defects.

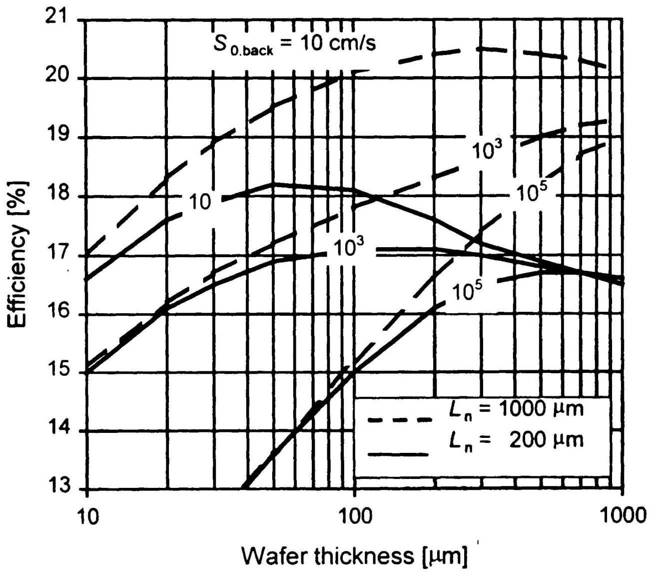

Figure 1.7. Simulations of 1 sun efficiencies of an n^+-p c-Si solar cell as a function of the wafer thickness reported in reference [42].

1.3.1 Field effect passivation

Since two types of carriers, electrons and holes, are needed to complete the process, recombination is maximized when their population is equal. On the other hand, if the population of electrons and holes is unbalanced, the recombination rate is strongly reduced. The field effect passivation consists of producing a band bending at the silicon surface, thus creating an electric field (there the name) and reducing one type of carriers at the interface.

Technically, the electric field can be created in several ways, by depositing a charged film or by creating a heavily doped region. Dielectric films storing a high charge density, like amorphous silicon nitride, have already been successfully applied in solar cell industry. It may also be possible to deposit or grow dielectric layers with a relatively low charge density, like thermally grown silicon dioxide, and apply an external voltage or an electrostatic charge at the surface by a corona charging instrument to provide the field effect. In the case of heavily doped regions, they can be either *high-low junctions* with the same type of impurities (p^+-p or n^+-n) or p-n junctions with opposite doping types. The p^+-p combination is commonly employed at rear side of conventional solar cells using aluminium, contacting the base and achieving at the same time what is called as *back* *surface field*. On the contrary, the *p-n* junctions are usually contacted and located at the front side of the solar cell, though they can also be not contacted (in that case they are called *floating junctions*).

1.3.2 Saturation of defects

The high amount of defects at the surface can be reduced by saturating the remaining silicon dangling bonds. According to the SRH theory, this would represent a direct reduction of the fundamental recombination velocities of electrons (S_{n0}) and holes (S_{p0}) described by equation (1.24). Technologically, this strategy is usually related to a passivating layer deposited or grown over the *c*-Si surface which decreases N_{ts}, since v_{th} is a constant of the semiconductor material and σ_n and σ_n are parameters intrinsically related to the type of defect. This strategy is much more sensitive to the presence of defects at the silicon surface than the field effect passivation, because the carriers are reaching the interface. In this sense, the cleaning steps before deposition or growth of the passivating film are of paramount importance to reduce N_{ts}. In the last step of RCA [43] or other chemical cleaning methods the wafer is dipped into diluted HF solution in order to eliminate the native oxide at *c*-Si surface. Moreover, this immersion tries to achieve a perfect coverage of the *c*-Si surface dangling bonds by atomic hydrogen (leading to very low S_{eff} values [44]). Other approaches to wafer cleaning that are economically less expensive than RCA and therefore more suitable to large area coverage are dry cleaning methods. They normally consist of subjecting the wafer to plasma with an etching gas [45,46]. The method is also useful to roughen the surface, thus providing a light trapping scheme. Finally, some passivation techniques to reduce N_{ts} are based on dangling bond saturation by atomic hydrogen. For instance, it is common to add molecular hydrogen (H_2) into the precursor gases when a passivating layer is deposited by PECVD [47]. The same idea is exploited in annealing the samples within a N_2/H_2 atmosphere (Forming Gas).

1.4 The effective lifetime as a characterization tool for surface passivation

1.4.1 General relationship between effective lifetime and surface recombination velocity

It would be desirable to study each recombination process separately. However, all the recombination processes described in section 1.2 can occur simultaneously within a silicon wafer. They can be treated as an effective recombination with the corresponding *effective lifetime*, this last being the measurable parameter.

The recombination mechanisms can be considered to occur independently, so that the total recombination is simply the sum of all processes. If all the mechanisms aforementioned occur, then it follows:

$$U_{effective} = U_{radiative} + U_{Auger} + U_{SRH} + U_{emitter} + U_{surface} \tag{1.37}$$

Taking into account equation (1.1), and assuming constant excess carrier density along the whole silicon wafer, the definition of effective lifetime arises as:

$$\frac{1}{\tau_{eff}} = \frac{1}{\tau_{radiative}} + \frac{1}{\tau_{Auger}} + \frac{1}{\tau_{bulk\ SRH}} + \frac{1}{\tau_{emitter}} + \frac{1}{\tau_{surface}} \tag{1.38}$$

In a practical case, the emitter is located at the surface and hence the surface recombination contribution is incorporated in the saturation current density, J_{0e}, being therefore unnecessary the inclusion of the surface term in the equation. In Chapter 5 a deeper analysis of emitter recombination and passivation is performed, and it is also discussed how to separate bulk emitter and surface emitter contributions.

On the other hand, the bulk recombination processes are normally grouped together:

$$\frac{1}{\tau_b} = \frac{1}{\tau_{radiative}} + \frac{1}{\tau_{Auger}} + \frac{1}{\tau_{bulk\ SRH}} \tag{1.39}$$

In all the experiments performed in this thesis Float Zone silicon wafers of very high quality are employed. Therefore, the presence of defects within the bulk is extremely low and the corresponding SRH lifetime will be assumed to be infinite. On the contrary, SRH model is employed to analyze the recombination present at the interface.

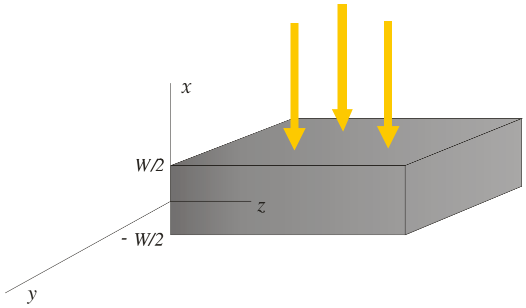

Figure 1.8. Schematic for the calculation of the lifetime expression in a silicon wafer illuminated by the front side.

In the following, we develop an expression to relate the effective lifetime to the surface recombination velocity, S_{eff}. A schematic of the system to be analyzed is shown in Fig 1.8, with a silicon wafer with thickness W and with the two sides located at the $W/2$ and $-W/2$ positions, respectively. The following reasonable assumptions are used in order to simplify this calculation:

- The y- and z- dimensions of the wafer are much longer than x-dimension.
- τ_b is uniform within the wafer and both surfaces have the same S_{eff} value.
- The photogeneration rate within the wafer, $G_{\mathrm{ext}}(t)$, is constant through the whole thickness leading to a *symmetrical profile* of $\Delta n(x)$.

The starting point is equation (1.1), modified in the following way to account for all the recombination processes occurring in the wafer and incorporating the effective lifetime. Assuming a recombination process *per unit area*, it holds:

$$\sum_i U_i = \frac{\Delta n_{av} W}{\tau_{eff}} \tag{1.40}$$

where Δn_{av} is the average excess carrier density within the wafer defined as:

$$\Delta n_{av} = \frac{1}{W} \int_{-W/2}^{W/2} \Delta n(x)\, dx \tag{1.41}$$

and W is the thickness of the c-Si wafer. Different profiles of $\Delta n(x)$ can be found depending on the wavelength of the light source and the surface recombination velocities at front and back surfaces. A high simplification is achieved in the equation when uniform profiles of $\Delta n(x)$ are considered. For sufficient high effective lifetime values Δn_{av} can be assumed to be constant regardless what is the illuminated side and the wavelength. This is because the diffusion time of carrier is shorter than the recombination time. For low effective lifetime values (for example due to bad passivated surfaces or low bulk lifetime values as multicrystalline silicon wafers) the recombination time is shorter than the diffusion time and therefore the carrier density is not uniform. In such cases it is convenient the use of infrared light for carrier generation, as the light absorption is more uniform along the wafer. Separating the bulk and the surface contributions we have:

$$\sum_i U_i = \int_{-W/2}^{W/2} U_{bulk} dx + U_{s,front} + U_{s,back} \tag{1.42}$$

From the definition of every recombination rate developed in section 1.2:

$$\sum_i U_i = \frac{\int_{-W/2}^{W/2} \Delta n(x) dx}{\tau_b} + S_{eff,front}\,\Delta n(W/2) + S_{eff,back}\,\Delta n(-W/2) \tag{1.43}$$

We are assuming for this last expression that τ_b is uniform throughout the wafer, i.e. the wafer is homogeneous. When identical effective surface recombination velocities at both surfaces $S_{eff,front} = S_{eff,back} = S_{eff}$ and a uniform photogeneration are considered, the $\Delta n(x)$ profile is symmetrical and then $\Delta n(W/2) = \Delta n(-W/2)$. Applying this and the definition of Δn_{av} presented in equation (1.41), it follows:

$$\frac{\Delta n_{av} W}{\tau_{eff}} = \frac{\Delta n_{av} W}{\tau_b} + 2S_{eff}\,\Delta n(W/2) \tag{1.44}$$

Finally, τ_{eff} can be isolated from the above equation and defined as:

$$\boxed{\frac{1}{\tau_{eff}} = \frac{1}{\tau_b} + \frac{2S_{eff}}{W}\frac{\Delta n(W/2)}{\Delta n_{av}}} \tag{1.45}$$

Then, from the measured τ_{eff} values, different recombination parameters of the sample can be deduced depending on the preponderant recombination process. Special attention must be paid to the relation between $\Delta n(W/2)$ and Δn_{av} in order to accurately determine S_{eff} from τ_{eff} data.

1.4.2 General relationship between effective lifetime and excess carrier density

In all the techniques the determination of the lifetime is performed through measurements of the excess carrier density. At the end of this section we will have developed an expression relating the effective lifetime, the average excess carrier density and the generation rate of carriers in the wafer. It is very convenient to achieve a uniform value of the excess carrier density along the wafer for simplification of the related equations, as well as equal excess carrier density for electrons and holes ($\Delta n = \Delta p$).

However, there are some situations in which this equality is not accomplished. In sections 1.5.4.1 and 1.5.4.2 two important cases of such effect are analysed in detail.

We first start by describing the generalised state described by Nagel *et al.* in 1999 [48]. Before this publication, transient state and quasi-steady state were treated separately. Apart from the assumptions presented in the previous section to reach equation (1.45), in the following analysis we also assume that:

1. The structure is symmetrical, with identical surfaces and a symmetric profile of $\Delta n(x)$.
2. Every photon generates the same number of electrons and holes, $\Delta n = \Delta p$.
3. *c*-Si wafer is *p*-type, then minority carriers are electrons. Symmetrical results can be obtained for *n*-type *c*-Si.
4. The sample is under open-circuit conditions, since measurement is typically done contactlessly.
5. Within the *c*-Si bulk, the electric field is negligible (quasi-neutral assumption).

Then, we start from the continuity equation of minority carriers, in this case electrons:

$$\frac{d\Delta n}{dt} = G_{ext}(t) - \frac{\Delta n}{\tau_b} - \frac{1}{q}\frac{dJ_n}{dx} \tag{1.46}$$

where J_n is the current density of electrons. Definitions of J_n and J_p are as follows:

$$J_n = q\mu_n nE + qD_n\frac{d\Delta n}{dx} \tag{1.47.a}$$

$$J_p = q\mu_p pE - qD_p\frac{d\Delta n}{dx} \tag{1.47.b}$$

where E is the electric field and D_n (D_p) is the diffusion coefficient of electrons (holes). Since the wafer is under open-circuit conditions, $J_n + J_p = 0$ at any x position. Using this assumption and the neutrality of charge, equation (1.46) can be expressed as:

$$\frac{d\Delta n}{dt} = G_{ext}(t) -$$

$$\frac{\Delta n}{\tau_b} + D_n\left(1 + n\frac{D_p - D_n}{nD_n + pD_p}\right)\frac{d^2\Delta n}{dx^2} + \mu_n\left(1 - n\frac{\mu_p + \mu_n}{n\mu_n + p\mu_p}\right)E\frac{d\Delta n}{dx} \tag{1.48}$$

Using the definitions of the ambipolar mobility, μ_{amb}, and the ambipolar diffusion coefficient, D_{amb}:

$$D_{amb} = \frac{(p+n)D_pD_n}{nD_n + pD_p} \tag{1.49}$$

$$\mu_{amb} = \frac{(p-n)\mu_p \mu_n}{n\mu_n + p\mu_p} \tag{1.50}$$

Equation (1.44) can be rewritten as:

$$\frac{d\Delta n}{dt} = G_{ext}(t) - \frac{\Delta n}{\tau_b} + D_{amb}\frac{d^2\Delta n}{dx^2} + \mu_{amb} E \frac{d\Delta n}{dx} \tag{1.51}$$

Applying the quasi-neutral assumption, this equation is reduced to:

$$\frac{d\Delta n}{dt} = G_{ext}(t) - \frac{\Delta n}{\tau_b} + D_{amb}\frac{d^2\Delta n}{dx^2} \tag{1.52}$$

Now, we integrate this expression within the wafer thickness:

$$\int_{-W/2}^{W/2} \frac{d\Delta n}{dt} dx = \int_{-W/2}^{W/2} G_{ext}(t) dx - \int_{-W/2}^{W/2} \frac{\Delta n}{\tau_b} dx + \int_{-W/2}^{W/2} D_{amb}\frac{d^2\Delta n}{dx^2} dx \tag{1.53}$$

This equation can be simplified by applying the assumption of a constant $G_{ext}(t)$ through the whole thickness and by the definition of Δn_{av} presented at equation (1.40). Then:

$$W\frac{d\Delta n_{av}}{dt} = G_{ext}(t)W - \frac{\Delta n_{av} W}{\tau_b} + D_{amb}\left.\frac{d\Delta n}{dx}\right|_{-W/2}^{W/2} \tag{1.54}$$

If we assume identical surfaces and a symmetrical $\Delta n(x)$ profile the boundary conditions hold:

$$\left.\frac{d\Delta n}{dx}\right|^{W/2} = -\left.\frac{d\Delta n}{dx}\right|^{-W/2} \tag{1.55}$$

and then:

$$\frac{d\Delta n_{av}}{dt} = G_{ext}(t) - \frac{\Delta n_{av}}{\tau_b} + 2\frac{D_{amb}}{W}\left.\frac{d\Delta n}{dx}\right|^{W/2} \tag{1.56}$$

In order to maintain a surface recombination rate, a current flow of minority carriers which feeds this recombination is needed. Then:

$$qU_s = J_n\big|^{W/2} \tag{1.57}$$

$$q\,S_{eff}\,\Delta n(W/2) = -q\,D_{amb}\left.\frac{d\Delta n}{dx}\right|^{W/2} \tag{1.58}$$

Applying this equation to equation (1.56):

$$\frac{d\Delta n_{av}}{dt} = G_{ext}(t) - \frac{\Delta n_{av}}{\tau_b} - 2\frac{S_{eff}}{W}\Delta n(W/2) \tag{1.59}$$

Finally, using the definition of τ_{eff} presented in equation (145), the final result is:

$$\boxed{\frac{1}{\tau_{eff}} = \frac{G_{ext}(t) - \frac{d\Delta n_{av}}{dt}}{\Delta n_{av}}} \qquad (1.60)$$

This equation describes the general relationship for the lifetime of a wafer under any illumination source and it is only dependent on the average excess carrier density and the external generation. It is important to note that it has been deduced without applying any assumption about the wavelength of the light excitation or the τ_{eff} range. The importance of equation (1.60) resides in the fact that all the methods for lifetime measurements are based on the determination of excess carrier density, Δn. From it three different states out of thermodynamic equilibrium are considered: Transient State, with no external generation, Steady State, with constant generation and Quasi Steady State (QSS), with an almost constant generation.

Similar calculations to reach to equation (1.60) can be done considering a light source which intensity varies exponentially with time (i.e. as A $\exp(-t/\tau)$). Since most of the time dependent sources used for lifetime measurements are exponentially dependent the expressions derived from such assumptions can be applied in many cases. Using this condition Tyagi *et al.* [49] developed a complex expression for the carrier density in a silicon wafer as a function of the position, the time, and the illumination wavelength, i.e. $n(x,t,\lambda)$. Then, Brody *et al.* [50] integrated such $n(x,t,\lambda)$ for a general spectrum to get $n(x,t)$ as a function of the recombination parameters (basically the surface recombination velocity, the bulk lifetime and the diffusion coefficient). In the following we analyse some particular cases of equation (1.60) and $n(x,t,\lambda)$ for the three different states aforementioned.

1.4.2.1 Steady state

For steady-state conditions generation is constant and the derivative term of (1.60) is zero. Brody *et al.* averaged the aforementioned $n(x,t)$ expression and introduced it into (1.60) under these circumstances. In the case of very high surface recombination velocities this equation tends to a limit value for τ_{eff}. With S tending to infinite and assuming a steady state generation constant throughout the wafer thickness, the effective lifetime would be given by:

$$\frac{1}{\tau_{eff}} = \frac{1}{\tau_{bulk}} + \frac{12}{W^2}D \qquad (1.61)$$

Such constant generation can be achieved using infrared light. The bulk lifetime will be usually a high value, so that a minimum measurable value for the lifetime is given by:

$$\frac{1}{\tau_{\min}} = \frac{12}{W^2} D \tag{1.61}$$

In the practical cases with low resistivities (around 1 Ω cm) and thicknesses in the range of hundred of microns, this value is normally less than 10 μs. For example, for *p*-type wafers 0.95 Ω cm, 300 μm thick (used in Chapter 4 and 5) D is equal to 26.6 cm^2 s^{-1}. In that case the minimum lifetime that we can measure is 2.8 μs.

1.4.2.2 Transient state

In transient conditions the generation is zero, and the solution of equation (1.60) using the aforementioned complex expression of $n(x,t)$ has the following simple expression:

$$S = \sqrt{D\left(\frac{1}{\tau_{eff}} - \frac{1}{\tau_{bulk}}\right)} \tan\left[\frac{W}{2}\sqrt{\frac{1}{D}\left(\frac{1}{\tau_{eff}} - \frac{1}{\tau_{bulk}}\right)}\right] \tag{1.63}$$

A further simplification is achieved if low values of surface recombination velocities are assumed. That is to say, for $SW/D < 1/4$ this following approximation is valid with an error less than 4%:

$$\boxed{\frac{1}{\tau_{eff}} = \frac{1}{\tau_{bulk}} + \frac{2S}{W}} \tag{1.64}$$

This happens for example for $S < 250$ cm s^{-1}, $W = 300$ μm and $D = 30$ cm^2 s^{-1}.

1.4.2.3 General state or Quasi Steady State (QSS)

Equation (1.45) describes a general dependence of the lifetime with S_{eff} considering only symmetrical Δn profiles and identical surfaces. We have also stated that under an exponential time dependent source a very long but analytical equation (not written) can be found. If we assume the following particular condition:

$$n_{av} = \frac{n(W/2) + n(-W/2)}{2} \tag{1.65}$$

then the expression of the lifetime with surface recombination velocity is given by:

$$\boxed{\frac{1}{\tau_{eff}}=\frac{1}{\tau_{bulk}}+\frac{2S}{W}} \tag{1.66}$$

which matches exactly (1.64) but in this case applied to a general state. Moreover, it is very similar to equation (1.45). An obvious way to achieve condition (1.65) is with uniform value of the carrier density along the wafer. This normally happens when the surface recombination velocity is low, or equivalently the transient time for the carriers to distribute is much faster than the effective lifetime. An important comment must be made at this point. In surfaces passivated by field effect there is a space charge region with increased or reduced minority carrier densities, depending on the direction of the electric field. As we said in section 1.2.3.2, a virtual surface at the edge of the space charge region can be assumed, with an effective surface recombination velocity, S_{eff}, as depicted in Figure 1.9. Then the recombination from the space charge region to the surface can be attributed to a diffusion process and the general equations (1.45) and (1.60) are still valid. Furthermore, if Δn at the space charge region (labelled as d in Figure 1.9) is the same constant value along the wafer, and $d \ll W$, then equation (1.66) is also valid replacing S by S_{eff}.

1.5 Lifetime measurements through photoconductance based methods

This method gives a direct relationship between the effective lifetime, the excess carrier density and the photoconductance of the silicon wafer. Light is employed to create an excess of carriers within the wafer and therefore an excess of conductance. In this regime, the wafer is out of the thermodynamic equilibrium, though it can be in steady state, in transient state, or in quasi-steady state.

In photoconductance based methods there are two magnitudes to be measured:

- Sample photoconductance, $\Delta\sigma$. The excess conductance is measured through a voltage signal converter, usually a coil generating a variable magnetic field. It is directly related to the excess carrier concentration along the wafer:

$$\Delta\sigma = q\int_0^W \left[\Delta n(x)\mu_n(x)+\Delta n(x)\mu_p(x)\right]dx \tag{1.67}$$

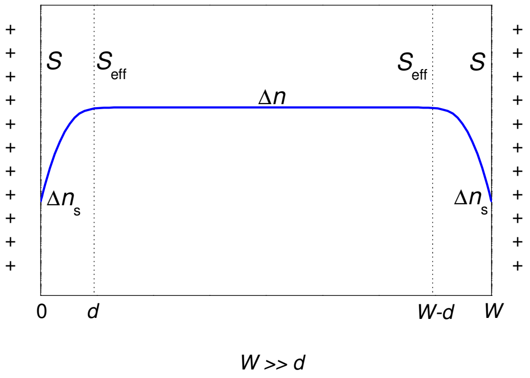

Fig 1.9. Schematic *n*-type wafer with field effect provided by a positive charge density. At the edge of the space charge region it can be assumed an effective surface recombination velocity, S_{eff}, so that the recombination rate can be estimated by equation (1.27) with the corresponding Δ*n*.

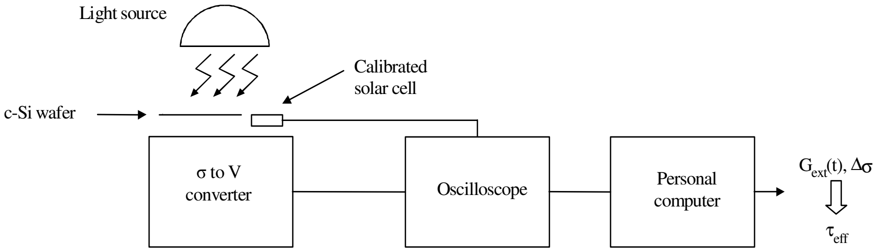

Figure 1.10. Block diagram of a generic τ_{eff} measurement system.

where W is the sample thickness, q is the fundamental charge and μ_n and μ_p are the electron and holes mobilities. When carrier concentrations are equal ($\Delta n = \Delta p$) and uniform along the wafer, the equation can be simplified to

$$\Delta\sigma = qW(\mu_n + \mu_p)\Delta n_{av} \qquad (1.68)$$

- The light intensity: it is measured through the short circuit current of a calibrated solar cell placed next to the *c*-Si wafer. From this magnitude, the electron-hole pair photogeneration within the wafer, $G_{ext}(t)$, can be estimated. To accurately determine $G_{ext}(t)$, it is necessary to define an effective optical transmission factor, which takes into account the reflection losses of the samples.

A schematic of the set-up measurement is presented in Fig 1.10. A wafer is placed on the photoconductance to voltage converter, and irradiated by a light source which intensity level can be varied in time, to explore different level of excess carrier densities.

To determine the lifetime from equations (1.67) or (1.68) the carrier mobilities need to be known. The mobility, μ, is defined as the relation between the mean velocity of a carrier and the electric field which drifts it. There are four terms contributing to the total mobility, which are the scattering due to the crstalline lattice, μ_L, the donor density, μ_D, the acceptor density, μ_A, and the electron-hole scattering, μ_{eh} or μ_{he}. Therefore, mobility is dependent on the excess carrier density, Δn. The effective mobility is given by the sum of the four inverse terms:

$$\mu_e^{-1} = \mu_{eL}^{-1} + \mu_{eD}^{-1} + \mu_{eA}^{-1} + \mu_{eh}^{-1} \tag{1.69.a}$$

$$\mu_h^{-1} = \mu_{hL}^{-1} + \mu_{hD}^{-1} + \mu_{hA}^{-1} + \mu_{he}^{-1} \tag{1.69.b}$$

where the sub index *e* stands for electrons and *h* stands for holes. Masseti *et al.* [51] developed an empirical expression for the majority carrier mobility depending on the doping density which is widely used in device simulators. However, we are interested in mobility of minority carriers. That means taking into account the last term in equation (1.69). The most reliable data about this parameter has been measured by Dannhäuser [52] and Krause [53] who measured the sum of electron and hole mobilities as a function of carrier concentration in the intrinsic region of a PIN diode. A more complete model was suggested by Klaassen [54]. Another issue that can be taken into account if a very fine analysis wants to be done is that mobility of the carriers near the surface is strongly reduced due to surface scattering. This effect has been extensively studied for Si/SiO_2 interfaces, showing that the 2D mobility of electrons in an inversion layer is greatly reduced due to interface roughness scattering [55]. In contrast, the literature on this topic for dielectric passivation films is very scarce. The only reference is the work of Elmiger and Kunst [56] that reported electron mobilities of about 250 $cm^2\,V^{-1}\,s^{-1}$ in highly inverted and accumulated Si/SiN_x interfaces with a charge density in the dielectric layer of $Q = 3 \times 10^{12}$ cm^{-2}.

1.5.1 Photo Conductance Decay (PCD)

The Photo Conductance Decay (PCD) method was first developed in 1955 [57] where the photoconductance of the sample was estimated by contacting it and measuring the *I-V* curve. In this method the carrier lifetime is determined from the photoconductance of the sample when there is no electron-hole pairs generation by the external light source, i.e. the sample is in transient conditions. The lamp generates a short pulse of light which creates an excess carrier density within the wafer. This excess of carriers recombines depending on recombination parameters of the bulk and surfaces. Then, with no G_{ext} (t), equation (1.60) is reduced to:

$$\tau_{eff} = -\frac{\Delta n_{av}}{\frac{\delta \Delta n_{av}}{\delta t}} = -\frac{\Delta\sigma / qW(\mu_p + \mu_n)}{\frac{\delta\left(\Delta\sigma / qW(\mu_p + \mu_n)\right)}{\delta t}} = \frac{\Delta\sigma}{\frac{\delta\Delta\sigma}{\delta t}} \qquad (1.70)$$

Hence, in this method the only magnitude needed is the photoconductance of the sample. This can be an advantage, since any error in the calibration of the instrument is cancelled out in equation (1.70). However, a high signal-to-noise ratio at the photoconductance signal is needed to reduce the error in the estimation of the derivative term. As a consequence, relatively high τ_{eff} values are needed to obtain reliable values.

1.5.2 Quasi-Steady State Photo Conductance (QSS-PC) decay

In this state, the time constant of the illumination source is varied slowly, so that at high illumination levels the derivative term in equation (1.60) can be neglected. Nevertheless, the deviations from the real lifetime observed suggest to keep this term for the analysis. The Quasi-Steady State is very useful from high to low injection level ranges. It is necessary, however, to know the external generation at the same time that the photoconductance is recorded.

1.5.3 Photoconductance measurement techniques

In this section we present two commonly employed methods to determine the conductance of the illuminated sample with a contactless method.

1.5.3.1 Microwave detected

This technique is widely used to determine the recombination parameters of *c*-Si wafers [58-60]. In Figure 1.11, we show a typical block diagram of a µW-PCD system. The photoconductance, generated by a pulsed light source, is estimated through the reflection of a microwave signal which is also applied on the sample. The pulsed light source can be a laser with a wavelength between 900 nm and 1100 nm, a led array or a stroboscopic light of xenon. The IR light agrees with the assumption of a constant $G_{\mathrm{ext}}(t)$ within the whole sample thickness. The rising and falling time of the light pulses are very fast, since these times limit the τ_{eff} measurement range; for instance using a laser diode, a typical value is 100 ns.

The microwave signal is usually generated by a Gunn diode with a typical frequency of 10 GHz. A circulator addresses this power to the antenna and finally to the sample. The microwave signal penetrates into the sample and a part of it is reflected depending on its conductivity. Then, the reflected power varies linearly with the photoconductance of the sample. The antenna receives the reflected power which is measured by the detector through the circulator.

This system needs an accurate calibration procedure which takes into account the microwave power loses, the efficiency of the antenna, the distance between the antenna, the sample and the back reflector, etc. Another important limitation is the penetration depth of the microwave signal into the silicon and its dependence on the resistivity of the sample. It is well-known that lower resistivity leads to lower penetration depth. For instance, with a microwave signal of 10 GHz, the penetration depth ranges from 350 µm for a resistivity of 0.5 Ω cm to 2200 µm with 10 Ω cm. The microwave signal only gives information about the excess carrier concentration at those zones where it has penetrated. Then, if the penetration depth is lower than the sample thickness, the measurement can be erroneous. On the other hand, if the penetration depth is much longer than the sample thickness, a multiple reflection phenomenon can occur. This phenomenon can be calibrated by changing the distance between the sample and the back reflector searching a maximum of the reflecting signal. However, due to the different penetration depths, the available injection levels are very limited. During a typical measurement with a high power of incident light, the sample moves from very high injection conditions to almost thermodynamical equilibrium. From the point of view of the reflection of the microwave signal, the penetration depth strongly varies leading to errors in the measurement. This is the reason why this system is used only with low light intensities which generate a low excess carrier density within the sample. In addition to this limitation, if S_{eff} has a strong dependence on the injection level, non monoexponential conductance signals are obtained as reported when *c*-Si surface is passivated by thermally grown SiO_2 [37,61], SiN_x [62] or even with chemical methods [63,64].

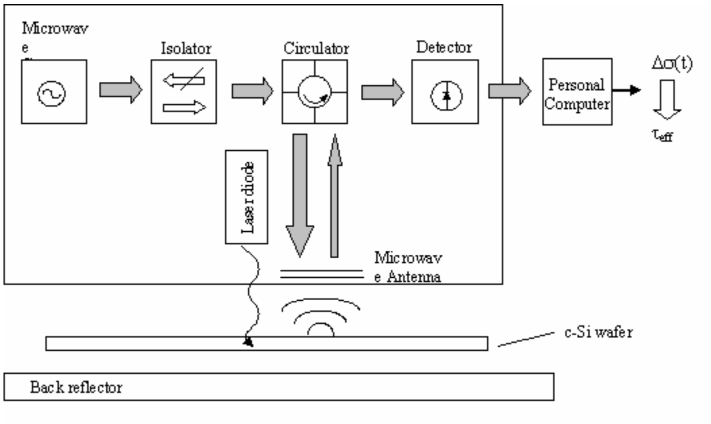

Figure 1.11. Block diagram of a a typical μW-PCD measurement system.

To avoid all these limitations, Basore and Hansen [65] in 1990 introduced a second light source, known as bias light, which generates a constant background carrier concentration. The laser pulse intensity was adjusted to modify the excess carrier concentration in less than a 10%. In this case, the penetration depth of the microwave signal as well as the rest of the physical parameters of the sample are practically constant throughout the recorded PCD signal. Hence, by changing the bias light intensity, recombination parameters of the sample can be determined for a wide range of excess carrier densities. However, recently Brendel [66] realized that the estimated τ_{eff} from the light-biased PCD measurements is not the actual τ_{eff} but a differential effective lifetime. Hence, in order to obtain the τ_{eff} values, an integration from the measured values at very low injection level is needed [42,64,66,67]

1.5.3.2 Inductive coupling

This method was firstly applied in Quasi-Steady State by Sinton and Cuevas in 1996 [68] and currently a comercial equipment with instrumentation and software is available at Sinton Consulting Inc. company [69]. Since it allowed taking measurements in a very wide injection range, the understanding and modelling of lifetime curves improved rapidly and it has been very helpful to analyse surface and recombination parameters, as well as defects in low-cost solar-grade materials. Measurements of the lifetime curves at different temperatures, the so called Temperature and Injection Dependence Lifetime Spectroscopy (TIDLS) [70] allowed the characterization of the energy level of such defects.

The system is based on a RF bridge with an inductive coil that generates electromagnetic fields within the wafer. Variations in the conductivity of the wafer modify these fields leading to a variation of the effective inductive value, thus changing the output voltage of the bridge. Such output voltage and the photoconductance have a parabolic dependence that is acutually close to be linear. A reference wafer of known conductance is normally used to polarize the bridge, and the voltage-conductance curve depends on the properties of this reference wafer. Therefore, it is possible to have different sets of voltage-conductance curves for different reference wafers. The way to obtain this voltage-conductance calibration is to employ a set of samples with know dark conductances. See an example of this in Figure 1.12. Once the bridge is polarized, the dark and light conductances of the sample to be analyzed are varied along the calibrated curve.

A flash lamp is used as excitation source, with a time constant of 2.3 ms for the QSS mode. To determine the external generation of carriers, $G_{\mathrm{ext}}(t)$, it is necessary to measure the illumination level with a reference solar cell. Because the fraction of absorbed light within the wafer will depend on the sample characteristics (kind of passivating layer, wafer thickness, and so on) it is important to estimate this quantity, called *optical factor*. The easiest way to determine the optical factor is doing a PCD measurent, that is, setting a short flash lamp time constant (about 20 μs) and chose an optical factor until both PCD and QSS coincide. This method is valid for sufficiently high values of the lifetime. Figure 1.13 shows the agreement between a PCD and QSS-PC measurement.

This system has clear advantages compared to the μW-PCD system described above. The main one is that once the light source is off, the system correctly detects the photoconductance until the sample reaches almost the thermodynamical equilibrium. Then, the available range of excess carrier density has no intrinsic limit. If the light source is powerful and the recombination within the sample is low, excess carrier densities as high as 10^{16}-10^{17}cm^{-3} can be measured. On the other hand, signal-to-noise ratio of the system will determine the lower limit, which lay typically at $\Delta n = 10^{12}$-10^{13} cm^{-3}.

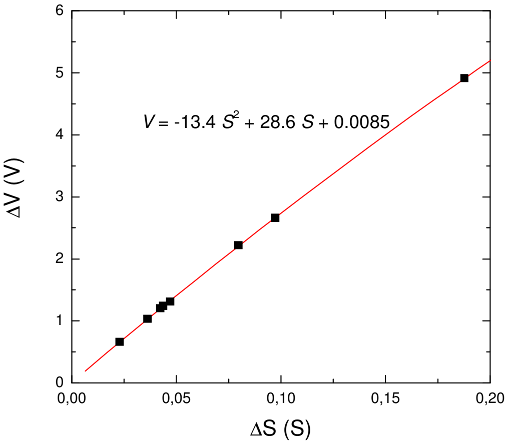

Figure 1.12. Calibration curve of the conductance to voltage signal conversion for the reference wafer. A parabolic fitting is used to estimate the conductance of the test sample.

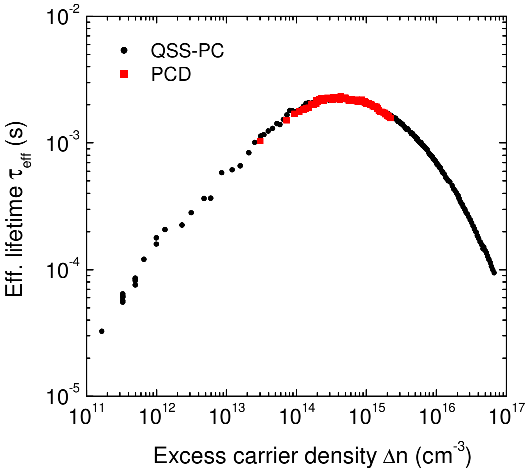

Figure 1.13. Effective lifetime for a FZ *p*-type 6 Ω cm silicon wafer passivated by phosphorus doped amorphous silicon carbide films. PCD method is used to determine the optical factor used in the QSS-PC technique.

1.5.4 Artifacts in photoconductance based methods

As we discussed in the previous section, equations (1.45) and (1.60) can be applied in most of the cases without loosing much generality. The conditions for those equations to be valid are repeated hereafter:

1. equal number of electrons and holes photogenerated $\Delta n = \Delta p$
2. open-circuit conditions
3. no electric field in the bulk wafer
4. uniform bulk lifetime

5. symmetric value of the minority carrier density
6. equal surface recombination velocities at both sides

With these conditions equations (1.45) and (1.60) are valid. If we add the following condition:

7. low surface recombination values to ensures uniform values of Δn

Then equation (1.64) is also valid.

In some cases, conditions 1, 3 and 7 are not accomplished, for example near the surfaces when a field effect passivation is present, or when shallow defects (traps) are present. The first case can be skipped if an effective surface recombination velocity, S_{eff}, is considered, as we have already explained in section 1.4.2.3. Nevertheless, when the photoconductance technique is used to measure the lifetime and condition 1 is not accomplished there are two effects that lead to overestimation of the lifetime at low injection densities. These two effects are called trapping of minority carriers and Depletion Region Modulation (DRM), and they will be explained below.

1.5.4.1 Trapping of minority carriers

Some defects located within the bandgap of the crystalline silicon act as traps of minority carriers without contributing to the recombination. This is because the trap only allows the carrier to return to the original energy band from which it was released. This phenomenon has been widely studied since mid-1950's [71,72] and it has been recently reported in QSS-PC measurements mainly in low-quality *c*-Si substrates [73,74]. Assuming a *p*-type *c*-Si wafer under thermodynamic equilibrium, the neutrality of charge equation is as follows:

$$p_0 = n_0 + N_A + N_T f_0 \tag{1.71}$$

Where p_0 (n_0) is the hole (electron) density under thermal equilibrium, N_A the acceptor density, N_T the trap density and f_0 the probability of being occupied which follows the Fermi-Dirac distribution and depends on the Fermi level position. If the sample is illuminated, the neutrality of charge equation is still valid:

$$p = n + N_A + N_T f \tag{1.72}$$

In this case f depends on the quasi-Fermi level of electrons. We are interested in Δn, then subtracting equations (1.71) and (1.72):

$$\Delta p = \Delta n + N_T \Delta f \tag{1.73}$$

Then, the photoconductance with traps, $\Delta\sigma_t$, is as follows:

$$\Delta\sigma_t = q(\mu_n \Delta n + \mu_p \Delta p) = q(\mu_n + \mu_p)\Delta n + \mu_p N_T \Delta f = \Delta\sigma + \mu_p N_T \Delta f \tag{1.74}$$

This magnitude is used to estimate τ_{eff}. Then, the effect of minority carrier trapped is an increase in the photoconductance of the sample and, hence, an overestimation of τ_{eff}. This effect is only visible under low injection conditions, since at high injection $\Delta n >> N_T \Delta f$ and the excess of holes is equal to the excess of electrons.

A way to partially correct the trapping artifacts was firstly suggested by R. A. Sinton [75], and analysed by Macdonald *et al* [76]. It consists of applying a *bias light* to keep the traps constantly filled. The photoconductivity is enhanced by a constant factor which would lead to an enhanced apparent carrier density. Once this constant factor is subtracted a more realistic excess carrier density and hence more realistic lifetime are determined. The technique makes it possible to lower by up to about one order of magnitude the minimum injection level at which the apparent lifetime is correct to within an error of less than 30%. It is not possible however to determine the low injection limit of the apparent lifetime with this method.

1.5.4.2 Depletion Region Modulation (DRM)

When electric fields are present in a certain location of the silicon wafer there appears a depletion region that unbalances the population of photogenerated carriers ($\Delta n \neq \Delta p$). This happens in the presence of *p-n* junctions, high-low junctions and in charged insulator-semiconductor interfaces. The width of the depletion region is dependent on the carrier concentration, and therefore it is modulated with the illumination level. As a consequence, an overestimation of the excess carrier density is encountered if equation (1.68) is applied for the calculus, with the corresponding overestimation of the lifetime. A kind of increasing "tail" is observed when Δn decreases (see Figure 1.14), sometimes overcoming even the intrinsic Auger limit, and clearly indicating its artificial nature. This effect, called Depletion Region Modulation (DRM), was identified to occur especially at low injection densities [77,78] and modelled in the presence of *p-n* junctions [79] and charged insulators [80]. These two cases will be analysed in section 1.7.

1.6 Photoluminescence based methods

With the aim to get rid of the trapping and DRM artifacts caused by the photoconductance technique, Trupke and Bardos *et al*, from University of New South Wales, developed a method to analyse the minority carrier effective lifetime from the photoluminescence (PL) of the silicon wafer [81,82].

Basically, this technique consist of detecting the photoluminescence (PL) decay at around 1.12 eV employing a photodetector after light excitation by means of a LED working at 870 nm. The photoluminescence signal is directly related to the radiative recombination, so that the lifetime can be determined through equations (1.1) and (1.3). Since the radiative lifetime depends only on carrier concentrations and the parameter B, the technique is free of conductance artifacts.

In the case of trapping artifacts, the error in the technique is very small [83]. In the PL lifetime technique, the measured PL intensity, I_{PL}, is proportional to the product of n and p giving

$$I_{PL} \propto \Delta n\left(\Delta p+N_A\right)=\Delta n\left(\Delta n+n_t+N_A\right)\approx \Delta n\left(n_t+N_A\right) \qquad (1.75)$$

for the p-type wafer considered here, where n_{t} is the density of traps and the last line holds for low level injection conditions i.e., for $\Delta n << N_{\mathrm{A}}$ and $\Delta n << n_{\mathrm{t}}$. Importantly, I_{PL} is only affected by minority carrier trapping in proportion to the ratio of the np product with and without trapping, i.e, in proportion to $N_{\mathrm{A}} + n_{\mathrm{t}}$ under low injection conditions and an even smaller ratio for higher injection conditions. For typical solar cells of low resistivity the apparent lifetime represents an error of less than 1%. In the case of DRM effect, there is no error in considering that the real lifetime is measured, since the photoconductance is not used to calculate the minority carrier densities.

Therefore, it is possible to measure the real lifetime of multicrystalline or DRM affected wafers. However, the PL signal can only be measured in arbitrary units, and a QSS-PC measurement at mid injection level range is required to determine the real value of the lifetime and match it using a calibrating factor with the radiative lifetime.

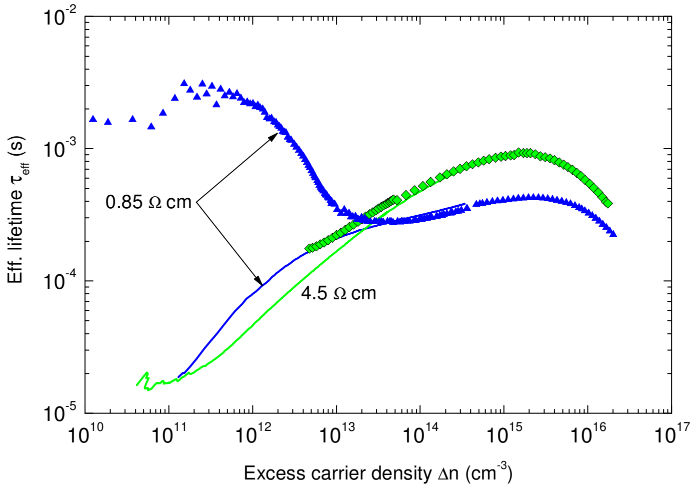

Figure 1.14. Lifetime measurements performed at UNSW through QSS-PC (symbols) and QSS-PL (lines) methods for two silicon *p*-type wafers passivated with amorphous silicon carbide. Note the presence of the DRM effect for the QSS-PC method.

In Figure 1.14 we plot the QSS-PC and QSS-PL measured lifetimes for a silicon wafer passivated by amorphous silicon carbide films. The measurements were taken at the University of New South Wales using for excitation subbandgap illumination (870 nm) with LED and multiple averaging. This allowed reaching very low injection densities for both PC and PL techniques. In section 1.7 we discuss the application of DRM effect to model lifetime curves and extract important parameters, such as the fundamental recombination velocity of electrons or holes and the charge density present at the interface or in the passivating films.

1.7 Simulation of lifetime curves for passivated wafers

It has already been stated that bulk, surface and emitter recombination can be present at the same time in a silicon wafer. All recombination mechanisms have their own theoretical models to predict the corresponding lifetime. Thus, the measured effective lifetime can be fitted to extract important parameters. For high quality materials the bulk lifetime is attributed only to Auger plus radiative recombination processes, which are well known for every doping density. On the other hand, surface recombination is based on Shockley-Read-Hall theory, since it is produced through the unavoidable surface defects located within the bandgap.

It must be pointed out that the developed model for the surface recombination with the SRH theory assumes flat bands throughout the whole wafer. However, the dielectric films used to passived cause a band bending at the first nanometres of the *c*-Si. To incorporate this effect to the initial SRH model, an *extended SRH formalism* was developed by Grove and Fitgerald [84,85] and improved by Girisch [86]. Later, J. Brody and A. Rohatgi [87] derived analytical equations from this model under different assumptions of light intensity and band bending.

1.7.1 Model for a dielectric/c-Si interface (Girisch model)

The only assumption of this model is that quasi-Fermi levels are constant throughout the space charge region. This is accomplished if generation and recombination is negligible at that region. Then, n_b and p_b can be easily calculated using the following expressions:

$$n_s = n_b\, e^{q\Psi_s / kT} \qquad (1.76.a)$$

$$p_s = p_b\, e^{-q\Psi_s / kT} \qquad (1.76.b)$$

where Ψ_s is the voltage at the surface or band bending whose sign is deduced from Figure 1.15. Our problem is now focused on the calculation of Ψ_s which can be determined applying the charge neutrality equation. In an insulator semiconductor structure, we can define the following charge densities, as shown in Figure 1.15:

- Q_{Si}: charge density at the c-Si.
- Q_f: fixed charge density at the insulator. For simplicity, we place this charge density at the insulator/c-Si interface since, from an electrostatic point of view, it is impossible to distinguish between a distributed sheet of charge within a certain depth in the insulator and an equivalent charge density per unit of area placed at the interface.
- Q_{it}: charge density trapped in the interface states. Its value depends on the position of the quasi-Fermi levels and, then, on the illumination intensity.

The expression of the neutrality of charge will be as follows:

$$Q_{Si} + Q_f + Q_{it} = 0 \qquad (1.77)$$

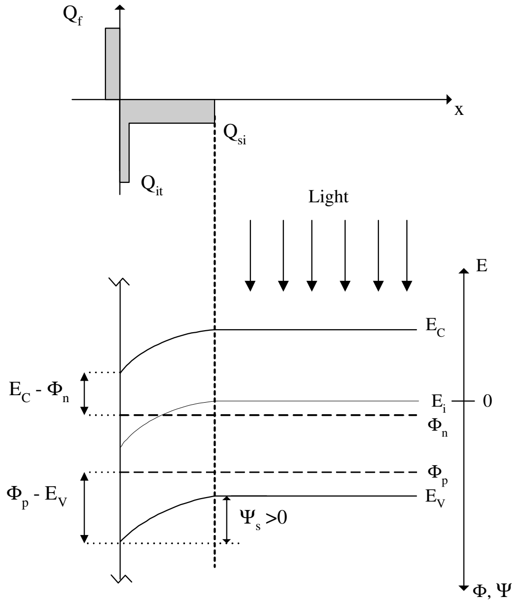

Figure 1.15. Band diagram and charge distribution of an insulator/p-type semiconductor structure where $\Phi_{n(p)}$ is the quasi-Fermi level of electrons (holes) and Ψ_s is the surface potential. Charge definitions are introduced below.

Q_f can be taken as a free parameter of the model and should be determined by fitting the experimental data. On the other hand, Q_f can be also determined by independent experiments (capacitance-voltage measurements) becoming a model data. The rest of the charge densities can be calculated, in fundamental charges per unit of area, using the following expressions [86]:

$$Q_{Si} = \mp\sqrt{\frac{2kTn_i\varepsilon_0\varepsilon_{si}}{q^2}F(\Psi_s,\Phi_n,\Phi_p)} \tag{1.78.a}$$

$$F(\Psi_s,\Phi_n,\Phi_p) = e^{q/_{kT}(\Phi_p-\Psi_s)} - e^{q/_{kT}\Phi_p} + e^{q/_{kT}(\Psi_s-\Phi_n)} -$$

$$- e^{-q/_{kT}\Phi_n} + q/_{kT}\,\Psi_s\frac{(N_A-N_D)}{n_i} \tag{1.78.b}$$

$$Q_{it} = -\int_{Ev}^{Ec} D_{it,a}(E)f_a(E)dE + \int_{Ev}^{Ec} D_{it,d}(E)f_d(E)dE \tag{1.79.a}$$

$$f_a(E) = \frac{\sigma_n(E)n_s + \sigma_p(E)p_1}{\sigma_n(E)(n_s+n_1(E)) + \sigma_p(E)(p_s+p_1(E))} \tag{1.79.b}$$

$$f_d(E) = \frac{\sigma_n(E)n_1 + \sigma_p(E)p_s}{\sigma_n(E)(n_s+n_1(E)) + \sigma_p(E)(p_s+p_1(E))} \tag{1.79.c}$$

where $D_{\mathrm{it,a}}$ ($D_{\mathrm{it,d}}$) is the acceptor-type (donor-type) surface states. An accurate value of Q_{it} is difficult to determine, since it is necessary to know a precise information about the distribution of $D_{\mathrm{it,a}}$ and $D_{\mathrm{it,d}}$ along the bandgap and the dependence of the capture cross section on the energy. In addition, the dependence of S_{eff} at *c*-Si surface on Δn is well explained by a constant charge density present in the passivating materials like SiO_2 or SiN_x that is independent of the illumination level. In some cases the charge provided by the interface states, Q_{it}, is much lower than this fixed charge, so that it can be neglected and equation (1.78) can be re-written as:

$$Q_{Si} + Q_f = 0 \qquad (1.80)$$

Then, a unique value of Ψ_s which equals both charges can be numerically determined. Once Ψ_s is known, n_s and p_s can be calculated using equations (1.72).

Whether such assumption is valid or not depends on the nature of the passivation material. For amorphous silicon carbide an extensive analysis of lifetime curves has been done at UPC assuming a negligible Q_{it} and hence attributing all the charge density to the fixed charge Q_f [32]. However, our last experiments seem to indicate that Q_{it} is not negligible and it might be possible that it has the dominant role in the recombination mechanisms (see Chapter 4 and Appendix I for more details).

Next step is the calculation of U_s where the characteristics of the defects are needed. For simplicity, we assume only one defect located deep in *c*-Si bandgap. Particularly, equation (1.25) can be simplified to (1.24) if we assume this defect at *c*-Si intrinsic energy level, E_i, which is very close to midgap. In this case $n_1 = p_1 = n_i$, and equation (1.24) can be simplified to:

$$U_s = \frac{n_s p_s - n_i^2}{\dfrac{n_s + n_i}{S_{p0}} + \dfrac{p_s + n_i}{S_{n0}}} \qquad (1.81)$$

Finally, S_{eff} is calculated applying equation (1.66). In conclusion, this model allows the calculation of the dependence of S_{eff} on Δn with three free parameters:

- S_{n0}, S_{p0}: they take into account the interface defect density located at *c*-Si intrinsic energy level and the relation between electron and hole capture cross sections.
- Q_f: fixed charge density placed at the interface which is responsible for the induced band bending at *c*-Si surface.

It must be pointed out that the for *p*-type wafers fundamental recombination velocity for electrons S_{n0} cannot be extracted from the measured τ_{eff} (Δn) curves when a field effect passivation is present. Because of the high positive charge in the layer, the surface is under inversion conditions at low injection and, hence, surface recombination is limited by the availability of holes and consequently determined by S_{p0}. This argument can be easily understood when examining equation (1.81). Thus, S_{n0} only impacts τ_{eff} values at high-injection where the band bending at the surface tends to vanish. However, for a high acceptor density at the *c*-Si bulk, as those used in this thesis, Auger recombination is dominant under high injection. As a consequence, from the measurements it is only possible to give a lower limit for S_{n0}. The same argument can be applied for *n*-type wafers and the fundamental recombination velocity of holes, S_{p0}.

1.7.2 Modelling Depletion Region Modulation (DRM) effect

In this section we present detailed explanations of the depletion region modulation (DRM) effect occurring on emitters and on charged insulator-semiconductors interfaces. Since the nature of the effect is slightly different for each case, it must be explained separately. Both effects have been used in this thesis for the simulation of the lifetime curves in order to get more precise information about the saturation current densities in passivated emitters or charge density stored in the passivating films. In both cases, the result for the DRM effect is an increasing tail of the lifetime at low injection densities, as we showed in Figure 1.14.

As we already said in section 1.6.3.1, the nature of the DRM effect comes from a mis-interpretation of the conductivity, leading to apparent carrier density values higher than the actual ones. To model this effect, it is useful to consider that the conductivity given by the sum of two contributions. The first one would be the *flat bands conductivity* considering $\Delta n = \Delta p$. (equation (1.68)), which is the one taken from the Sinton instrument tool to calculate Δn. The second one would be a conductivity factor due to the *band bending*, which is responsible for the distortion in the real lifetime detection.

1.7.2.1 DRM on p-n junctions

We follow the analysis performed in reference [79]. Consider a *p*-*n* junction with a *p*-type base and the emitter located at the surface. In this *p*-type side three different regions are present (see Figure 1.16):

(i) Bulk region. It has an equilibrium carrier concentration of N_A holes and n_i^2/N_A electrons, and a photogenerated excess carrier concentration of $\Delta n = \Delta p$.

(ii) Depletion region. It contains negligible carrier concentrations. The width of this regions changes with the illumination level.

(iii) Modulation region. The modulation region has a negligible background carrier concentration, since this region is depleted of charge carriers in equilibrium. The excess carrier concentration in this region is approximately $N_A/\Delta n$ holes Δn and electrons. The width of this region depends on the excess carrier concentration.

Applying equation (1.67) to the *p*-side considering the three regions the excess conductance is:

$$\Delta\sigma_p =$$

$$= \sigma_{p,light} - \sigma_{p,dark} = q\left[N_A\,\mu_p\right]\left(l_{p,dark} - l_{p,light}\right) + q\left[\Delta n_{light}\,\mu_n + \Delta p_{light}\,\mu_p\right] W \qquad (1.82)$$

where $\sigma_{p,light}$ and $\sigma_{p,dark}$ are the conductances under light and dark conditions, repectively, $l_{p,dark}$ and $l_{p,light}$ are the respective widths of the depletion region under equilibrium (dark) or under illumination. A similar derivation can be obtained for the *n*-type side. Then the total conductivity of the whole wafer resulting for the sum of the *n* and *p* sides is:

$$\Delta\sigma = q\,N_A\left(\mu_p + \mu_n\right)\Delta l_p + \Delta n\left(\mu_p + \mu_n\right) q\,W \qquad (1.83.a)$$

$$\Delta l_p = \left(\sqrt{\left(\Psi_0 - V_A\right)} - \sqrt{\Psi_0}\right)\sqrt{\frac{2\varepsilon}{q}\frac{N_D}{N_A\left(N_A + N_D\right)}} \qquad (1.83.b)$$

$$V_A = \frac{kT}{q}\ln\left(\frac{\Delta n + n_0}{n_0}\right) \qquad (1.83.c)$$

$$\Delta l_n\,N_D = \Delta l_p\,N_A \qquad (1.83.d)$$

Therefore, there is an excess of the conductivity compared to the simple equation (1.68) that is the responsible of overestimating the excess carrier density, and hence the effective lifetime. This effect is noticeable at low Δn values, while it is negligible for mid-high excess carrier densities because the first term in equation (1.83.a) is dominated by the term with Δn. The cross-over point in the lifetime curve is given by:

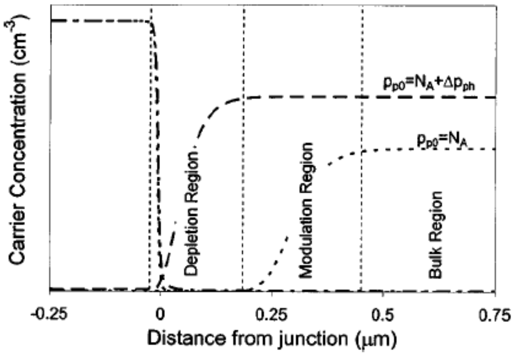

Figure 1.16. Electron and hole carrier concentrations within a n+p junction under illumination, illustrating the three defined regions: depletion, modulation, and bulk regions. Extracted from reference [79].

$$\Delta n \approx \frac{N_A}{W}\Delta l_{p0} \tag{1.84}$$

1.7.2.2 DRM on charged insulators

The DRM on charge insulator-semiconductor interfaces has been analysed at UPC by M. Garín *et al* [80]. The nature of the effect is similar to that found in *p-n* junctions, but it must be calculated separately since the results lead to different expressions.

We depart from the general equation (1.62), which is employed for the determination of the effective lifetime.

For simplicity in the calculations, we consider true-steady-state illumination conditions, whereas a flash decay time of 2.3 ms is used in the physical setup. For the lifetime determination, we consider being true equation (1.68), and therefore we estimate the average carrier density as considering the light and dark conditions:

$$\Delta n_{av} = \frac{\sigma_{light} - \sigma_{dark}}{qW(\mu_n + \mu_p)} \tag{1.85}$$

We have to take into account now that there is a bulk region with *flat bands* and equal concentration of electrons and holes, and a depletion region produced by the charge in the insulator, which originates a *band bending* at the surface. These two regions have their own conductances, being the total conductance the sum of both contributions [77]:

$$\sigma = \sigma_{fb} + 2\sigma_{bb} \tag{1.86}$$

being

$$\sigma_{fb} = qW(n_0 + \Delta n_{bulk})\mu_n + qW(p_0 + \Delta n_{bulk})\mu_p \tag{1.87}$$

the wafer conductance assuming flat bands along the whole wafer, and σ_{bb} the deviation of the conductance from flat band condition due to the surface potential (band bending) ψ_s. We include a factor 2 in equation (1.87) to take into account two symmetrical surfaces. The conductance term σ_{bb} is determined by solving the Poisson equations near the surface. For convenience, the potential ψ_s is used as the integration variable, instead of the position *x*, resulting in [77]:

$$\sigma_{bb}(\Psi_s) = \pm\sqrt{\frac{q\beta}{2}}\int_0^{\Psi_s} \frac{(n_0+\Delta n_{bulk})(e^{\beta\Psi}-1)\mu_n + (p_0+\Delta n_{bulk})(e^{\beta\Psi}-1)\mu_p}{\sqrt{F(\Psi,\Delta n_{bulk})}} \tag{1.88.a}$$

with the auxiliary function *F* defined as:

$$F(\Psi,\Delta n_{bulk}) =$$

$$= (n_0+\Delta n_{bulk})(e^{\beta\Psi}-1)\mu_n + (p_0+\Delta n_{bulk})(e^{\beta\Psi}-1)\mu_p + \beta\Psi(N_A - N_D) \tag{1.88.b}$$

where β is *q/kT*. Prior to the calculation of σ_{bb}, the surface potential Ψ_s is determined by balancing the charge within the semiconductor and the fixed charge Q_f, which is located at the insulator/semiconductor interface.

First, we calculate the surface recombination rate by applying the *extended Shockley-Read-Hall formalism* with input parameters Q_f and Δn_{bulk}. In this calculation we assume a single recombination centre at the *c*-Si midgap with fundamental recombination velocities for electrons and holes, S_{n0} and S_{p0}. For the bulk recombination we assume infinite SRH lifetime and the Auger considered in equation (1.17). The explained calculation of wafer conductivity is performed under dark and illumination conditions. The former is calculated with Δn_{bulk} equal to zero, whereas the latter is performed for a certain Δn_{bulk}. This last value is also used for calculating the corresponding photogeneration rate. Thus, to generate a complete τ_{eff} (Δn_{av}) curve we scan a given range of Δn_{bulk} calculating the corresponding Δn_{av} and τ_{eff} values. Notice that the final Δn_{av} scanned range can strongly vary depending on the DRM effect and, consequently, on the Q_f value.

Analytically, we can rewrite the QSS-PC excess minority carrier density using equations (1.86) to (1.88) as

$$\Delta n_{av} = \Delta n_{fb} + 2\Delta n_{bb} \tag{1.89}$$

where

$$\Delta n_{fb} = \frac{\sigma_{fb,light} - \sigma_{fb,dark}}{qW(\mu_n + \mu_p)} \tag{1.90}$$

is the excess minority carrier density considering flat energy bands along the wafer and

$$\Delta n_{bb} = \frac{\sigma_{bb,light} - \sigma_{bb,dark}}{qW\left(\mu_n + \mu_p\right)} \tag{1.92}$$

is the excess minority carrier density term due to the surface band bending. The term Δn_{fb} is what we expect to obtain in the ideal case, whereas Δn_{bb} is a parasitic term that depends on the variation of σ_{bb} with the illumination, giving rise to the DRM effect. In order to effectively see a *tail* in τ_{eff}, Δn_{bb} must be comparable to Δn_{fb}, which means that light must introduce a significant variation in ψ_{s}. Such a variation is only possible for a highly inverted surface, where the splitting of the quasi-Fermi levels drags the surface potential. Actually, the surface does not need to be inverted under dark conditions, but it must certainly be inverted under illumination. In slightly inverted/depleted or accumulated surfaces, light can not induce a significant variation in ψ_{s} and the effect disappears.

To show how the DRM is sensitive to the charge density, we perform in Figure 1.17 several simulations of a *p*-type wafer varying the parameter Q from 10^{10} to 10^{12} cm^{-2}. The tail starts to be shown at in a very narrow range of Q, between 2 and 3 × 10^{11} cm^{-2}. At 3 × 10^{11} cm^{-2} there is a maximum that in some occasions has been measured (Figure 1.14) and then it rapidly disappears at 5 × 10^{11} cm^{-2} and above. The DRM effect is also very sensitive to the wafer resistivity. Figure 1.18 plots the dependence of the lifetime curves on the acceptor density for *p*-type wafers. Again there is a very narrow range of N_{A} in which a maximum is observed, being in the present case between 1 and 2 × 10^{16} cm^{-3}.

1.8 Chapter conclusions

In this Chapter we have described all the recombination processes present in crystalline silicon solar cells. Models have been presented for each mechanism in order to separate the different contributions. The intrinsic Auger plus radiative recombination has been treated with up-to-date most complete model at 300 K of Kerr and Cuevas [27]. The recombination through defects has been described by the Shockley Read Hall (SRH) theory. When working with high quality silicon wafers a negligible SRH recombination can be assumed. On the contrary, surface recombination has been extensively analyzed by the extended SRH theory. This considers a dielectric film located at the surface that is able to perform surface passivation either by saturating the defects and diminishing fundamental recombination velocities or by establishing a field effect passivation.

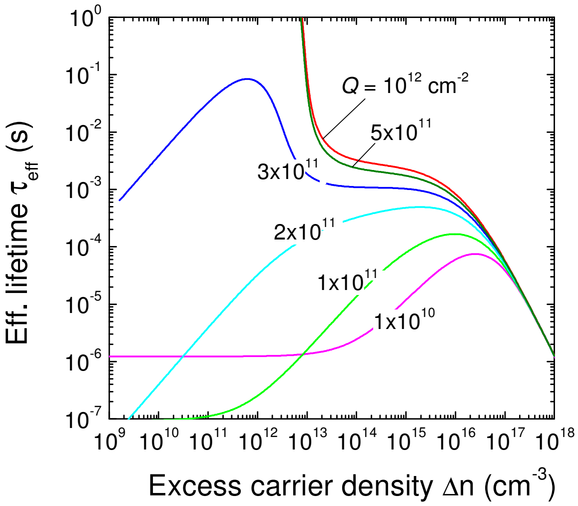

Figure 1.17. Simulations of lifetime curves including DRM effect in a insulator/ semiconductor structure. Assumptions: $N_A = 1.6 \times 10^{16}$ cm^{-3}, $W = 300$ µm, $S_{p0} = 100$ cm s^{-1}, $S_{n0} = 10^4$ cm s^{-1}.

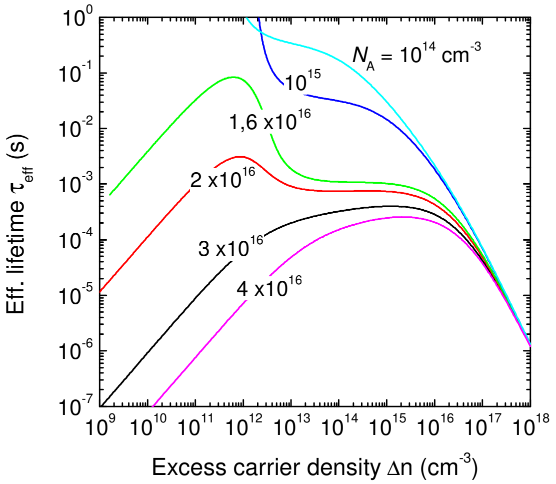

Figure 1.18. Simulations of lifetime curves including DRM effect in a insulator/ semiconductor structure. Assumptions: $Q_f = 3 \times 10^{11}$ cm^{-2}, $W = 300$ µm, $S_{p0} = 100$ cm s^{-1}, $S_{n0} = 10^4$ cm s^{-1}.

Lifetime measurements by Quasi Steady State Photoconductance technique (QSS-PC) has been presented as a powerful tool to characterize the surface recombination velocity and hence the ability of the films to perform crystalline silicon surface passivation. An artifact present in such measurements, Depletion Region Modulation (DRM) has been identified and explored extensively to improve the models and have better determination of the recombianation parameters, especially the amount of charge in the dielectric film that lead to the field effect passivation.

CHAPTER 2

State of the art in surface passivation

2.1 Introduction

An overview of the most important materials and techniques for crystalline silicon surface passivation is presented in this Chapter. Reasons for choosing a particular one depend on several factors. For example, when applied at the front side of the solar cell we require transparency of the film and an appropriate thickness in order to achieve antireflective properties. On the other hand, high refractive indexes (i.e. like in metals) are desired in the rear side in order to reflect the long wavelengths that have reached that side. Other issues to take into account are the quality of the silicon wafer used and the production costs compared to the cell efficiency achieved.

The literature provides many details about passivation on *p*-type bases and n^+-emitters, but results on *n*-type silicon bases or p^+-emitters are rather scarce. The reason is that traditionally the solar industry has focused on *p*-type silicon wafers due to the existence of a higher feedstock of this material from the microelectronic industry. Interest in *n*-type wafers, and therefore in its surface passivation, has recently arisen. The utilization of *n*-type bases has some advantages, for example that passivation of *n*-type surfaces at a given resistivity is easier than in *p*-type bases. Also, *n*-type substrates are free of highly recombinative B-Fe or B-O centres, which appear when low-cost solar-grade silicon is used.

2.2 Thermally grown silicon dioxide (SiO_2)

Silicon dioxide (SiO_2) is one of the most important materials in semiconductor manufacturing, having played a crucial role in the development of semiconductor planar processing. The formation of SiO_2 on a silicon surface is most often accomplished through thermal oxidation.

The thermal oxidation of silicon consists of exposing the silicon substrate to an oxidizing environment at elevated temperature (usually between 700-1300 ºC), producing oxide films. This process can be done in tube furnaces or in Rapid Thermal Anneal (RTA) furnaces. When the environment is O_2 the process is called *dry thermal oxidation* while the process involving H_2O is called *wet thermal oxidation*. The corresponding chemical reactions involved are expressed by:

$$Si + O_2 \rightarrow SiO_2 \tag{2.1}$$

$$Si + 2H_2O \rightarrow SiO_2 + 2H_2 \tag{2.2}$$

Oxidation of silicon is not difficult as long as an oxidizing ambient is present. The elevated temperature used in thermal oxidation therefore serves primarily as an accelerator of the oxidation process, resulting in thicker oxide layers per unit of time. According to the model predicted by Deal and Grove [88] the thickness obtained depends on the root square of the time, the process temperature, the orientation of the crystalline surface, and the atmosphere type. In dry atmosphere the growing rates are very low. For example, to grow a 110 nm thick layer (adequate for antireflective layers on Si) we need to expose the wafer 70 min at 1100 ºC. In wet atmosphere the growing rate is much faster but the electronic properties of the Si – SiO_2 interface are poorer than those provided by dry oxidation. Therefore, in order to achieve good interface properties and thick SiO_2

layers in a reasonably fast process it is common to combine dry and wet thermal oxidation.

From the point of view of surface passivation, silicon dioxide works mainly by reducing the density of states at the interface. Analysis of the charge density reveal that there is a positive fixed charge density within the dielectric layer with a value around 3×10^{11} cm^{-2} [89], combined with a density of states that are negatively charged. Altogether causes a weak field effect passivation, leading to similar populations of electrons and holes in excess at the interface and therefore to increasing SRH recombination assisted by defects. For this reason, wafer cleaning step prior introducing the wafer in the furnace is a crucial process. The standard procedure in microelectronics for wafer cleaning is the so-called *RCA* cleaning, which last step is a HF dip to remove the native oxide.

The value of the fixed charge density in the SiO_2 is not intrinsic to the material. Sai *et al.* studied the charge values for different growing conditions [90], measuring low values for dry oxidation ($2 - 10 \times 10^{10}$ cm^{-2}), significantly higher values for wet oxidation ($2 - 4 \times 10^{11}$ cm^{-2}), and really high values for Chemical Vapour Deposition ($> 10^{12}$ cm^{-2}). Regardless the technique used, the value of the fixed charge resulted to be approximately proportional to the density of states at midgap position, $D_{\mathrm{it,midgap}}$. However, higher Q_{f} values, which would cause higher field effect passivation, are not beneficial to the surface passivation. On the contrary, surface passivation gets worse as Q_{f} increases due to the increment of $D_{\mathrm{it,midgap}}$. This is the reason why the lowest effective surface recombination values are obtained for dry thermal oxidation.

To improve further surface passivation so-called Forming Gas Anneal (FGA) treatment is applied after oxidation is complete. This treatment consist of exposing the passivated wafer to a H_2(5%)/N_2(95%) atmosphere at 400 °C for a concrete period of time, normally 30 minutes. The hydrogen present in this atmosphere diffuses easily towards the interface and saturates most of the remaining dangling bonds, thus leading to a reduction of the interface states density. A further and almost complete saturation of dangling bonds is performed by atomic hydrogen with what is called the *Al-anneal* treatment. This consists of evaporating aluminium film over the SiO_2 followed by an annealing at 400 ºC for about 20 minutes. During this anneal, atomic hydrogen is created from the oxidation of the aluminium by water molecules formed during the SiO_2 growth.

The best results of thermally grown surface passivation allow S_{eff} values below 10 cm s^{-1} for both *n*- and *p*-type high resistivity wafers (> 100 Ω cm) [91,92]. For lower resistive wafers this excellent surface passivation is still providing very good results (on *p*-type silicon $S_{\mathrm{eff}} < 20$ cm s^{-1} for 14 Ω cm [90] and $S_{\mathrm{eff}} = 41$ cm s^{-1} for 0.7 Ω cm [93] are achieved). In such resistivity range silicon is used as base in electronic devices. The surface passivation properties of silicon dioxide in these cases have been overcome by materials based on amorphous silicon thanks to field effect passivation (see next section). The contrary is occurring when heavily doped regions are involved to be used as emitters. In these regions the impurities are diffused in the wafers forming a layer around 1 μm thick with doping densities exceeding 10^{18} cm^{-3}. A *p-n* or a *high-low* (p-p^+ n-n^+) junction is then built, providing already a field effect passivation. Therefore, the field effect passivation provided by the passivating layer has a minor role and the way to further reduce recombination is by reducing interface state density. Thermally grown silicon dioxide is so far the best material to provide such reduction of defects. In Figure 2.1 we plot the surface recombination velocity of phosphorus doped bases and emitters as a function of the doping density at the interface for silicon dioxide with FGA and Al-anneal treatments. The results have been extracted from reference [28].

The trend shown in Figure 2.1 is actually a general trend for all surface passivation strategies, i.e. the surface recombination velocity increases with doping density due to a higher presence of defects introduced at the interface.

The study of boron p^+-type emitter passivation is more recent and with scarce results, since until the present days the use of such emitters was not as spread as the use of n^+-type emitters in the photovoltaic field. One of the most relevant results is found again in reference [28]. Boron emitters with different resistivities received thermal oxidation, some of them with trichloroethane (TCA) gas in the oxidizing atmosphere. Excellent passivation was achieved, with low values of the minority saturation current density (for example for 100 Ω/sq J_{0e} was around 30 fA cm^{-2}). However, after storing the samples in the dark for two years [94], J_{0e} increased severely, but could be lowered to the initial values by a FGA at 400 ºC. The samples that received no TCA had similar initial passivation quality as with a TCA, but it was not possible to recover the degradation with the FGA treatment.

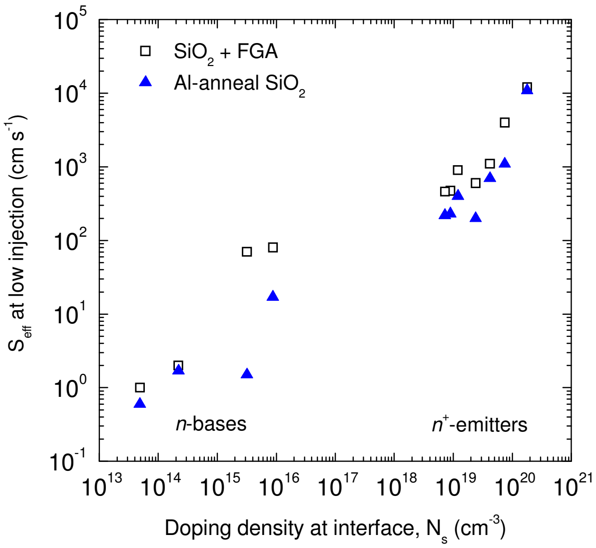

Figure 2.1. Surface recombination velocity of phosphorus doped bases and emitters as a function of the doping density at the interface provided by thermally grown silicon dioxide. Extracted from reference [28].

The principal drawback of thermal oxidation to be applied in solar industry is the high cost implied, as the temperatures involved range between 900 – 1100 ºC. The temperature itself can be an inconvenient for low cost multicrystalline substrates, which can suffer from degradation. Another problem is the low growing rates. Rapid Thermal Oxidation (RTO) or silicon dioxide grown by plasma equipments help to diminish these costs, but usually offer poorer surface passivation properties. In these sense, promising results have been obtained recently by Hoex *et al.* [95]. They developed SiO_2 films deposited by means of Expanding Thermal Plasma (ETP) technique at high deposition rates in the range of 0.4 – 1.4 μm min^{-1} using an argon/oxygen/octamethylcyclotetrasiloxane (OMCTS) gas mixture. These plasma-deposited SiO_2 films yielded effective surface recombination velocities as low as 54 cm s^{-1} on 1.3 Ω cm n-type silicon after a 15 min Forming Gas Anneal at 600 °C.

From the point of view of application to working devices SiO_2 provides the highest efficiencies because the combination of optical properties and electrical quality optimize the cell efficiency. It was effectively used in the world-record efficiency c-Si solar cell produced by the University of New South Wales achieving solar cell efficiencies of 24.0% [96] at standard test conditions (AM 1.5 25 ºC) with the concept of PERL (Passivated Emitter Rear Locally diffused) cell. With the same concept of cell the efficiency was later improved up to 24.7% [3], which is the present efficiency record of crystalline silicon solar cells working at 1 sun illumination.

2.3 Amorphous silicon-based compounds

Amorphous silicon-based compounds have been suggested as alternatives to thermally grown SiO_2 for surface passivation, since they offer low cost production and scalability to large area implementations. The presence of silicon helps to adjust the lattice constant, so that the density of voids and hence the density of dangling bonds is highly reduced. Between such compounds we can find amorphous silicon (*a*-Si), silicon nitride (*a*-SiN_x), silicon carbide (*a*-SiC_x), and non-thermally grown silicon oxide (SiO_x). Their stoichiometry varies on the deposition conditions, and affects strongly the optical and electronic properties. Materials with a high content of silicon present strong optical absorption in the visible-ultraviolet range, with low conductivity compared to crystalline silicon (for example, in silicon carbide conductivity is around 10^{-6} S cm^{-1} at room temperature [97]). When the content of silicon is low, light absorption and conductivity decrease, thus exhibiting transparency and very good dielectric properties.

The methods to produce such films are normally based in decomposition of hydrogenated gases. This ensures a high content of hydrogen that contributes to improve the surface passivation by saturating dangling bonds. And at the same time this hydrogen is beneficial for the passivation of defects in the bulk of low-quality solar-grade silicon. Plasma Enhanced Chemical Vapour Depositions (PECVD) is the most studied of those methods, and it is also the technique used in this thesis to grow amorphous silicon carbide.

Plasma Enhanced Chemical Vapour Deposition (PECVD) consists of the deposition of a film from a precursor gas mixture whose molecules are broken by means of an electric field. The gas excitation to produce the plasma is placed between the two electrodes that cause such electric field. Depending on the excitation source we can distinguish between Radio Frequency (RF) working at low frequencies (between 10 - 500 kHz), high frequency (normally 13.56 MHz) or even microwave frequencies. The instruments can also be divided in direct configurations, in which the wafer is placed in contact with the plasma, or remote configurations, in which the plasma and the wafers

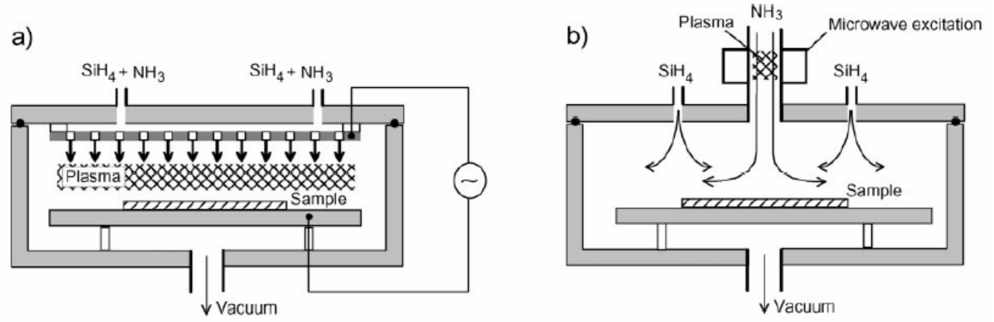

Figure 2.2. (a) Direct-plasma reactor excited through a RF source and (b) Remote-plasma reactor using microwave excitation. Extracted from reference [98].

are located in different chambers. A schematic of both configurations is shown in Figure 2.2 (extracted from Ref [98]), using in this case silicon nitride films. This material is produced by the decomposition of silane (SiH_4) and ammonia (NH_3) gases. In direct configurations both gases are excited, while in remote configurations the silane is introduced directly in the deposition chamber and reacts with the decomposed atoms of nitrogen and hydrogen coming from the excitation chamber. The plasma excitation frequency has a strong impact on the electronic properties of the resulting film-silicon interface. The reason is that below the so-called plasma frequency (< 4 MHz) ions are able to follow the plasma excitation frequency and therefore produce a strong surface bombardment. Due to the resulting surface damage, films fabricated with low-frequency direct PECVD only provide an intermediate-quality surface passivation on silicon surfaces. Fortunately, this problem can be largely eliminated as for excitation frequencies above 4MHz the acceleration periods are too short for the ions to absorb a significant amount of energy. Hence, films prepared by direct PECVD at high frequency (13.56 MHz) provide a much better surface passivation than films prepared at low frequency. The introduction of a remote chamber improves even more the quality of surface passivation, as no ion bombardment is produced in the wafer.

Other relevant deposition techniques in development for passivation films are Sputtering and Hot Wire Chemical Vapour Deposition (Hot Wire CVD). Sputtering technique belongs to the Physical Vapour Deposition (PVD) family. The principles of deposition are based on bombarding a solid silicon target with ions coming from a plasma excited gas. The principal advantage of sputtering in industry is that no silane gas is used. This is very convenient because silane is explosive. It also has the benefit of producing highly uniform films in composition and thickness in very large areas. Hot Wire CVD is based on the decomposition of gases using high temperatures (around 1600 ºC). No plasma and no voltage are applied inside the chamber and therefore there is no damage in the silicon wafer coming from ion bombarding.

2.3.1 Amorphous silicon nitride

Amorphous silicon nitride is the present state of the art in surface passivation of crystalline silicon solar cells. Extensive research has been led during the last two decades, producing silicon nitride films that offer excellent surface passivation, transparency and antireflective properties, stability under ultraviolet light exposure and under high thermal treatments. Good synthesis of important results about silicon nitride passivation can be found in relevant publications [28,42].

Preliminary studies indicated that the surface passivation improved as the fraction of silicon in the film increased. This led to higher refractive indexes and therefore to higher extinction coefficients, with some absorption of light within the film that did not contribute to the photocurrent. The introduction of molecular nitrogen (N_2) gas in the PECVD system, apart from silane (SiH_4) and ammonia (NH_3), produced transparent layers with record low values of surface recombination velocity. For low resistivity *p*-type wafers this passivation scheme was able to achieve S_{eff} values lower than 10 cm s^{-1} with a conventional PECVD in direct configuration.

Silicon nitride passivates mainly by the field effect provided by a high fixed charge density. When the films are dielectric enough, Capacitance-Voltage (*C*-*V*) measurements of MIS structures are useful to determine the density of states, D_{it}, and the fixed charge, Q_{f} in the film. Elmiger and Kunst [56] determined a rather small density of states $D_{\mathrm{it}} = 5 \times 10^{11}$ eV^{-1} cm^{-2} and a very high fixed charge density $Q_{\mathrm{f}} = 3 \times 10^{12}$ cm^{-2}. Since D_{it} was much smaller than Q_{f}, the contribution of the charge coming from the interface states could be neglected. In the same work they used contactless microwave conductivity measurements to determine that charges at the SiN_x film are located within 20 nm of the interface. On the other hand, the dependency of the charge density value on the light intensity was a controversial discussion. Dauwe *et al.* applied corona charge measurements to clarify that the value of the charge was constant at $Q_{\mathrm{f}} = 2.5 \times 10^{12}$ cm^{-2} and independent of the light intensity [99].

The level of passivation of silicon nitride can be improved by using remote PECVD plasma to avoid ion bombardment. This is actually the current trend in the photovoltaic industry. Another strategy that improves the use of silicon nitride is to perform thermal oxidation before the SiN_x deposition. The SiO_2 provides a low interface density and the SiN_x provides an extra field effect. The combination of such stacked films on *p*-type, 1 Ω cm wafers resulted in S_{eff} values lower than 3 cm s^{-1} [100]. The same approach was tried applying Rapid Thermal Oxidation (RTO) and SiN_x deposition with only slightly worse results [101]. Another result combining silicon dioxide and silicon nitride stacks was provided by Hao, et al [102]. In this case, they performed stacks of thermally grown SiO_2 and stoichiometric Si_3N_4 grown by LPCVD at 775 ºC. Without oxide, the LPCVD silicon nitride caused serious irreversible bulk damage to silicon wafers after a high temperature treatment. A thin oxide, about 10 nm, helped to reduce the damage. A thick oxide (more than 50 nm) helped to completely eliminate the bulk damage. On *p*-type high resistivity wafers (100 Ω cm) values of S_{eff} lower than 2 cm s^{-1} were achieved.

Some research was intended to achieve surface passivation by means of sputtering [103,104]. With an inline sputtering system (ATON series, manufactured by Applied Films) it was possible to reach 30 cm s^{-1} on *p*-type 1 – 2 Ω cm wafers [105].

In silicon nitride passivation schemes the evolution of lifetime with annealing after deposition has been extensively studied. The effective lifetime vs. annealing time curves usually reach a maximum followed by decay and then saturate. As the temperature process increases, the peak becomes narrower and is located at shorter annealing times [28,106]. This represents a big benefit in screen printed solar cells. Screen printing is an industrial process in which the metal pastes are printed on the wafers through a mesh to define the front grid and the rear metallic area. The wafers are subsequently fired at typical temperatures between 700 – 900 ºC for a few seconds. Since surface passivation is performed before the metallization, it is desirable that the films applied keep or enhance their properties after the screen printing process. The improvement phenomenon, however, depends on the silicon nitride composition. Schmidt *et al* [107] showed that films with a refractive index equal to 2.1 enhanced the wafer effective lifetime after a short treatment at 900 ºC, while when the index was slightly higher (n = 2.4) and therefore a bit more rich in silicon, the tendency was inverted. Recently, an anomalous behaviour was observed [108], with two local maxima in the curves, when the wafers were heated up at temperatures higher than 650 ºC in an RTA furnace. Several mechanisms were considered for this phenomenon, but the best explanation seems to be offered by a densification of silicon nitride films accompanied by different dissociation rates of the Si-N, Si-H and N-H bond densities.

Concerning the boron emitters, surface passivation was tried by means of silicon nitride stacks in reference [28]. The lifetime curves showed a strong dependence with the injection density, and therefore the saturation current density J_{0e} could not be extracted from the diffusion diode model. To solve this problem, the passivation level was determined through values of the implied open circuit voltage, V_{oc}. Apart from this anomalous behaviour, a de-passivating effect was observed, attributed to the high charge density stored in the silicon nitride films. In other words, what is a benefit for the surface passivation of bases resulted detrimental for heavily doped regions that were also building a field effect.

2.3.2 Amorphous silicon

Hydrogenated amorphous silicon, *a*-Si:H is produced from the decomposition of silane, with optional addition of molecular hydrogen (H_2). This leads to intrinsic layers with low conductivity. Nevertheless, the films can be *n* or *p*-type doped by introducing phosphine (PH_3) or diborane (B_2H_6) as precursor gases together with the silane.

This material has been widely studied for several applications in the microelectronics industry. The principle of passivation of amorphous silicon is based on defects saturation, like silicon oxide. To provide such low interface states density good hydrogenation of the interface is critical. However, if the substrate temperature is too high hydrogen effusion may occur due to the high mobility of this atom or molecule, leaving remaining dangling bonds at the interface and therefore diminishing the surface passivation quality. In general, it is accepted that a temperature lower than 230 °C is sufficient to avoid such hydrogen effusion. Excellent results of surface passivation using amorphous silicon can be found for example in reference [109]. In that work, surface recombination values as low as 3 cm s^{-1} were achieved in 1.5 Ω cm wafers by amorphous silicon films grown by conventional PECVD at 225 °C, which were then applied at the rear side to manufacture a 20.1% efficient crystalline silicon solar cell. Amorphous silicon can be also grown by Hot Wire CVD. For example, D. Muñoz *et al.* reported implied open circuit voltage near

700 mV after surface passivation of *p*-type 0.8 Ω cm wafers, with S_{eff} around 15 cm s^{-1} [110].

The main problem of amorphous silicon is its instability under thermal steps, which are required for firing the screen printed metals. Also, there is a light induced degradation (the Staebler-Wronski effect) associated with the relatively high diffusion coefficient of hydrogen and the changes in local bonding coordination promoted by hydrogen [111]. Developing amorphous silicon at relatively higher temperatures could lead in principle to more stable films under post annealing effects. This was tried, for example, by means of the Expanding Plasma Technique, in which amorphous silicon grown at 400 ºC led to excellent surface passivation in 1.9 Ω cm *n*-type silicon, achieving S_{eff} between 7 and 15 cm s^{-1} at interesting deposition rates higher than 1 nm s^{-1} [112]. After a FGA treatment at 400 ºC the effective recombination velocity increases significantly at about 60 cm s^{-1}, which is a value significantly higher but that can be still considered in the level of good surface passivation.

Another attempt to provide more stability to amorphous silicon could be by introducing a diffusion barrier for hydrogen, thus avoiding its effusion out of the interface. If in addition the barrier is transparent then it could be applied as an antireflective layer at the front side of the solar cell. The approach is probably not interesting in phosphorus doped emitters, as passivation in these cases is solved by silicon nitride. However, this could be a good application in boron doped emitters. In this sense, in reference [113] stacks of a-Si/a-SiN_x films were used to passivate the same configuration of *p*-type emitters explained in reference [94] (section 2.2). Both layers were grown by PECVD at a low temperature (230 ºC) to optimize the passivation properties of the amorphous silicon layer, and subsequently annealed shortly at 350 ºC. The passivation level achieved was as good as that achieved by the thermally grown oxide, without observing increment of J_{0e} after accelerated degradation experiments in UV light.

Finally, it is important to comment that amorphous silicon has been used in solar cells not only as surface passivation layer, but as active part of the device acting as emitter. A good example can be found in the so-called Heterojunction with Intrinsic Thin-layer (HIT) structure, developed by Sanyo Electric Co, with impressing open-circuit voltages over 700 mV and efficiencies exceeding 21% in laboratory cells and over 19%

for mass produced solar cells [114]. In this device a *n*-doped crystalline Si bulk is used as base, a very thin (5 nm) intrinsic *a*-Si:H buffer reduces interface recombination and a p^+-doped layer acts as emitter.

2.3.3 Amorphous silicon carbide

Amorphous silicon carbide, *a*-SiC_x is produced from the decomposition of silane and methane (CH_4) and like amorphous silicon it can be phosphorus or boron doped using phosphine or diborane gases.

To our best knowledge, the earliest work reporting crystalline silicon surface passivation by means of *a*-SiC_x was provided in our group by I. Martín *et al* [115]. In that work intrinsic *a*-SiC_x(*i*) films were deposited in 3.3 Ω cm *p*-type wafers, achieving surface recombination values as low as 30 cm s^{-1}. The results were further improved using phosphorus doped films *a*-SiC_x(*n*) [116].

The quality of passivation depends strongly on the deposition parameters. In the case of silicon carbide developed in our group it was found that surface passivation improves with increasing temperatures, as Figure 2.3 shows. The silane to methane gas flow ratio has also a strong impact in the surface recombination velocity. It can be seen in Figure 2.4 that S_{eff} is minimized for intrinsic and phosphorus doped films at a methane to silane ratio that is close to the unity. Despite this approximately one to one incorporation of silicon and carbon atoms in the chamber, the composition of the films appears to be rich in silicon. Indeed, optical band gap for this composition are around 1.8 eV (see Fig 2.5), value that is close to that for amorphous silicon. The explanation for this effect is that the plasma was created in the so-called *starving plasma* conditions. In those conditions the RF power density is able to break SiH_4 molecules whereas the CH_4 molecules are not affected due to their higher stability. Hence, all the carbon atoms incorporated to deposited films come from secondary reactions between SiH_4 radicals and CH_4 molecules.

Ultimately, some photovoltaic research groups have looked at silicon carbide as an attractive option to keep in mind. Part of the interest is focused in the possibilities for boron doped emitter passivation. By means of boron doped stacked silicon carbide films, R. Petres *et al.* achieved good surface passivation of such heavily doped regions [117].

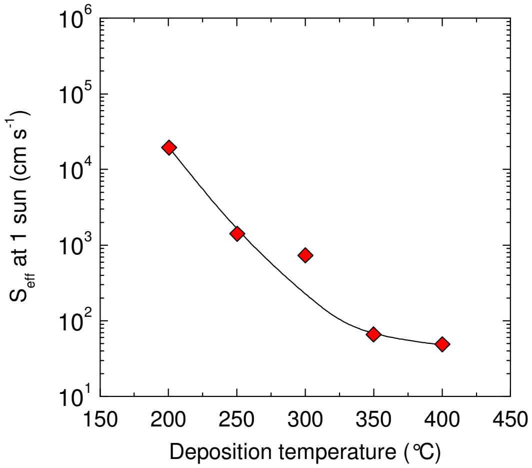

Figure 2.3. Surface recombination velocity provided by intrinsic amorphous silicon carbide as a function of the deposition temperature. Extracted from reference [32].

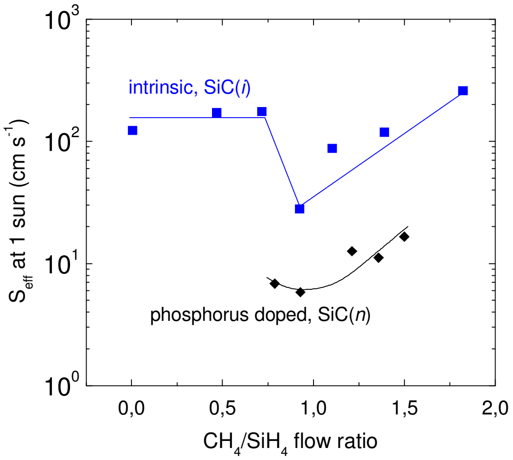

Figure 2.4. Surface recombination velocity provided by amorphous silicon carbide as a function of the methane to silane flow ratio. Comparison between intrinsic and phosphorus doped amorphous silicon carbide films. Extracted from reference [32].

Figure 2.6 illustrates the effective lifetime measured in that work for different passivation configurations. It can be seen that only thermally grown silicon oxide provides better properties that silicon carbide, while for silicon nitride there is a de-passivation behaviour with lifetimes even lower than the non-passivated emitters.

Other relevant results with silicon carbide are provided for example by Coscia et al [118]. They developed intrinsic and carbon rich SiC in a direct PECVD reactor to be applied on *p*- and *n*-type silicon of 1 Ω cm. Hydrogen dilution in the gas mixture was

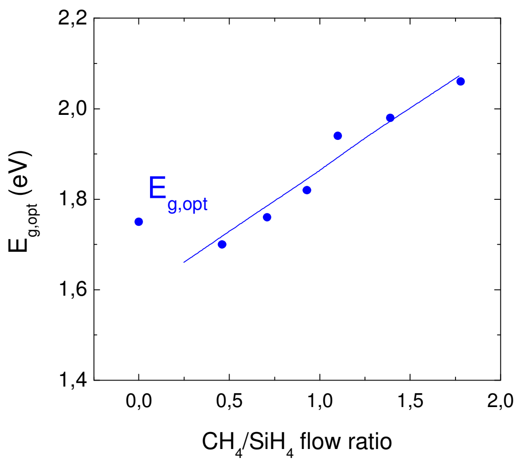

Figure 2.5. Optical gap of amorphous silicon carbide the methane to silane flow ratio. Extracted from reference [32].

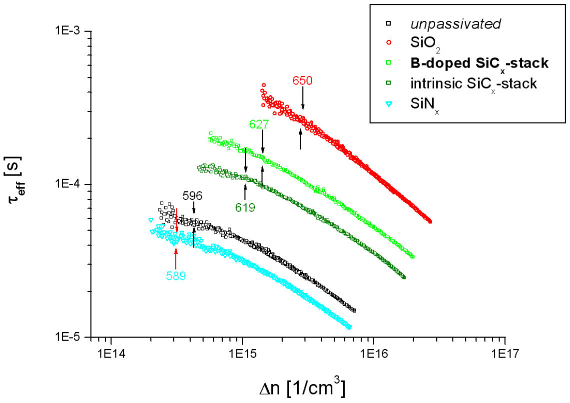

Figure 2.6. Overview of the best results with PECVD-SiC$_x$ on 90 Ω/sq p^+-type emitters on 2.8 Ω cm n-type Cz to PECVD-SiN$_x$ and 10 nm thin thermal SiO$_2$. Arrows indicate 1 sun illumination, numbers at arrows display the corresponding implied V_{oc}. Extracted from reference [117].

used to improve the carbon incorporation in the films and to produce lower microvoids density. Consistently with our results [115,119], the passivation achieved for intrinsic carbon rich films is relatively low (S_{eff} < 300 cm s^{-1}). When depositing silicon nitride films on top of the SiC layer, forming stacks, the passivation improved due to the extra field effect provided by the high charge density in the nitride.

2.3 Aluminium back surface field

Back surface field (BSF) consist of creating a high-low junction, i.e. p-p^+ or n-n^+ at the rear side of the solar cell (depending on the doping type of the substrate) that builds a field effect passivation. It is common to diffuse boron or phosphorus to create the p-p^+ or n-n^+ junctions, respectively. However, for the p-p^+ junction the use of aluminium is much widely spread.

Aluminium is a standard material for contacting silicon. Aluminium-silicon alloy is produced at a relatively low temperature of 577 °C (the eutectic temperature), with aluminium acting as a p^+ acceptor. This property is used in to create an already contacted p-p^+ junction. The properties of the aluminium BSF are optimal for industrial solar cells: in a very simple step it provides good contact, field effect passivation and reflection at the rear side, increasing light absorption. However, the maximum open circuit voltage provided by this structure is around 630 mV, which is insufficient to reach very high efficient solar cells.

2.4 Chapter conclusions

The principal materials used for crystalline silicon surface passivation are reviewed. Silicon oxide and amorphous silicon base their strategy in direct reduction of interface states density, silicon nitride and the so-called aluminium back surface field are based mainly on field effect passivation, and finally silicon carbide appears to use both strategies in a similar level. Regardless the material used, the surface recombination velocity normally increases with the surface doping due precisely to a major presence of defects at the interface.

For silicon carbide, the optimum deposition parameters used in our group are summarized and will be used in the following Chapters as starting point to improve surface passivation.

CHAPTER 3

Single phosphorus doped a-SiC$_x$(n):H films

3.1 Introduction

An extensive work has already been realized at the Electronic Engineering Department, UPC, developing amorphous silicon carbide films for the surface passivation of crystalline silicon. PECVD parameters (flow gas ratios, temperature, and total pressure) were widely varied to obtain optimum deposition conditions that minimized the surface recombination velocity [32]. It was found that passivating properties of phosphorus doped films were much better than the intrinsic ones, as mentioned in Chapter 2. However, further investigations are required for better understanding of the physical properties of the a-SiC$_x$/c-Si system, but also to fit its applicability to the industrial processes of solar cells manufacturing. Related to the first issue, it would be important to determine the value of the charge density, Q, allocated in the amorphous films and its dependence with important parameters, as the film composition, film thickness and wafer resistivity. For the second concept, the deposited films should keep high uniformity in large areas, and stability under high temperature steps, normally used in the solar cell fabrication. For applications to the front side of the solar cells high transmission of the films is also required. Another important issue concerns the doping of the wafer to be used. In solar cells it is convenient to use wafers with low resistivities to achieve high open circuit voltages. At the same time, the resistivity values have to be high enough to ensure a sufficient diffusion length of carriers, so that they can reach the contacts once they are generated. Therefore, it is common to use wafers with resistivites around 1 Ω cm or lower. This involves a relatively high doping that introduces more defects on the network, being more difficult to passivate. Hence, the passivation films have to demonstrate their capabilities on such surfaces.

In this Chapter we focus our attention on phosphorus doped *a*-SiC$_x$(*n*):H films for the passivation of low resistivity *p*-type wafers, starting at the point of optimum composition determined in reference [32]. That composition is rich in silicon, leading to relatively low values of the optical bandgap (around 1.8 eV) and presenting a significant absorption of the visible light. Therefore, the applicability of the films is focused on rear side passivation of solar cells. The main parameters analyzed are the total pressure in the chamber, the radio frequency (RF) power and the film thickness. Finally, optimized silicon carbide films have been applied to wafers of different resistivities. In all cases the quality of passivation has been determined through lifetime measurements by QSS-PC technique. The $\tau(\Delta n)$ curves have been analyzed in order to extract the recombination parameters mentioned in Chapter 1.

3.2 Wafer cleaning

Contaminants present on the surface of silicon wafers have to be removed in order to obtain high performance and high reliability semiconductor devices, and to prevent contamination of process equipment. Along this thesis, two cleaning methods have been employed:

- *Piranha* cleaning.

It consists of a 2:1 H_2SO_4:H_2O_2 solution. This mixture generates an exothermal reaction which boils spontaneously. The silicon wafer is immersed in it for 10 minutes, in which the first monolayers are oxidized. Afterwards the wafer is rinsed under water and immediately dipped in a 20:1 H_2O:HF solution for 10 seconds. The native oxide grown is removed and the wafer comes out dry because of the hydrophobic character of the non-oxidized surface.

- *RCA* cleaning.

The RCA clean is the standard for removing contaminants from wafers in the microelectronic industry. Kern and Puotinen developed the basic procedure in 1965 while working for RCA (Radio Corporation of America) [43]. It has four steps used sequentially:

I. Organic Clean: Removal of insoluble organic contaminants with a 5:1:1 H_2O:H_2O_2:NH_4OH solution boiling for 10 minutes at 75 °C.

II. Oxide Strip: Removal of a thin silicon dioxide layer where organic contaminants may accumulated as a result of I, dipping the wafer in a 40:1 H_2O:HF solution.

III. Ionic Clean: Removal of ionic and heavy metal atomic contaminants using a solution of 6:1:1 H_2O:H_2O_2: HCl for 10 minutes at 75 °C.

IV. Oxide Strip: Removal of a thin silicon dioxide layer where metallic contaminants may accumulated as a result of III, dipping the wafer in a 40:1 H_2O:HF solution.

During these two processes silicon is not etched, and only a very thin layer of silicon dioxide is removed during the HF dip. When finished, the surface is completely dry and without residues.

3.3 Thickness measurements by profilometry

Thickness characterization is of paramount importance for the deposited films. In the particular case of silicon carbide, surface passivation is improved with increasing film thickness. It is also desirable to control the deposition rate and the uniformity for the applicability to industrial processes. Ellipsometry and profilometry are employed in this thesis to measure *a*-SiC$_x$ films thickness.

Two types of profilometers were employed along this thesis: KLA Tencor and Dektak 3030 Sloan Inc. The thickness of the films developed lay below 200 nm. In such small nanometric scale, measurements would be difficult in a single step. Therefore, silicon samples with evaporated Al strips (around 500 nm high) separated 100 μm were

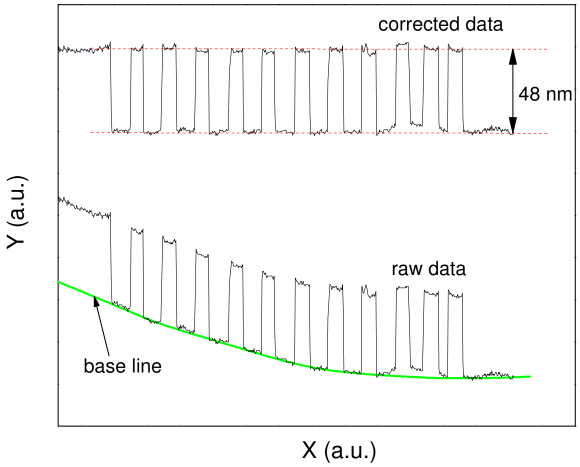

Figure 3.1. Profilometry measurement and base correction for determination of *a*-SiC$_x$ film thickness.

Table 3.1. Optimal PECVD parameters for the deposition of *a*-SiC$_x$(*n*):H films applied at the passivation of 3.3 Ω cm wafers in Ref [32], and the studies performed in this Chapter for 0.85 Ω cm wafers

	SiH$_4$+PH$_3$ (sccm)	CH$_4$ (sccm)	temperature (ºC)	total pressure (mTorr)	RF power (W)	deposition time (min)
standard process for 3.3 Ω cm	29.5	24.3	400	300	15	5
this work	unaltered	unaltered	unaltered	250 – 450	15 – 90	1 – 12

introduced in the PECVD reactor at every deposition. Afterwards, the Al was stripped with HCl in a lift-off process, remaining only *a*-SiC$_x$ strips. Due to the silicon wafer curvature, it is necessary to perform a base correction before determining the thickness. The detail can be observed in Fig 3.1.

3.4 Surface passivation of 0.85 Ω cm *p*-type *c*-Si

The present section is focused on the surface passivation of low resistivity, planar silicon wafers. The substrates used were Float Zone, <100> oriented, *p*-type, 0.85 Ω cm, double side polished, 400 μm thick. As the wafers were new and had already a RCA cleaning step from the manufacturing company, a piranha cleaning was considered to be sufficient to achieve good initial preparation of the surface.

The silicon carbide films developed in this thesis are deposited by a PECVD system (Plasmalab DP-80 from Oxford Instruments) working in direct configuration at high RF frequency (13.56 MHz). The parameters of the deposited films can be selected by the user to produce the desired effect on the surface passivation. These are:

- Gas flows of the precursor gases: silane (SiH_4), phosphine (PH_3) and methane (CH_4)
- Total pressure of the chamber
- Substrate temperature
- RF power density
- Deposition time

Symmetrical PECVD depositions were performed in order to measure the effective lifetime. Before the second deposition the wafers were dipped again in HF. To start our analysis of surface passivation on 0.85 Ω cm wafers, we depart from optimum conditions already found in references [32] and [115] for 3.3 Ω cm. These previous experiments indicate that the silicon rich composition is crucial to achieve good surface passivation, as well as a relatively high deposition temperature (400 ºC). Therefore, these parameters are kept unaltered, while total pressure in the chamber, RF power and deposition time are systematically varied. Table 3.1 summarizes the process developed in this Chapter.

3.4.1 Dependence on chamber pressure

In this section we fixed the RF power at 15 W and the deposition time at 7 minutes. A variation of the total pressure in the chamber was done. After the second side deposition, the wafers were immediately subjected to a Forming Gas Anneal treatment at 430 ºC for 30 minutes to improve the surface passivation. From lifetime measurements we extracted values of effective recombination velocity at 1 sun illumination, using the equation:

$$\frac{1}{\tau_{eff}} = \frac{1}{\tau_{bulk}} + \frac{2S_{eff}}{W} \tag{3.1}$$

As explained in Chapter 1, the high bulk lifetime of the wafers and the good surface passivation provided by the amorphous silicon carbide films make this equation an excellent approximation to the real value of S_{eff}. We only considered Auger lifetime in the determination of τ_{bulk}, since we used high-quality Float Zone (FZ) *c*-Si wafers. Therefore, recombination SRH recombination through defects in the bulk can be neglected.

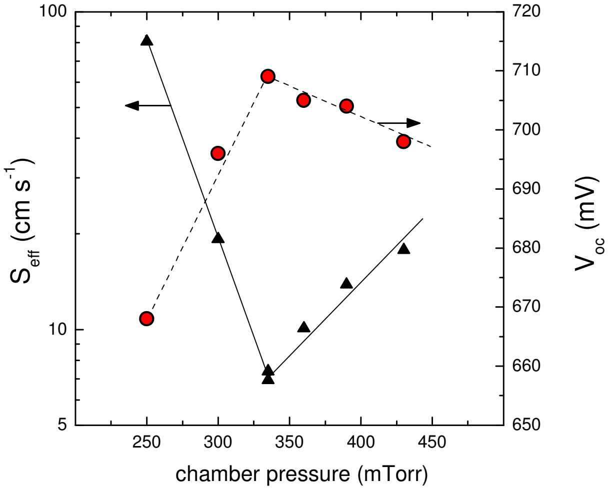

Figure 3.2. Surface recombination velocity (S_{eff}) and implied open circuit voltage (V_{oc}) for *p*-type *c*-Si, 0.85 Ω cm, 400 µm thick wafers, passivated by silicon rich *a*-SiC$_x$(*n*):H films. The growing conditions are specified in Table 3.1. An optimum point is found at 335 mTorr, with S_{eff} = 7 ± 2 cm s^{-1} and V_{oc} up to 709 mV.

Particularly, we used Auger lifetime parameterization suggested by Kerr *et al.* [27], which is described in equation (1.17).

Fig 3.2 plots the values for the surface recombination velocity at 1 sun illumination as a function of the total pressure in the chamber, showing a minimum of $S_{eff} = 7 \pm 2$ cm s^{-1} at 335 mTorr. The implied open circuit voltage, V_{oc}, at 1 sun illumination is also presented in this Figure. This parameter is calculated from the QSS-PC data and represents an upper limit for the open circuit voltage in a working solar cell. It is shown that very high V_{oc} values, up to 709 mV, can be achieved when combining low resistivity wafers with silicon carbide passivation. Despite the quality of passivation is good in all cases (S_{eff} is kept below 100 cm s^{-1}, while V_{oc} is above 660 mV) there is a narrow range in pressure to get really low values of the surface recombination velocity.

In order to get fundamental information of the recombination and passivation mechanisms, the corresponding lifetime curves were simulated using the fitting routine developed at UPC by M. Garín and I. Martín [80], which employs the Girisch model to extract the charge allocated in the layer and the fundamental recombination of holes S_{p0} [86]. The fitting routine includes the Depletion Region Modulation (DRM) effect, favouring the accuracy in the determination of charge density. Optionally, it can be switched off for those cases in which a constant bias light is applied. As explained in

Chapter 1, the DRM effect is partially masked under these conditions. At the time of performing the experiments varying the pressure, our QSS-PC set-up was not covered, so that a bias light was constantly illuminating the measured wafers. Therefore, simulations are presented without incorporating DRM effect, reducing slightly the accuracy in the determination of the charge density. Figure 3.3 shows an example of lifetime measurement for the best *a*-SiC$_x$(*n*) surface passivation obtained for this resistivity, together with the simulated curve and the parameters extracted. The corresponding bulk lifetime at 1 sun illumination provided by the Auger and the radiative limit is 1.4 ms. This results in a very low surface recombination value $S_{eff} = 7 \pm 2$ cm s^{-1} demonstrating the good level of passivation achieved by silicon carbide. The superior and more conservative limit for the surface recombination velocity is calculated by assuming infinite bulk lifetime, thus $S_{eff} = W/2\tau = 24$ cm s^{-1}. Fig 3.4 shows other examples of experimental lifetime curves for the pressure series, with the corresponding simulated curves. It can be seen that in some cases the agreement between experimental and simulated curves is not complete. Apart from experimental sources of errors (miscalibrations, mobility models and so on) that would produce errors in the lifetime values, the causes could be attributed to the simplicity of the model. In order to improve it, some mechanisms can be taken into account [89]:

- An interface state density (or density of states), causing a charge Q_{it} that is variable with the Fermi level. Normally, in silicon nitride films this value is neglected against the high positive fixed charge, Q_f. To include it in the model it would be necessary to know the density of states, D_{it}, and the capture cross sections, σ_n σ_p. This has been possible in good dielectric films like silicon oxide, in which *C*-*V* measurements allow determination of density of states and Deep Level Transient Spectroscopy (DLTS) provides information about the capture cross sections. However, these two techniques are very difficult to apply to conductive films like silicon-rich *a*-SiC$_x$.
- Recombination in the space charge region created by Q_f and Q_{it}, significant at low injection densities. It is usually modelled by a recombination diode with the corresponding saturation current density (J_{rec}).
- Shunt tunnels through the space charge region. The minority carriers can tunnel through the potential barrier and recombine at the interface. It is modelled by a parallel resistance R_p.

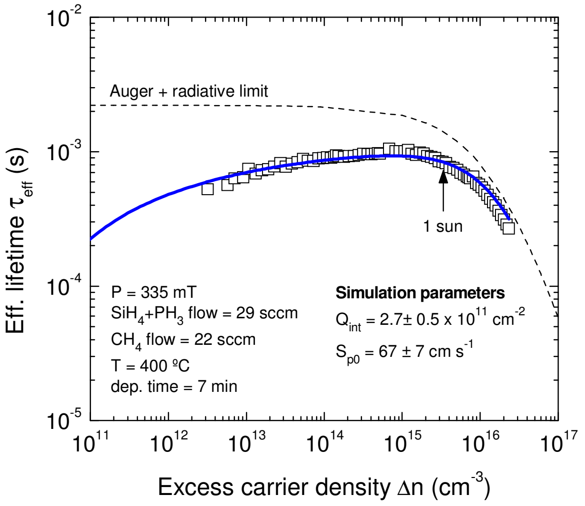

Figure 3.3. Lifetime curve for *p*-type, 0.85 Ω cm, Float Zone wafer, 400 µm thick. Both sides were symmetrically passivated with a 70 nm *a*-SiC$_x$(*n*) film. Arrow marks 1 sun illumination level.

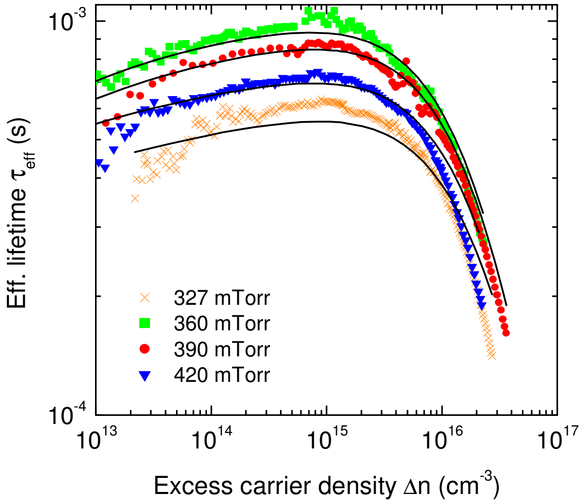

Figure 3.4. Lifetime curves (symbols) with the corresponding simulations (lines) for several passivated *a*-SiC$_x$(*n*):H *p*-type wafers at different pressures in the chamber.

The first of the three points aforementioned is susceptible to be the most determinant in silicon carbide films. Appendix I presents some evidences that relate the field effect passivation to a variable charge.

Fig 3.5 plots the extracted parameters Q and S_{p0}. The fundamental recombination of holes, S_{p0}, correlates directly with the effective surface recombination velocity values, S_{eff}, presented in Fig 3.3. This is an indication that saturation of dangling bonds is crucial

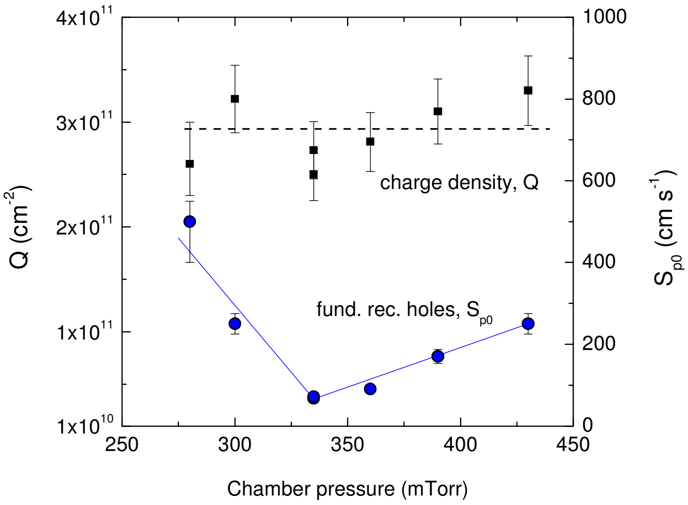

Figure 3.5. Charge density, *Q*, and fundamental recombination of holes, S_{p0}, determined from simulated lifetime curves using the Girisch model. The minimum of the S_{p0} correlates with the minimum found for the experimental S_{eff}, while the charge variation is relatively small.

for the passivation by means of silicon carbide. On the other hand, the error bars for the charge density do not allow establishing a clear trend for this parameter. Probably, the charge density is independent of the pressure with a value at about 3×10^{11} cm^{-2}. This is in agreement with the other dependencies studied in the following sections for the same wafer resistivity. Actually, the charge density seems to be a function of the bulk resistivity, thus increasing values of the doping wafer lead to increasing values of the charge density. This trend can be again explained with a charge originated by the density of states at the interface.

3.4.2 Dependence on the RF power

In photovoltaic technology there is a strong interest in increasing the area of the active device. One of the benefits is to allow a reduction of the perimeter to area ratio, thus minimizing the recombination at the edges of the cell. It also causes a reduction of the production costs per unit module. Currently, most of the solar companies manufacture solar cells on 6” diameter substrates, and the technology has even been applied in 8” wafers. Therefore all processes involved in solar cell technology have to demonstrate uniformity in large areas. In the case of deposited films for surface passivation, the uniformity is achieved by appropriate industrial instrumentation and optimization of deposition parameters.

The features of the reactor employed in this thesis do not allow uniformity in very large areas. However, in order to follow the actual trend research was addressed to achieve more uniform silicon carbide films. By varying the RF power it was possible to achieve films with different degrees of uniformity. In a systematic study to explore such uniformity combined with surface passivation, the RF power was varied from 15 to 90 W. The deposition time was set at 5 minutes and the total pressure at 335 mTorr. The gas flow ratios were maintained unaltered with respect to those used in last section. Identically, the wafers received a FGA at 430 ºC for 30 minutes before checking the lifetime.

3.4.2.1 Thickness uniformity with RF power

Due to the geometry of our PECVD chamber, a circular symmetry in film characteristics was expected. Therefore, analysis of the thickness was performed along the radius of the reactor plate. Fig 3.6 shows the thickness of the layer as a function of the distance from the centre of the plate at different RF powers. In all cases, the thickness has a minimum at the centre and monotonically increases with distance. However, as the RF power increases uniformity is achieved in larger areas. For example, if we want to passivate 4” *c*-Si wafers, we should use a RF power of at least 30 W in order to have a variation in thickness less than 10%. It is possible to reach the same uniformity in 6” substrates if the power is increased up to 60 W. Furthermore, it can be seen that the traditional depositions employed at UPC at 15 W are not suitable for the passivation of large substrates with regard to homogeneity. Of course, it is essential to keep the passivating properties when using these higher RF powers. This is analysed in the following section.

3.4.2.2 Lifetime dependence on RF power

To check whether the passivating properties were unaltered or not, wafer passivation was investigated for the rest of the RF powers. At the date of performing these experiments an improvement of the Sinton WC-100 instrument was performed, adding a cover that allowed the measurements run from true dark conditions to illumination. As a consequence, the DRM effect appeared and it was introduced in the fitting routine for lifetime simulations. As previously explained, this effect allows a better determination of the charge density, Q, without introducing any new parameter. An example is shown in

Fig 3.7 where an increasing tail at low injection level range exceeds the corresponding Auger lifetime, indicating that its nature does not come from any physical recombination mechanism.

In Fig 3.8, the dependence of S_{eff} at 1 sun illumination on the RF power is shown. These values are calculated by introducing the corresponding τ_{eff} value into equation (3.1). As it can be seen, S_{eff} is reduced by almost a factor of 2 when RF power is increased from 15 W to 30 W. Then, a plateau is found up to a RF power of 60 W. Beyond this point, S_{eff} increases up to 54 cm s^{-1} for RF power of 90 W. Best result is a S_{eff} value as low as 24 ± 4 cm s^{-1} for a RF power of 45 W.

The measured τ_{eff} (Δn) curves for different RF power were fitted resulting in the Q and S_{p0} values shown in Fig 3.9. Regarding Q, it remains constant to about 3.2×10^{11} cm^{-2} up to a RF power of 60 W increasing to 4×10^{11} cm^{-2} for 90 W. In all cases, Q has positive high values resulting in inversion conditions at *c*-Si surface under low-injection.

On the other hand, S_{p0} slightly decreases when RF power is increased up to 45 W. Then a plateau is found with S_{p0} values of about 200 cm s^{-1} up to 60 W. Finally, S_{p0} drastically increases beyond 1000 cm s^{-1} for a RF power of 90 W. This result suggests that interface state density could be slightly reduced when RF power is increased up to 60 W and then increases at 90 W. This would indicate that the *a*-SiC$_\text{x}$(*n*):H film could passivate *in-situ* the increment in interface state density due to the ion bombardment onto *c*-Si surface up to a RF power of 60 W. Beyond this point, the energy supplied to the plasma species seems to be too high for a satisfactory *c*-Si surface passivation. These two different power regimes can also be responsible of the increase in Q at a RF power of 90 W since this charge density could be related to a higher defect density within the *a*-SiC$_\text{x}$(*n*):H films.

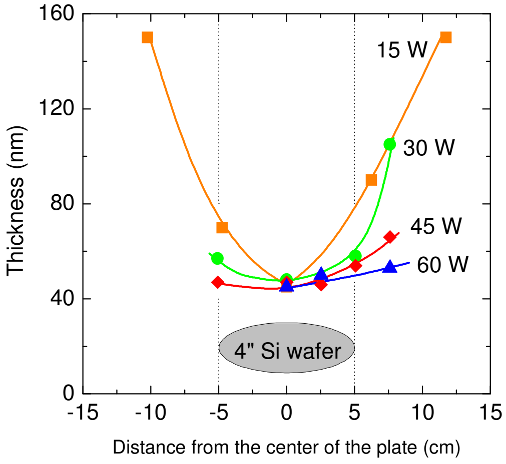

Figure 3.6. Thickness profile for the *a*-SiC$_x$(*n*):H deposited during 5 minutes. For higher RF powers the layers are significantly thinner and more homogeneous.

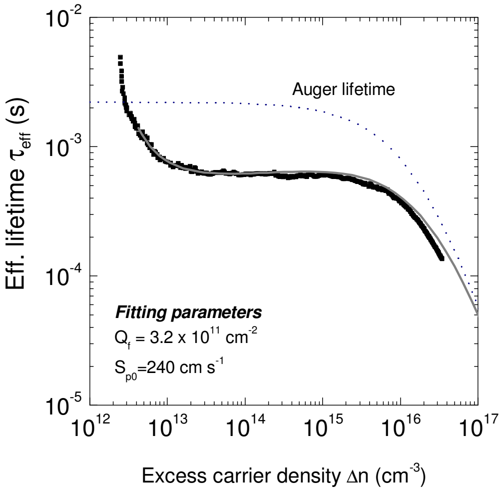

Figure 3.7. Measured τ_{eff} (Δn) curve (symbols) and fitting curve (line). Auger lifetime (broken line) is also plotted. Fitting parameters determined by the fitting routine are also indicated in the graph.

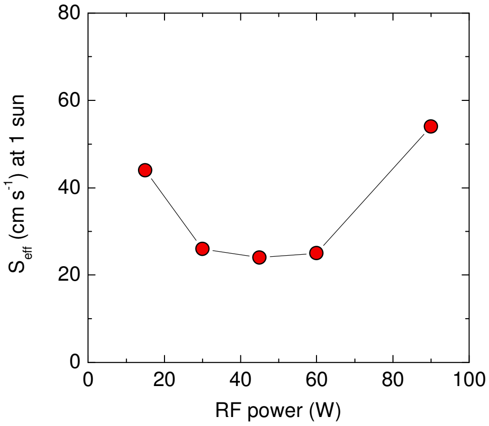

Figure 3.8. Effective surface recombination velocity at 1 sun illumination as a function of RF power. Best result is achieved at 45 W with S_{eff} = 24 ± 4 cm s^{-1}.

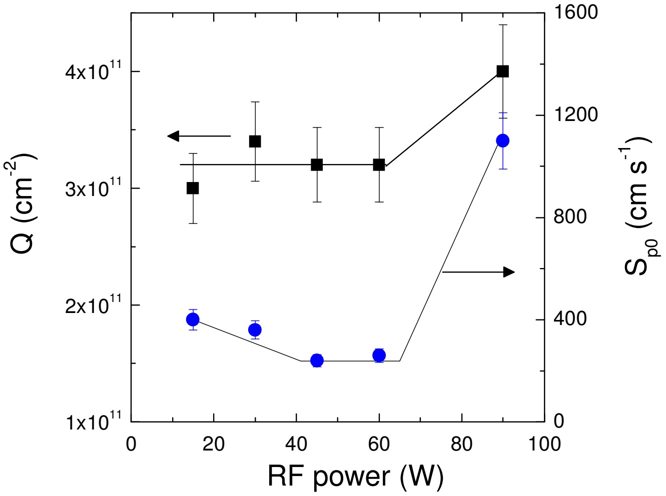

Figure 3.9. Charge density, Q, and fundamental recombination of holes, S_{p0}, determined from simulated lifetime curves using the Girisch model in the RF power series.

3.4.3 Dependence on thickness

The aim of this experiment is to establish any dependence of surface passivation on the silicon carbide thickness. It was inspired in the results obtained by Elmiger and Kunst for amorphous silicon nitride [56]. In that work, the total excess conductance, ΔS, of *p*- and *n*-type substrates passivated with SiN$_x$ films of different thickness was determined by contactless microwave conductivity measurements. This parameter is directly related to the effective lifetime and hence to the surface passivation level. Charge density in the films was derived from ΔS. Their results concluded that both excess conductivity and charge density stored in the SiN$_x$ film increased with the film thickness up to 20 nm and then saturated. The saturation value for the charge density was $Q = 3 \times 10^{12}$ cm^{-2}, in agreement with that obtained through Capacitance-Voltage measurements of MIS structures with thick (100 nm) SiN$_x$ films. The interface states density value was much smaller than the fixed charge value, $D_{it} = 5 \times 10^{11}$ eV^{-1} cm^{-2}, and therefore considered to have low impact in the surface recombination.

Similar to the silicon nitride case, it is interesting to know how the charge is distributed with the film thickness. However, the films deposited in this Chapter are rich in silicon, resulting in conductivity that is too high to prepare well-behaved MIS capacitors. This problem increases even further for thin films (<100 nm). Therefore, instead of using *C-V* measurements, the analysis of the charge density was carried again by simulations of the lifetime curves using the Girisch model.

The experimental process developed in this section is the same as in the two previous sections. The RF power was kept at 30 W to achieve homogeneity in at least 4" wafers, the total pressure at 335 mTorr and the deposition time (labelled as t_{dep}) was varied from 1 to 12 minutes. We measured the thickness in the range of 10 – 100 nm, finding a linear relationship between this parameter and the deposition time. As usually in this Chapter, a FGA at 430 ºC for 30 minutes was applied before lifetime testing.

3.4.3.1 Analysis of charge density and fundamental recombination velocity

Fig 3.10 shows the τ_{eff} values at 1 sun illumination for t_{dep} ranging from 1 to 12 minutes. As it can be observed, τ_{eff} increases with deposition time up to t_{dep}= 5 min, indicating an improvement in surface passivation. The corresponding effective surface recombination velocities are also shown in Fig 3.10. S_{eff} values when t_{dep} is higher than 5 minutes are about 24 – 27 cm s^{-1} suggesting that 40 nm is the minimum film thickness to obtain an optimum surface passivation.

In Fig 3.11, we show the experimental $\tau_{\mathrm{eff}}(\Delta n)$ curves together with the modelled curves for four different thicknesses. From the theoretical curves we determined an almost constant Q value of $3.4 \pm 0.2 \times 10^{11}$ cm^{-2}. Moreover, the dependence of S_{p0} on film thickness also plotted in Fig 3.10 follows the dependence found for τ_{eff}, S_{eff} suggesting that S_{p0} is the parameter responsible for the surface passivation improvement.

The results obtained suggest two possibilities for the origin of the charge density that causes the field effect passivation. The first possibility is that it could be allocated in a layer narrower than 10 nm (this is the minimum thickness used in the experiment). The second possibility is that it depends only on the interface states density, D_{it}, being then attributed to the filled number of states according to the Fermi level position. In other words, it would be dependent only on the wafer resistivity. This last hypothesis is reinforced by the results obtained in next section and in Appendix I, in which we analyze the properties of silicon carbide passivation on wafers with different resistivities. In case this second possibility was true, it would represent an important difference compared to amorphous silicon nitride, with high charge density values in the range of 10^{12} cm^{-2}, regardless the resistivity of the wafer. Although further research is needed to confirm the Q values for a-SiC$_x$:H films through independent measurements, additional experiments on surface passivation of boron-doped emitters has also pointed to the same direction. It is well-known that the high positive Q values of SiN$_x$ have led to poor results of passivation of boron-doped emitters [28]. Experiments reported in Ref [120] and [121] yielded lower S_{eff} values for a-SiC$_x$:H films on boron-doped emitters compared to those obtained with SiN$_x$. On the other hand, the evolution of the S_{p0} values with film thickness indicates a higher surface quality, probably due to the saturation of dangling bonds by atomic and/or molecular hydrogen.

In order to clarify the evolution of interfacial hydrogen, we performed additional film depositions for 1, 2 and 5 minutes (corresponding to thickness of about 10, 20 and 40 nm approximately). Consecutive anneals in forming gas of 10 minutes at 430 ºC were performed measuring the τ_{eff} value at 1 sun illumination after each step. Fig 3.10 shows the evolution of the measured τ_{eff} values as a function of the annealing time. The values are normalized to the value of the as-deposited samples. As a general trend, the effective lifetime and, hence, surface passivation improves for short FGA while there is decay for long anneals. Considering that the main source of hydrogen is the a-SiC$_x$(n):H film, this behavior could be due to a competing mechanism between hydrogen-covering of the interface dangling bonds and dehydrogenation of the film. Actually, identical anneal but in N$_2$ atmosphere has led to similar improvement in surface passivation indicating that the H$_2$ present in the forming gas plays a minor role, if any.

The effect of the increasing FGA time has been analyzed for the 10 nm thick sample (t_{dep}= 1 min). Simulations of the τ_{eff} (Δn) curves indicate a constant density of charge equal to $(3.7 \pm 0.1) \times 10^{11}$ cm^{-2} and S_{p0} values increasing from 2550, to 4250 cm s^{-1} for annealing times ranging from 0 to 30 minutes, confirming the hypothesis of dehydrogenation. The interface quality and hence the S_{p0} are strongly affected at the same time by the film thickness and the annealing time. Furthermore, it is clear from the results in Fig 3.11 that thicker films are more robust and have better properties under FGA treatment.

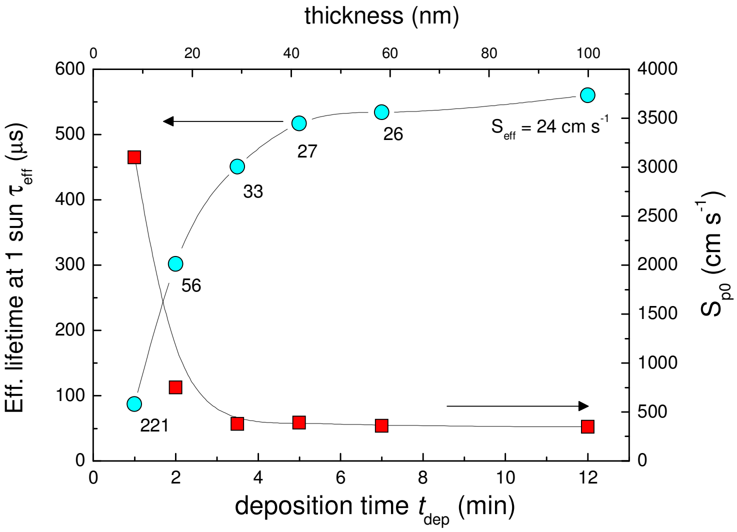

Figure 3.10. Experimental (circles) τ_{eff} and S_{eff} values at 1 sun illumination vs. deposition time, t_{dep}. Also shown are S_{p0} values determined from the simulations (squares). Corresponding film thickness is represented on the upper axis. Solid lines are a guide for the eye.

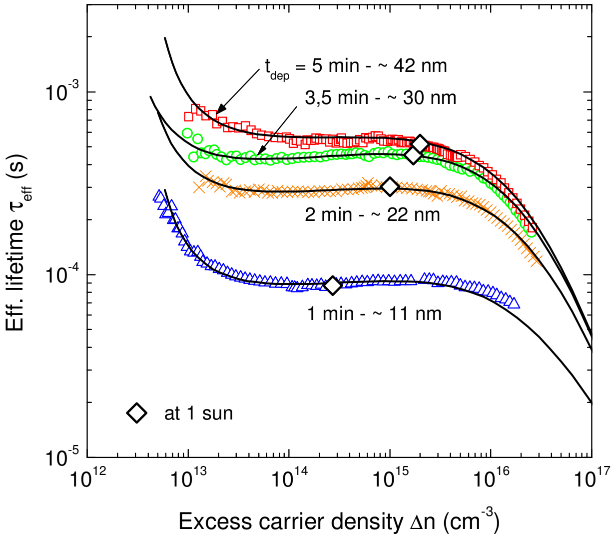

Figure 3.11. Experimental (symbols) and simulated (lines) τ_{eff} vs Δn curves for *p*-type 0.85 Ω cm wafers passivated with single *a*-SiC$_x$(*n*):H films with different film thicknesses. The corresponding deposition time and film thickness are labeled. The DRM effect is observed at low Δn values. Rhombuses indicate 1 sun illumination.

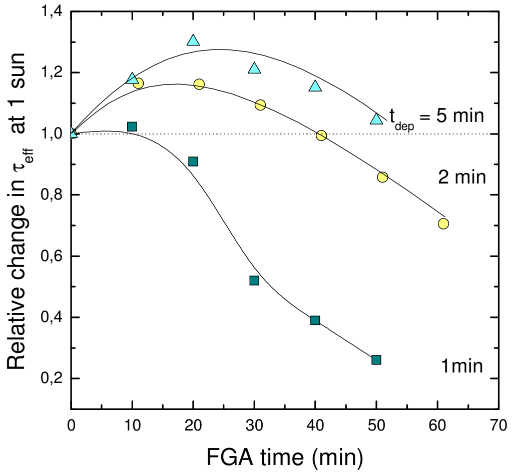

Figure 3.12. Normalized τ_{eff} values at 1 sun illumination as a function of FGA time for *p*-type 0.85 Ω cm samples passivated with three different deposition times labelled in the graph. Solid lines are a guide for the eye.

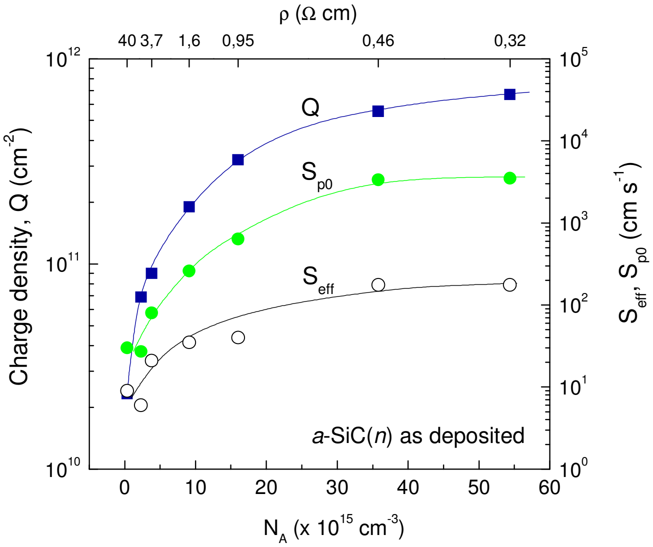

Figure 3.13. Experimental values of surface recombination velocity and simulation parameters, *Q* and S_{p0}, as a function of the wafer doping.

3.5 Surface passivation dependence on wafer resistivity

In order to analyze the dependence on bulk doping, optimized silicon carbide films were used to passivate wafers with different resistivities ranging from 0.3 to 40 Ω cm (N_A from 5.4×10^{16} to 3.4×10^{14} cm^{-3}). The wafers were chemically etched using a 1:3:3 HF:HNO$_3$:CH$_3$COOH$_3$ solution (the so-called CP133 solution) to provide similar surface conditions in all samples. A RCA sequence ended with an HF dip was applied before PECVD depositions. As usual, lifetime measurements were performed and fitted with the Girisch model.

Fig 3.13 plots the measured values for the surface recombination velocity, S_{eff}, at $\Delta n = 10^{15}$ cm^{-3} and the two simulation parameters, the charge density, Q, and the fundamental recombination of holes, S_{p0}. It can be seen that surface passivation gets worse as the doping increases, indicated by increasing values of S_{eff}. Increasing values of S_{p0} and Q are also found with doping. Therefore, as the doping increases the number saturated dangling bonds (related to S_{p0}) is lower, while the field effect (related to Q) is enhanced. The experimental S_{eff} values evidence that the first mechanism dominates the second. The increasing values of S_{eff} as the substrate doping increases are easily explained by a higher density of states provided by the boron impurities. However, the strong dependence of the charge density on the doping is relatively anomalous and indicates again that the origin of the field effect passivation is not provided by a fixed charge density, but probably by a variable interface density of states that depends on the Fermi level position of the crystalline silicon. Appendix I provides preliminary results about the fundamental properties of the charge density in *a*-SiC$_x$ films based on corona charge measurements. However, a complete theory of the phenomenon requires further investigations.

3.6 Chapter conclusions

This Chapter has focused on the surface passivation of *p*-type crystalline silicon by means of phosphorus-doped silicon-rich amorphous silicon carbide films *a*-SiC$_x$(*n*):H grown by PECVD. With the aim to find uniform films with good surface passivation, different deposition conditions have been explored for low resistivity wafers (0.85 Ω cm): total pressure in the chamber, RF power and film thickness. Values of S_{eff} as low as 7 ± 2 cm s^{-1} have been achieved with films grown under very low RF power, although the thickness profile was not completely uniform. Higher values of S_{eff} = 24 ± 4 cm s^{-1} have been encountered for uniform films, still providing excellent surface passivation.

Determination of the charge density allocated in the layer through lifetime simulations reveals interesting results. For the series in which the chamber pressure is varied, the charge density seems to be relatively independent of the deposition conditions, at about 3.4×10^{11} cm^{-2}. More accurate simulations, including the Depletion Region Modulation (DRM) effect also show a charge value that can be assumed as constant for the resistivity used. In the series with the film thickness variation the charge density showed, surprisingly, a constant value of $Q = 3.4 \times 10^{11}$ cm^{-2}, which is very similar to that obtained in most cases of the RF power (3.2×10^{11} cm^{-2}). On the other hand, a strong dependence of the charge on the wafer resistivity experiments has been found. This may indicate that the origin of the fixed charge is not attributed to a fixed charge density in the film, but depends on the whole *a*-SiC$_x$/*c*-Si system.

The fundamental recombination of holes, S_{p0}, varies with the deposition conditions, indicating that besides the field effect passivation the improvement for the surface passivation is due to the saturation of dangling bonds, partly provided by the atomic or molecular hydrogen present in the films.

Finally, it must be mentioned that due to the high content of silicon these films present high absorption of light. Optical transmission data show that for films around 80 nm thick only 50% of visible light (400 – 1000 nm) goes through a film/glass system. In an *a*-SiC/*c*-Si interface the transmission to the *c*-Si might be higher due to some interference phenomena. Nevertheless, the portion of light absorbed in the amorphous film is not susceptible of contributing to the photocurrent because the photogenerated carriers might recombine rapidly, before any chance to reach the *p-n* junction. Therefore, the applications of these films should be relegated to the passivation of the rear side of a solar cell unless their absorption is minimized, for example by reducing the thickness. In this sense, next Chapter is focused on the development of films for front side passivation.

CHAPTER 4

Stacks of Si rich/ C rich films: passivation with antireflective properties

4.1 Introduction

The previous Chapter demonstrated that it is possible to achieve good surface passivation of *p*-type wafers by means of amorphous silicon carbide films. It has already been established that the optimum composition to achieve low values of surface recombination velocity implied the use of silicon rich films, with a relatively low bandgap (around 1.8 eV), thus presenting significant light absorption in the visible range. Widening the bandgap by introducing more carbon in the films has resulted in much poorer passivation. Therefore, the use of these layers in solar cells should be restricted to passivate the rear side.

In addition, as the previous Chapter showed, increasing the film thickness decreases strongly the surface recombination velocity by reducing the fundamental recombination velocity of holes (S_{p0}), while the amount of charge created in the SiC_x film, which builds the so-called field effect passivation [42], seems to be independent of this thickness. This can be explained in terms of higher hydrogen incorporation at the SiC_x/Si interface correlated with longer deposition time, and suggests the possibility of depositing by PECVD stacks of two SiC_x layers with different compositions. The first layer would consist of a very thin silicon rich film, thus keeping the absorption to a minimum, providing charge density and also a certain reduction of the density of states. The second layer would be a carbon rich, hydrogenated coating with good antireflective properties, i.e. an appropriate refractive index ($n \approx 2$) and thickness (about 70 – 80 nm), which would contribute to additional passivation by hydrogen.

The principal application of the stacked films is the passivation of the front side of solar cells, in which the emitter is normally located. Therefore, the stacks have to prove that good surface passivation can be achieved in heavily doped regions. In recent works we reported the passivation of phosphorus emitters, which is reviewed in the present Chapter, and boron emitters [120,121], which was achieved with the collaboration of the University of Konstanz. Apart from the use at the front side, the stacks provide an important benefit when applied for the passivation of the rear side in PERC solar cells, as we explain in section 4.4.3.

This Chapter explores the passivating properties of SiC(n)/SiC(i) stacks to be applied to p-type bases (0.95 Ω cm) and n^+-type emitters (20 to 500 Ω/sq) with different thicknesses of the SiC(n) layer. For the p-type bases, the values of effective recombination velocity are determined in all configurations, while for the n^+-type emitters the most relevant parameter calculated is the minority saturation current density J_{0e}. An analysis of the optical properties provided by ellipsometry measurements is presented and will be used to determine optical losses. Finally, solar cell efficiency limits for 50 Ω/sq and 90 Ω/sq emitters are theoretically determined.

4.2 Deposition conditions

From the antireflection point of view, the optimum refractive index for the passivating films in the visible range should be $n \approx 2$ for non encapsulated solar cells and $n \approx 2.3$ for glass encapsulated cells [122], without optical absorption and with a thickness of around 70 nm. The optical and structural properties of amorphous semiconductors are highly dependent on sample preparation, especially for those involving the presence of hydrogen. For pure hydrogenated amorphous silicon, *a*-Si:H, many different values of the refractive index and optical bandgap have been reported, ranging between $n = 3.5 - 4.5$ and $E_g = 1.4 - 1.8$ eV [123-126]. For pure hydrogenated amorphous carbon, *a*-C:H, it is possible to reach bandgap values of 3.8 eV with a refractive index equal to 1.5 [127], but also values up to 4.1 eV have been reported [128].

Although carbon rich films are not suitable to achieve very low values of S_{eff}, the content of hydrogen in the film can be crucial to provide an extra surface passivation after a FGA treatment. Hydrogen can diffuse towards the *a*-SiC/*c*-Si interface, thus reducing the Density Of States (DOS) by saturating those dangling bonds still remaining after the PECVD deposition. Apparently, a minimum initial hydrogen concentration in the films is required to improve surface passivation with the FGA. Such concentration depends strongly on the deposition temperature, as shown in Fig 4.1. It corresponds to investigations previous to this work, made in our group by M. Vetter *et al.* [129]. Measurements of Fourier Transform Infra Red (FTIR) spectroscopy were performed on intrinsic silicon rich films grown at different temperatures, calculating the integrated absorption at 2000 – 2100 cm^{-1} peak. This absorption is directly related to the hydrogen concentration, and hence the graph shows that it decreases with the temperature. Therefore, low temperatures are preferred to obtain carbon rich films. On the other hand, for phosphorus-doped silicon-rich films, surface passivation is optimum when the deposition temperature is above 350 ºC [32]. Due to technological reasons, it is desirable that both films are deposited at the same temperature or at least as close as possible. The optimum option found has been to grow the silicon rich films at 350 ºC and the carbon rich films at 300 ºC.

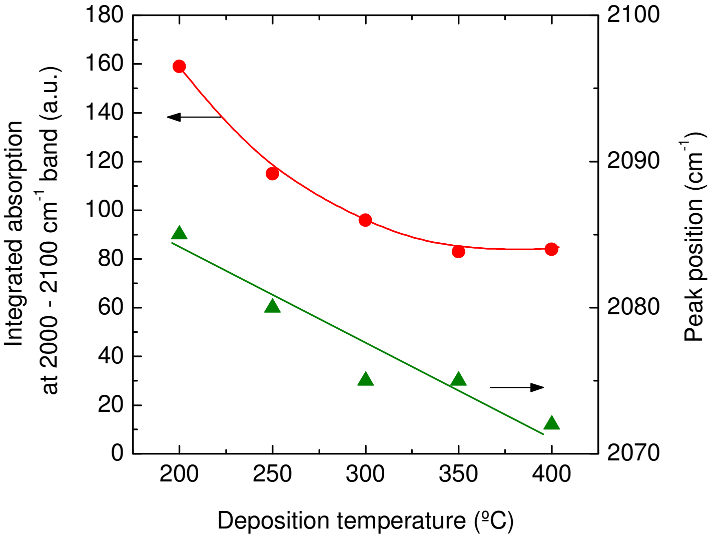

Figure 4.1. FTIR measurements for intrinsic films. The hydrogen concentration, directly related to the integrated absorption of Si-H bonds, decreases with the deposition temperature. Extracted from reference [129].

Regarding all the aforementioned points, the present experiment chose a deposition temperature of 350 ºC for the silicon-rich passivating films and 300 ºC for the carbon-rich antireflective films. Thus, optimum deposition conditions were kept for the two layers. Once the deposition conditions are defined, it is useful to establish a nomenclature for the two films. From now on the phosphorus-doped silicon-rich sample will be labelled as PAS, to indicate its passivating behaviour. The intrinsic carbon rich will be designated as ARC due to its antireflective properties.

Technologically, the process is achieved in the following way. After RCA cleaning, the wafer is placed inside the PECVD reactor with the plate at 350 ºC. Once the vacuum is achieved the phosphorus-doped silicon-rich (PAS) film is deposited. Then, the plate temperature is set at 300 ºC without breaking the vacuum in the chamber. After 12 minutes the new set temperature is achieved and the deposition of the intrinsic carbon-rich film (ARC) follows.

The importance of the PAS film thickness has been discussed in Chapter 3. It was stated that at least 40 – 50 nm are required for best surface passivation (corresponding to 5 – 6 minutes in deposition time). In the present Chapter the effect of thickness on the passivation properties is also analyzed, but using thinner films in order to keep optical losses to a minimum. In detail, four different deposition times were chosen: 0 (i.e. no layer), 30, 60 and 90 seconds. They correspond nominally to 0, 4, 8 and 12 nm thick

Table 4.1. Deposition parameters of the two films that form the stack.

		PAS (Si rich)	ARC (C rich)
RF power	(W cm^{-2})	0.043	0.086
Temperature	(ºC)	350	300
pressure	(mTorr)	335	315
SiH_4+PH_3	(sccm)	29.5	-
SiH_4	(sccm)	-	2.8
CH_4	(sccm)	24.3	32
deposition time	(min)	0.5 – 1.5	11

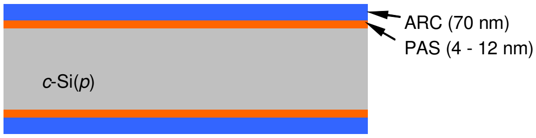

Figure 4.2. Schematic of the passivation structures by stacks of silicon carbide. PAS layer is Si rich with good passivation properties. ARC layer is C rich with good antireflective properties.

layers as determined from ellipsometry measurements (see next section). The deposition time for the ARC film was 11 minutes, which corresponds nominally to 70 nm. As usual, symmetrical depositions were performed on both sides of the wafers for lifetime analysis. The PECVD conditions are detailed in Table 4.1. Figure 4.2 shows a schematic of the lifetime test samples.

4.3 Optical constants measured by ellipsometry

The determination of refractive index, *n*, and extinction coefficient, *k*, in a wide spectral range is very useful information when considering effective absorption of light into the silicon solar cell. To this end, depositions of single PAS film (1 and 5 minutes) and single ARC films (11 minutes) were performed and analyzed with a phase-modulated ellipsometer (UVISEL, Jobin Yvon Horiba) in a wavelength range from 200 to 1200 nm. The measurements were taken on as-deposited samples but also on samples annealed in forming gas (FGA) at 400 ºC for 20 minutes. The pseudo-dielectric functions of the PAS and ARC layers were modelled using the Tauc-Lorentz dispersion law [130,131] to extract the optical constants. Both refractive index and extinction coefficient are presented in Figure 4.3 for as-deposited and FGA cases.

Table 4.2. Thickness and optical bandgap extracted from ellipsometric measurements of the different silicon carbide films to form the stack.

Deposited film	Thickness (nm)	Optical gap (eV)
PAS, 5 minutes, as deposited	43	1.83 ± 0.01
PAS, 5 minutes, FGA 20 minutes	41	1.75 ± 0.01
ARC, 11 minutes, as deposited	72	2.53 ± 0.02
ARC, 11 minute, FGA 20 minutes	67	2.53 ± 0.03

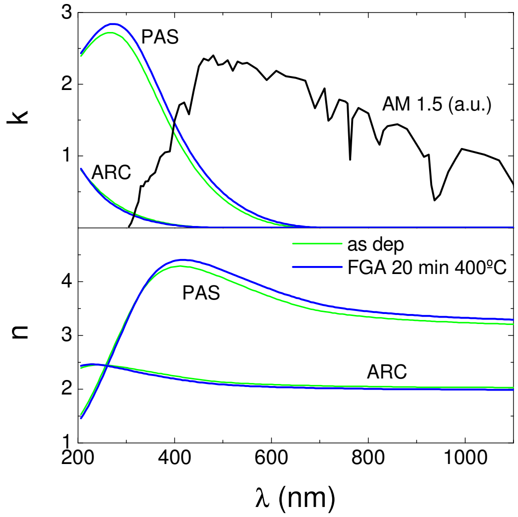

Figure 4.3. Refractive index, *n*, and extinction coefficient, *k*, measured for the PAS and ARC films before and after a FGA treatment at 400 ºC for 20 min. For comparison, the AM 1.5 spectrum is also plotted.

The PAS layer is responsible for the optical absorption. Its deposition rate has been determined to be 8.0 ± 0.8 nm min^{-1}. The FGA treatment at 400 ºC for 20 minutes affects slightly both the refractive index *n* (from 3.75 to 3.62 at 630 nm) and the extinction coefficient *k*, while the optical gap slightly reduces from 1.83 to 1.75 eV. On the other hand, the thickness of the antireflective coating is 67 ± 3 nm, and the optical constants are not affected by the FGA. Essentially, the ARC layer maintains good antireflective properties in a wide range of wavelengths ($n = 2.0$, $k = 0$ for $\lambda > 450$ nm) and an optical bandgap equal to 2.53 eV. Table 4.2 summarizes the thickness and the optical bandgap for the four cases. As a last comment, the parameters obtained for the PAS film deposited for 1 minute were in agreement with those for the 5 minute deposited films.

4.4 Surface passivation of *p*-type, 0.95 Ω cm wafers by means of silicon carbide stacks

This section starts analyzing the experimental results concerning the surface passivation as a function of the PAS thickness film, and then their evolution with FGA annealing time at 400 ºC. Symmetrical depositions were performed on both sides of <100> oriented, Float Zone, *p*-type, 0.95 Ω cm, 300 µm thick, double-side polished *c*-Si wafers. The lifetime curves as a function of the excess carrier density were fitted using the Girisch model, with a brief discussion about the determination of the charge density and the fundamental surface recombination of holes, S_{p0}.

4.4.1 Surface recombination velocity and evolution with FGA

Figure 4.4 plots the values of surface recombination velocity as a function of the FGA time for four different stacks configuration with different PAS layer thickness. We first focus on the as-deposited case, without any FGA treatment. For the case without PAS film the values of S_{eff} obtained are too high for high efficiency solar cells. When the PAS film is introduced, a reduction of S_{eff} is found, becoming more important as the film thickness is increased. Not only this trend is in agreement with the results obtained in Chapter 3 for single SiC(*n*) films, but also the lifetime values obtained for the same thicknesses (deposition time 1 minute) are comparable. On the other hand, the evolution with the FGA treatment is completely different. In Chapter 3 the lifetime evolution with the FGA depended on the film thickness (see section 3.4.3.1 and Fig 3.12), obtaining improvement of surface passivation for thicker films and degradation for thinnest ones. With the stacks, the surface passivation improves regardless the PAS film thickness, and the improvement is much more important. To clarify these results we deposited single PAS films on the same type of wafers and performed the same study with FGA time. Fig 4.5 shows the S_{eff} values for two of the stacks plotted in Fig 4.4, together with the S_{eff} values for single SiC(*n*) films with the same thickness. It can be seen that the trends of S_{eff} for singles and for stack films are in opposite direction.

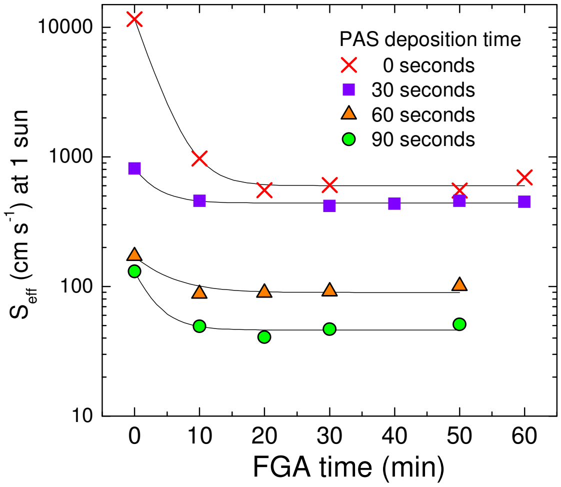

Figure 4.4. Effective surface recombination velocity (S_{eff}) of *p*-type 0.95 Ω cm planar wafers passivated by stacks of silicon carbide films (PAS and ARC) and subjected to FGA at 400ºC and at different times and different thicknesses of the PAS layer. Lines are guides to the eye.

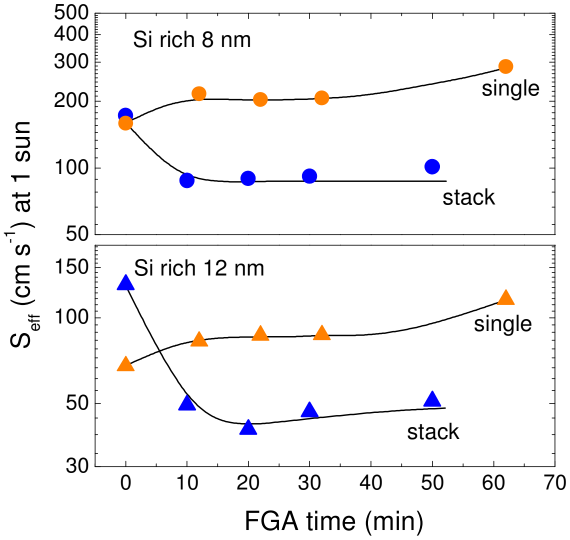

Figure 4.5. Evolution of S_{eff} with FGA time for single layers and for stacks. At equal thickness of the passivation layer, the stacks provide better surface passivation after annealing. Lines are a guide to the eye.

From the results explained above, two conclusions can be reached related to the role of hydrogen in surface passivation. First, it was previously shown in section 4.2 that the content of hydrogen in the ARC layer is substantially higher than in the PAS layer due to a lower deposition temperature. This extra amount of hydrogen might provide a better hydrogenation of the *a*-SiC(*n*)/*c*-Si interface, thus explaining the higher improvement in surface passivation within the firsts 20 minutes of FGA treatment when the stack is used.

Second, the opposite trend with the FGA for single PAS films and for stacks suggests that ARC film may act as a hydrogen barrier. This film would avoid the hydrogen effusion to the exterior, thus keeping its concentration constant within the film and therefore at the *a*-SiC(*n*)/*c*-Si interface.

The lowest surface recombination velocity values found for the stacks with PAS films deposited during 60 and 90 seconds are S_{eff} = 90 and 40 cm s^{-1}. The corresponding implied voltages at 1 sun (i.e. the upper limit calculated from the carrier density, Δn, at that illumination) are 671 and 688 mV, respectively. Despite these values are acceptable for the fabrication of high efficiency solar cells, if the stacks are to be applied at the rear side it would be more convenient to use a thicker PAS film, deposited at least during 5 minutes. Values up to 709 mV have been demonstrated for those silicon rich films in the previous Chapter.

4.4.2 Lifetime curves, fittings and determination of charge density

Fig 4.6 shows the lifetime curves measured using the QSS-PC technique for the 20 minutes annealed samples. The solid lines represent the fittings using the Girisch model [86] incorporating the DRM effect. The model uses expression (1.66) to calculate S_{eff} from lifetime measured values. For low lifetime values this expression does not hold because the carrier excess density is not entirely uniform through the wafer thickness, so that the extraction of parameters can be affected by errors. This is particularly true for the two lowest lifetime curves in Fig 4.6. Fortunately, the DRM effect is very sensitive to the charge density and helps to correct this problem.

From simulations we extracted a constant value of the charge density $Q = 3.3 \times 10^{11}$ cm^{-2} and decreasing values of the fundamental recombination of holes, S_{p0}, from about 7000 to 500 cm s^{-1} as the film thickness increased (see Fig 4.7). The same value for the charge density is found in all the points from the FGA series shown in Fig 4.4. Apparently, the charge density is invariant regardless the *a*-SiC_x(*n*) thickness, the FGA treatment and even the composition. Furthermore, this value is very similar to those obtained in Chapter 3 for SiC_x(*n*) films on wafers that have similar resistivity (0.85 Ω cm). In the different experiments explained in that Chapter the charge density varied between 2.5 and 4×10^{11} cm^{-2}. All these results could be attributed to a constant value of

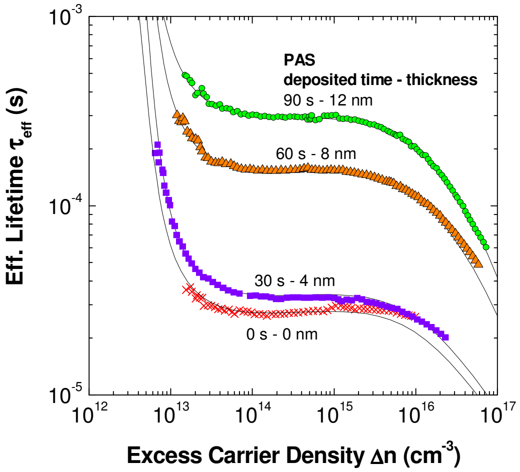

Figure 4.6. Experimental (symbols) and simulated (lines) lifetime curves of the *p-t*ype 0.95 Ω cm planar wafers passivated by stacks and with an optimized FGA treatment.

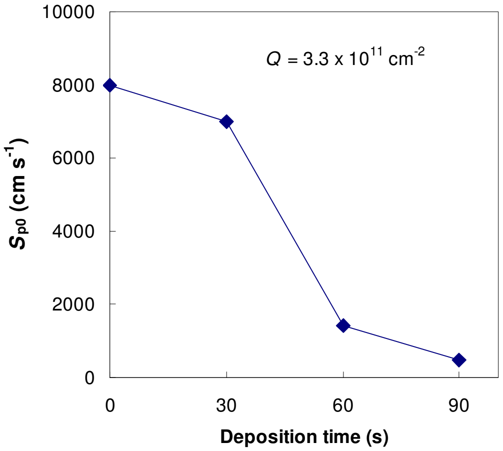

Figure 4.7. Extracted parameters corresponding to lifetime fittings performed in Figure 4.6. A constant fixed charge about Q = 3.3 × 10^{11} cm^{-2} and a decrease of S_{p0}.

the charge density with some scattering. Indeed, some mechanisms that could lead to misinterpretations of the value of the charge have already been identified in the previous Chapter (section 3.4.1).

An important issue arises at this point, since apparently the PAS layer is not critical to build the field effect passivation, but to minimize the density of states at the interface. This provides another argument favouring the hypothesis that the origin of the charge is induced by the *a*-SiC/*c*-Si system rather than being a fixed charge in the film, as it is clear, for example, at the SiO_2/*c*-Si [89] or the *a*-SiN/*c*-Si systems [99].

4.4.3 Applications of stacks to the rear side of the solar cells

A drawback for films with high positive charge when applied to MIS structures (for example the rear side of a PERC solar cell) is that the field effect passivation may vanish due to shunting effects. Lateral shunting appears when perforating the dielectric film to apply the metal contacts [132]. This shunting can be partially prevented if a SiO_2 barrier is located between the contact and the nitride, because the lower charge of the oxide creates a much weaker inversion layer. Another alternative is using films which passivation strategy is based more in the reduction of the interface states density than the field effect passivation, like silicon carbide.

However, the performance of the final device depends not only on the dielectric film, but also on the metallic contacts. Recently, our group has investigated the influence of the metal work function on the open circuit voltage of the solar cell [133] for three different metals: Al (4.25 eV), Cu (4.65 eV), and Au (5.1 eV). The application of the stacks resulted in higher V_{oc} values in Al and Au (642 and 658 mV, respectively) compared to single Si rich films (619 and 628 mV).

Another benefit of using stacks instead of a single Si rich layer concerns the light reflection. The carbon rich layer, with a lower refractive index, helps to enhance light reflection towards the bulk silicon, thus enhancing the cell performance.

The three features aforementioned (better prevention of shunting, good behaviour with metal work function, and higher rear side reflection) accomplished by silicon carbide stacks were used to manufacture PERC solar cells with efficiencies above 20% in collaboration with the Fraunhofer Institute for Solar Energy Systems [134].

4.5 Surface passivation of phosphorus emitters

Conventional screen-printed solar cells use phosphorus doped n^+-emitters with low resistivity (between 40 and 60 Ω/sq). The recombination within those thick emitters dominates over the recombination at the surface. When only thermal oxidation was known, the passivation of that side did not represent a significant improvement in efficiency in front of manufacture expenses for industrial solar cells. Therefore, the surface was usually covered with an antireflective TiO_2 or with Ta_2O_5 coating that only provided enhancement of light absorption.

The front side surface passivation became interesting with the firsts solar cells passivated by silicon nitride, thus providing passivation and good antireflective properties. Not only it keeps low manufacture costs, but also maintains compatibility with the new solar-grade silicon, as multi-crystalline (*mc*-Si) or ribbon silicon (*rb*-Si). The minority carrier bulk lifetime of such low quality substrates may suffer from degradation when exposed to high temperatures (>1000 ºC), as it was reported for thermally grown SiO_2 on *mc*-Si [135]. Wet thermal oxidation at lower temperatures (800 ºC) avoids the problem of bulk lifetime degradation [136,137], but it still implies expensive manufacture steps. As a consequence, lower temperatures are preferred.

Silicon nitride, deposited at 400 ºC has become the alternative to produce high efficiency solar cells at reasonably low costs. Its advantages for the passivation of *p*-type surfaces have already been discussed in Chapter 2. Now, their applications for the passivation of phosphorus emitters are commented. The best passivation scheme for silicon nitride has been obtained by using a stack of SiO_2/SiN_x, including a Rapid Thermal Oxidation (RTO) process [100] at 1050 ºC. Other outstanding results have been presented where silicon nitride is deposited after thermal oxidation [138] or after a drive-in step [139,140], removing first the oxide. In both cases the thermal step modifies the phosphorus profile within the emitter, reducing the surface doping and moving the junction further away from the surface, therefore enabling a more efficient surface passivation. On the other hand, the same approach suggested in this Chapter for silicon carbide, i.e., the use of stack films, has already been successful for silicon nitride [141].

In this section we explore the capabilities of silicon carbide stacks for the passivation of planar n^+-type emitters to be applied at the front side of the solar cell. One of the main objectives is to demonstrate excellent emitter surface passivation without requiring either a drive-in or any other high temperature step than phosphorus pre-diffusion. Results are compared with state-of-the art silicon nitride passivation. The thickness of the PAS layer is optimized, reaching a trade-off between the better passivation achieved for thicker layers and the increased light absorption within the layer, which reduced the photocurrent.

4.5.1 Emitter diffusion with Planar Diffusion Sources (PDS)

The solid Planar Diffusion Sources (PDS)® [142] are an alternative to the conventional liquid diffusion using $POCl_3$. These sources contain the active component CeP_5O_{14}, which is decomposed at temperatures above 800 ºC, releasing P_2O_5 vapour, as shown in Fig 4.8. The vapour is deposited on top of the wafers creating the phosphorus glass, which is the final doping source. This diffusion technique allows a high throughput, needing minimum process requirements. These are a three-zone diffusion furnace with an open quartz tube and a N_2 gas line. N_2 gas is not used as diffusion carrier, but serves to avoid back flow of contaminants into the diffusion tube.

After a RCA and HF cleaning, the wafers were inserted into a tube furnace and phosphorus emitters were pre-diffused simultaneously on both sides for 30 minutes using PDS. The deposition process is essentially the same as in Ref. [143], and the emitter profiles obtained are identical. The temperatures employed ranged from 920 to 800 ºC, obtaining sheet resistances R_{sh} between 20 and 500 Ω/sq. On the one hand, R_{sh} was measured using a four probe tester after etching the phosphorus glass in HF (5%). On the other hand, the diffusion process performed in the clean room is simulated by SUPREM software, which calculates the emitter profile once the input parameters are set. The fixed parameters are the up and down ramps, the diffusion temperature and the diffusion time, altogether conforming the temperature profile as a function of time. The variable parameter is the doping concentration at the phosphorus glass, N_s', which is set to a value near to the solubility limit for phosphorus in silicon at the processed temperature. Doing this SUPREM calculates the actual phosphorus concentration at the silicon surface, N_s, and a value for the emitter sheet resistance. Then, N_s is varied until both sheet resistances, measured and calculated, match. The surface doping concentrations N_s were found to lie in a narrow range between 0.9 and 2.7×10^{20} cm^{-3}, which are consistent with the technological process due to the absence of a drive-in step.

The phosphorus profile for the 50 Ω/sq emitter was measured by Secondary Ion Mass Spectroscopy (SIMS) technique and compared with that calculated by SUPREM (see Fig 4.9). In the absence of a drive-in step, the phosphorus is located very near the surface and

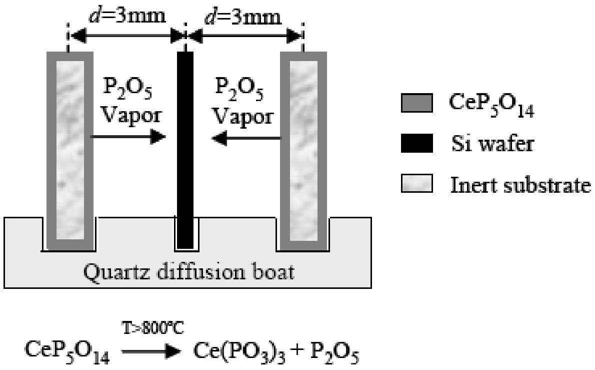

Figure 4.8. Diffusion concept using solid dopant sources. Extracted from [143].

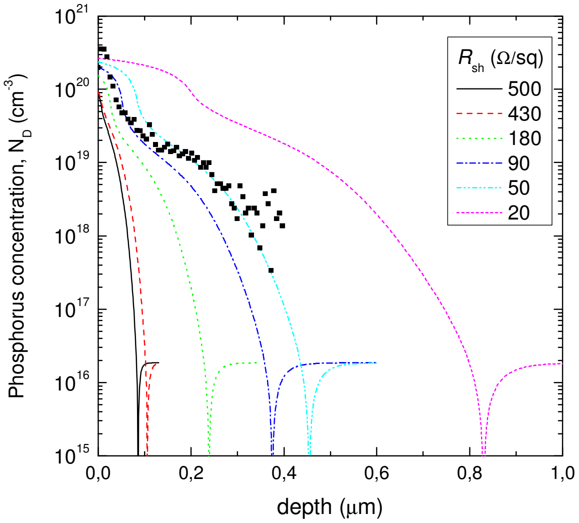

Figure 4.9. Emitter profiles simulated by SUPREM (lines), and the corresponding SIMS measurement (symbol) for R_{sheet} = 50Ω/sq.

the profile determination by SIMS is difficult. However, the agreement between experimental and simulated data is reasonable.

After another RCA cleaning step, ended with a HF dip to remove any grown oxide, the SiC stacks (PAS and ARC layers) were deposited symmetrically on both sides of the wafers. The wafers were then subjected to post-deposition Forming Gas Anneals (FGA) at 400 ºC for 20 minutes, which is the optimized process for bare wafers in the previous section. The temperatures used for both PECVD deposition and FGA are low enough to keep the phosphorus distribution unaltered. Lifetime measurements were performed before the FGA, and over the following five month period to check stability.

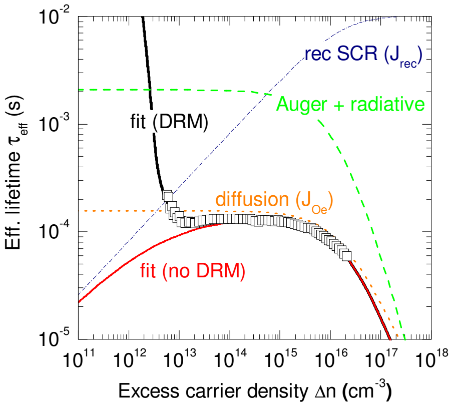

Figure 4.10. Example of extraction of J_{0e} from $\tau_{eff}(\Delta n)$ data (symbols) for a n^+-p-n^+ symmetric structure with 90 Ω/sq emitters and simulation showing all the recombination mechanisms involved (lines). The model for the fitting includes the diffusion diode (J_{Oe} = 72 fA cm^{-2}), the recombination diode (n_{rec} = 2, J_{rec} = 2 × 10^{-9} cm^{-2}), Auger lifetime, and DRM effect.

4.5.2 Lifetime measurements and modelling

The emitter saturation current density, J_{0e}, can be determined from the dependence of the effective minority carrier lifetime, τ_{eff}, on the injection level, Δn. For low resistivity wafers with significant bulk recombination, it is important to use a complete model that includes all the involved recombination mechanisms, in order to get an accurate estimation of J_{0e}.

We measured the effective lifetime (τ_{eff}) in a wide injection level range ($10^{12} < \Delta n < 10^{17}$ cm^{-3}). Afterwards, the $\tau_{eff}(\Delta n)$ curves of the symmetric structure were fitted using a model that incorporates the following recombination mechanisms:

1. A diffusion diode defined by J_{0e} with ideality factor $n_{dif} = 1$
2. A recombination diode that accounts for the recombination in the Space Charge Region (SCR), defined by J_{rec} and ideality factor $n_{rec} = 2$
3. The intrinsic Auger plus radiative bulk recombination [27] (eq. 1.17)
4. The Depletion Region Modulation (DRM) effect [79]. In this section, DRM was modelled analytically using the abrupt junction approximation with constant doping densities in the SCR.

Since the substrates are Float Zone wafers of high quality, the model does not include the Shockley-Read-Hall (SRH) recombination in the bulk. Finally, it is important to mention that the extraction of parameters was performed considering a temperature T = 25 ºC, corresponding to an intrinsic concentration $n_i = 8.65 \times 10^9$ cm^{-3}. Figure 4.10 shows an

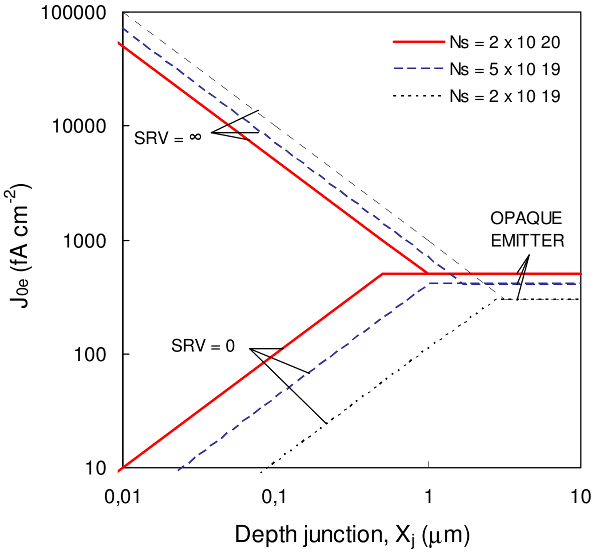

Figure 4.11. The asymptotes of the base current in bipolar devices for Gaussian emitters at given N_s. Extracted from reference [144]

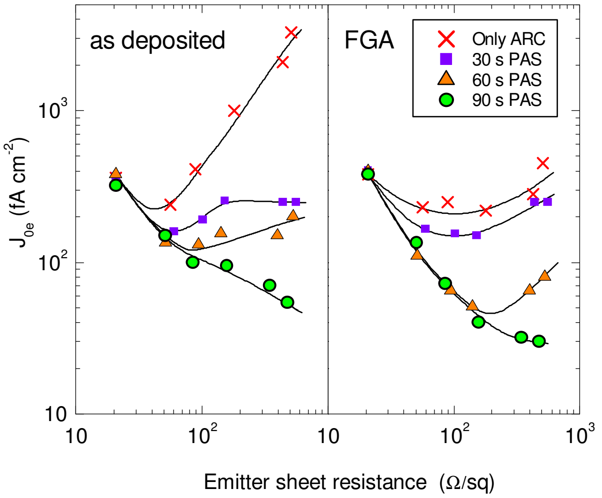

Figure 4.12. J_{0e} values of phosphorus-diffused, planar emitters passivated by PECVD SiC$_x$ stacks, before and after the FGA treatment. The increasing deposition time of the Si rich layer leads to better values of J_{0e}, while the relative improvement after FGA (400 ºC 20 min) is more noticeable for thinner layers. Lines are a guide to the eye.

example of lifetime measurement and simulation corresponding to a 90 Ω/sq emitter passivated with a SiC$_x$ stack (90 s of PAS layer with FGA for 20 minutes), with good agreement between measured and theoretical curves over the whole injection level range.

4.5.3 J_{0e} for planar emitters passivated by SiC_x stacks

The general behaviour of J_{0e} with the emitter sheet resistance (or inversely the junction depth) depends on the Surface Recombination Velocity, *SRV* [144,145]. The asymptotes of the J_{0e} are summarized in Fig 4.11 for Gaussian emitters with different N_s values as a function of the junction depth. For thin emitters (usually high sheet resistance) two opposite trends are found depending on *SRV*. Very low values of J_{0e} are found for well passivated emitters (*SRV* ~ 0), while very high values are obtained for non-passivated ones (*SRV* ~ 5×10^6 cm s^{-1}). As the junction depth increases (the sheet resistance diminishes) J_{0e} increases for those emitters well passivated and decreases for non-passivated ones. For the so-called opaque or deep emitters, with very low sheet resistance, J_{0e} does not depend on the surface recombination velocity because the recombination in the bulk of the emitter dominates over the surface recombination.

Experimentally, these general trends are observed for emitters passivated by the silicon carbide stacks. Fig 4.12 shows the measured J_{0e} dependency on R_{sh} for different thicknesses of the PAS layer. Two clear tendencies are observed: the passivation improves as the PAS layer thickness increases and it also improves due to the FGA treatment. Before FGA, the samples with single ARC layer (without PAS layer) show increasing values of J_{0e} with R_{sh}, indicating a high surface recombination velocity. On the other hand, for the thicker PAS layer the opposite tendency is found, revealing a low *SRV*. The intermediate cases lay in between. After the FGA, the four structures with different PAS layer thickness show an important improvement, especially for samples without PAS layer. The passivation quality was checked over five month period after the FGA, presenting a strong degradation for the single ARC layer and for the thinnest (30 s) PAS layer after this period. In particular, single ARC layers showed a complete de-passivated behaviour, with J_{0e} values even higher than the as-deposited case. Samples with PAS layer deposited for 60 and 90 s were found to hold the initial J_{0e} values. The corresponding J_{0e} values are plotted in Fig 4.13.

The effects aforementioned can be explained in terms of hydrogen passivation. The films obtained by decomposition of hydrogenated precursor gases contain a certain amount of hydrogen that is partially responsible for the surface passivation, decreasing the surface recombination velocity. Either in atomic or in molecular form, the hydrogen mobility is high even at temperatures below 400 ºC, and its distribution depends on the

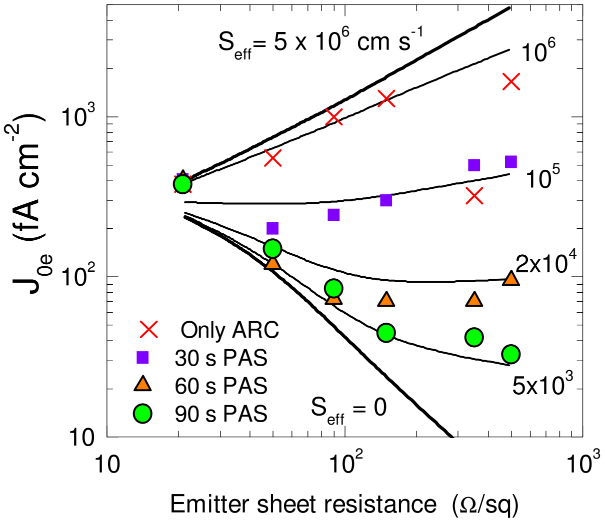

Figure 4.13. J_{0e} values (symbols), 5 months after the FGA treatment. Degradation is observed for the thinnest PAS layers (0 and 30 s deposited) while above 60 s the passivation quality is maintained. Theoretical curves (solid lines) for given values of *SRV* are plotted for comparison.

thermal processes applied. In the stacks with thickest PAS films (8 and 12 nm) the saturation of defects at the interface may come mainly from the Si-Si and Si-C bonds, while in the thinnest PAS films (0 and 4 nm) it may come mainly from the high content of hydrogen present in the ARC layer. This is why the FGA has a strong impact on the thinnest films, and it also explains why those films degrade faster.

It is clear that a PAS layer with a minimum thickness of 8 nm, corresponding to 60 s of deposition time, is required to achieve good surface passivation. With such PAS layers J_{0e} as low as 160 – 100 fA cm^{-2} can be obtained for deep emitters (≈ 40 – 60 Ω/sq), suitable for metal contacts by screen printing process. In the range of emitters suitable for evaporated contacts (≈ 100 Ω/sq) values around 70 fA cm^{-2} are obtained. In the case of lightly doped emitters, adequate for not contacted regions in selective emitters (≈ 200 – 500 Ω/sq), the best value obtained is around 30 fA cm^{-2}.

4.5.4 Surface recombination velocity

In order to evaluate the passivation quality, values of surface recombination velocity, *SRV*, have to be calculated. To this end, it is necessary to determine both phosphorus profile and the surface doping concentration (N_s), so that it is possible to distinguish the recombination within the emitter from the recombination at the surface.

The process of determination of surface recombination velocity in a highly doped region (emitter) is summarized hereafter:

1. Determination of emitter profile, i.e. the doping concentration as a function of the depth. It is performed by SUPREM characterization tool, correlated with the measured sheet resistance, and compared with SIMS measurements (section 4.5.1).
2. Lifetime measurement of the symmetric structure and extraction of the saturation current density, J_{0e}, as described in section 4.5.2.
3. PC1D simulation [26] of a *p-n* junction and generation of the corresponding dark *I-V* characteristic. The structure for simulation is the following:
    - Very thin *p*-type base (about 2 µm thick) with very high lifetime, about 10 ms (high resistivity and no SRH recombination). In this way, the recombination in the base can be neglected.
    - The emitter profile determined from SUPREM, at the front side.
    - A random value for the front surface recombination, $S_{\mathrm{eff,front}}$. We assumed a defect energy position located at the intrinsic level E_i and that the emitter is always working at Low Level Injection (LLI). This implies that surface recombination is dominated by the fundamental recombination velocity of the minority carriers (S_{p0} in our case). Therefore we use $S_{\mathrm{eff,front}} = S_{\mathrm{n0}} = S_{\mathrm{p0}} = S_{\mathrm{eff\ at\ LLI}}$ as input parameters.
    - No rear surface recombination, $S_{\mathrm{eff,back}} = 0$.

    Under these conditions, the recombination is only due to the front surface and the Auger plus radiative in the bulk emitter. The saturation current density for the *I-V* curve can therefore be fully attributed to the emitter, and the base component can be neglected:

    $$J_0 = J_{0e} + J_{0b} \approx J_{0e} \qquad (4.2)$$

4. Simulation of the dark *I-V* and extraction of parameters. The model used for the fitting is described by:

    $$I(V) = I_0\left(e^{V/qV_T} - 1\right) + I_{0rec}\left(e^{V/n_{rec}qV_T} - 1\right) \qquad (4.3)$$

    Where V is the applied voltage, q is the electron charge, $V_{\mathrm{T}} = k\ T\ /q$ is the thermal voltage, I is the total current, I_0 and $I_{0\mathrm{rec}}$ the saturation currents for the diffusion and recombination diodes, respectively, n_{rec} is the ideality factor for the recombination diode (normally equal to 2). The corresponding saturation current density, J_0, is obtained by simply dividing I_0 by the device area used in the PC1D simulation.

Steps 3 and 4 are repeated until the J_0 matches with the measured J_{0e}. Then, the surface recombination velocity in the emitter is the corresponding $S_{eff,front}$ obtained in step 3.

Concerning step 3, it is important to comment the effect of Band Gap Narrowing (BGN). As the doping concentration at the surface, N_s, increases, the band gap decreases, thus increasing the bulk recombination. Nevertheless, PC1D incorporates a lineal model for the shrinking of the E_g that is overestimated at high N_s values (see for example ref [138]). In PC1D it is not possible to modify this parameter. On the contrary, the excess of recombination provided by the wrong BGN model can be compensated by decreasing the Auger coefficient, C_n, which can be edited in PC1D. In order to obtain a suitable C_n term we simulated the *p-n* structure with the highest doped emitter (20 Ω/sq) and assuming no surface recombination ($S_{eff,front} = S_{eff,back} = 0$). Actually, in such very highly doped emitters the recombination is dominated by the bulk. C_n was lowered until the resulting J_{0e} value was the same than that determined from lifetime measurements. Then, the same C_n value can be employed in the rest of pre-diffused emitters, as the surface doping concentration does not vary significantly with the sheet resistance in such structures. From this procedure we obtained $C_n = 1.2 \times 10^{-31}$ cm^{-6} s^{-1}, while the default value in PC1D was $C_n = 2.2 \times 10^{-31}$ cm^{-6} s^{-1}.

Another argument to decrease the C_n term is provided by the experimental data of a passivated emitter with a drive-in process. The dependence of N_s with the sheet resistance in this case is significant. Because N_s has decreased, the error in the BGN committed by PC1D is smaller, so that the corresponding *p-n* junction could be simulated correctly. However, if we assume $C_n = 2.2 \times 10^{-31}$ cm^{-6} s^{-1} with $S_{eff,front} = S_{eff,back} = 0$, the J_{0e} predicted is still higher than the experimentally measured, indicating that C_n value is anyway overestimated.

In addition to the experimental $J_{0e}(R_{sh})$ curves, Fig 4.13 plots the resulting theoretical J_{0e} (R_{sh}) curves (solid lines) for given fixed values of *SRV*, ranging from 0 to 5×10^6 cm s^{-1}, which is close to the thermal velocity limit for silicon [138]. It can be seen that for each stack configuration a single *SRV* value reasonably fits the whole $J_{0e}(R_{sh})$ curve. This is again in agreement with the low variation of surface doping, N_s, due to the absence of a drive-in step, because normally *SRV* depends strongly on this value. For single ARC layers we obtain a *SRV* of about 10^6 cm s^{-1}, for the thinnest PAS layer (30 s deposited - 4 nm thick) it is about 10^5 cm s^{-1}. Finally, the structures with the two thickest PAS layer (60 and 90 s deposited) keep *SRV* around 10^4 cm s^{-1} at low R_{sh}. At higher sheet resistance values, *SRV* tend to be 2×10^4 and 5×10^3 cm s^{-1} respectively.

At very low sheet resistance J_{0e} converges to a single value, independently of the surface passivation treatment. Regarding the theoretical curves, the lowest R_{sh} achieved in our experiment (20 Ω/sq) could still show a certain degree of surface passivation. However, a complete de-passivated behaviour is observed for those samples, probably indicating a lattice damage within the emitter directly compared to high phosphorus concentration.

4.5.5 Comparison between SiN and SiC

Fig 4.14 shows a comparison between our two best SiC_x passivation schemes (PAS layer 8 and 12 nm thick) and several results for SiN_x taken from the literature. All of them refer to planar emitters, i.e. polished wafers without any texturing treatment. Special attention must be paid to direct comparison of the data without taking into account the emitter profile. For emitters with the same sheet resistance, there can be different doping profiles with different surface doping N_s. Reducing N_s by means of high temperature steps helps to achieve a higher passivation quality while maintaining R_{sh} virtually unaltered. To our knowledge, Kerr *et al.* reported the lowest published results for J_{0e} as a function of sheet resistance in phosphorus emitters passivated by SiN_x. In their process, a thermal oxidation at 900 ºC for 30 minutes was applied prior to SiN_x deposition. Aberle *et al.* [139] and Lenkeit *et al.* [140] perform a drive-in step (830 ºC, 20 min.) before the SiN_x deposition. Rohatgi *et al.* [101] apply stacks of thin oxide grown by RTO and SiN_x layers deposited in a remote PECVD. In this configuration, and in the range of 90 – 100 Ω/sq, both J_{0e} and N_s are similar to those reported by Kerr *et al.* in Ref. [138] (J_{0e} ~ 35 fA cm^{-2} and $N_s \sim 5 \times 10^{19}$ cm^{-3}). Additionally, in reference [101], when the RTO is omitted and no drive-in is used, both J_{0e} and N_s are higher but still better than in Ref. [139] and in Ref. [140]. The same passivation quality is achieved by Moschner *et al.* [141] applying SiN_x stacks (refractive index 2.1 and 2.4) and again without using a drive-in step. Since there is no use of drive-in, references [101] and [141] can be directly comparable to the process used in this work. We can conclude that the *n*-type emitter passivation level achieved by silicon carbide stacks is at least as good as that offered by silicon nitride. Furthermore, to

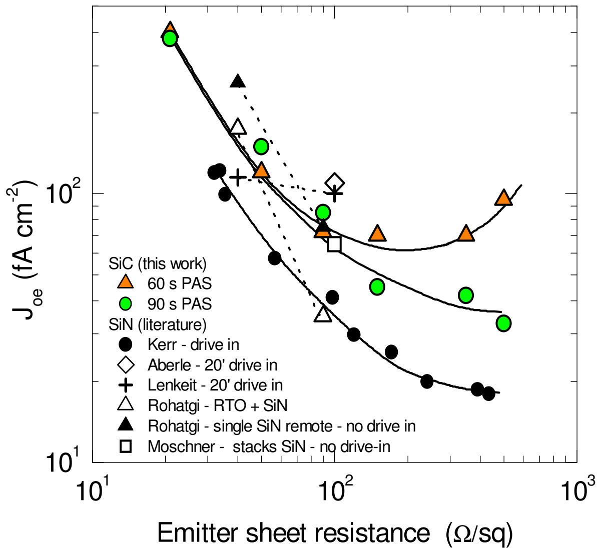

Figure 4.14. Comparison of J_{0e} of planar n^+-emitters passivated with SiC_x (this work) and SiN_x values reported in the literature: Kerr [138], Aberle [139], Lenkeit [140], Rohatgi [101], Moschner [141]. Lines are a guide to the eye.

achieve this level the silicon rich layer does not need to be 50 nm thick, as required for the passivation of *p*-type surfaces (Chapter 3).

4.5.6 Optical losses

From the optical constants it is possible to calculate the fraction of light transmitted to the bulk wafer, as well as the fraction reflected and that absorbed in the PAS layer. A multilayered system consisting of air/ARC/PAS/*c*-Si/air has to be considered, with the light entering from the ARC layer side. For each wavelength, interference phenomena can occur within the layers depending on the layer thickness and the corresponding optical constants *n* and *k* through the Fresnel coefficients at each interface, which relate the optical constants of two adjacent layers. When more than a layer is present, it is useful to calculate the Fresnel effective coefficients for the first one and iteratively apply the same procedure to all subsequent layers of the system, as it is explained in ref [146].

Figure 4.15 shows calculated optical losses due to the PAS layer and the fraction of light transmitted to the wafer, i.e. available for the solar conversion. Consistently, as the PAS layer thickness increases the optical losses become higher. Experimental values for single ARC layer are also plotted. They have been obtained from 1-$R(\lambda)$, where $R(\lambda)$ is the measured reflectivity. The agreement between theoretical and experimental values

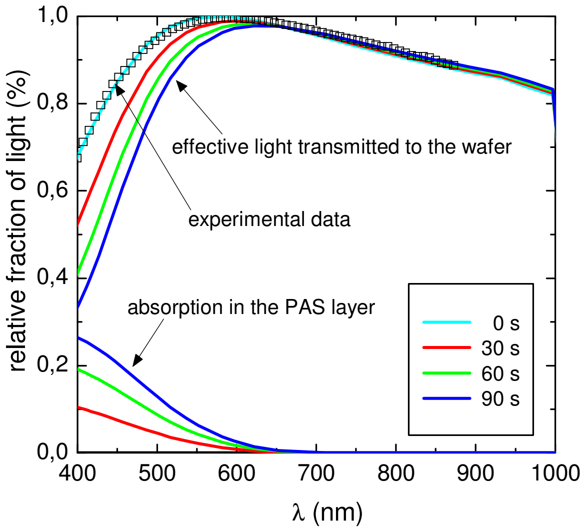

Figure 4.15. Lines: theoretical curves showing the fraction of transmitted light to the silicon wafer and absorbed by the PAS layer, modelled from optical constants and multilayer structure calculations. Squares: experimental values obtained from reflectance measurements for single ARC layers (0 s).

guarantees confidence with the model applied. In addition, the reflectivity measured is very similar to the resulting reflection spectra when standard single TiO_2 antireflective coatings are used [147].

4.5.7 Effects on the solar cell efficiency

To estimate the effect on solar cell efficiency, we chose the emitters with 50 Ω/sq and 90 Ω/sq from the whole series of wafers. Using PC1D software, we calculate the limits for the open circuit voltage (V_{oc}), the short circuit current (J_{sc}) and the cell efficiency (η) operating at 1 sun.

Bulk resistivity and thickness were the same as employed in the experimental procedure (0.95 Ω cm, 300 μm). Also, the emitter profiles were taken from the SUPREM simulations. To account for the optical losses calculated in the previous section, four different input files (for the four different passivation schemes) were built containing the effective reflectivity, i.e. considering the absorption in the PAS layer. For the electrical losses we consider Auger recombination as the only recombination process within the bulk, and perfect surface passivation in the rear side ($SRV = 0$). For the front side we employed $SRV = 10^6$, 10^5, 10^4 and 10^4 cm s^{-1} for 0, 30, 60 and 90 s of PAS layer respectively, which are values derived from Fig 4.13. We assumed values of 10^{-4} Ω for

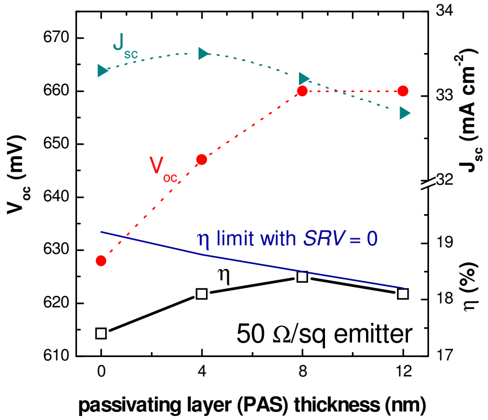

Figure 4.16. Theoretical limits of V_{oc}, J_{sc} and η for 50 Ω/sq emitters under standard test conditions (AM 1.5G, 300K), calculated from the J_{0e} and SRV values. The maximum efficiency of 18.4% is achieved for the PAS layer 8 nm thick. The limit for the efficiency with no surface recombination is also plotted.

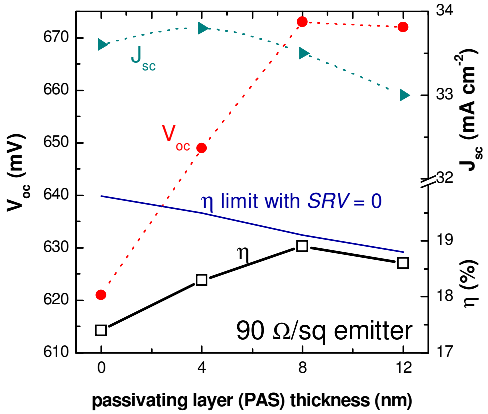

Figure 4.17. Theoretical limits of V_{oc}, J_{sc} and η for 90 Ω/sq emitters under standard test conditions (AM 1.5G, 300K), calculated from the J_{0e} and SRV values. The maximum efficiency of 18.9% is achieved for the PAS layer 8 nm thick. The limit for the efficiency with no surface recombination is also plotted.

both emitter and base contacts, and the shunt resistance was considered to be infinite. Finally, the I-V curves of the structures were simulated under standard test conditions (AM 1.5G, 300 K).

Figure 4.16 and 4.17 show the calculated results for V_{oc}, J_{sc} and η as a function of the nominal PAS layer thickness, showing that both emitter structures behave in the same way. As the PAS layer thickness increases the V_{oc} increases and reaches saturation. The trend for the J_{sc} is, as expected, the opposite. An optimum point is found for 8 nm of PAS layer thickness, whose corresponding efficiencies are 18.4 and 18.9% for the emitters with 50 Ω/sq and 90 Ω/sq respectively. To make clear the good emitter passivation achievable we also plot the limits for the efficiency considering a perfect surface passivation in the front side ($SRV = 0$) independently of the structure used to passivate. In the ideal case (no absorption in the passivating layer and no surface recombination) the maximum efficiencies achieved would be 19.2 and 19.8% for the emitters with 50 Ω/sq and 90 Ω/sq respectively. Clearly, the passivation obtained by the SiC_x stacks is excellent and the efficiency obtained in our case study is mostly limited by low J_{sc} due to the nonexistence of a texturing treatment.

4.6 Chapter conclusions

Surface passivation by silicon carbide stacks has been analyzed by varying the thickness of the inner layer (PAS). The study has been performed on low resistivity *p*-type wafers, suitable for solar cells performance, and pre-diffused n^+-type emitters, without requiring a further drive-in step.

The use of a carbon rich (ARC) led to several benefits. Firstly, the transparency and antireflective properties provided by a suitable refractive index ($n \approx 2$) are pre-requisites when applied at the front side of solar cells. For the rear side passivation this also helps to enhance internal reflection towards the bulk silicon. Secondly, the high content of hydrogen available in these films allows further improvement in surface passivation after forming gas anneal. Thirdly, it presents better stability than thin Si rich samples in front of long forming gas anneals as it may act as a hydrogen barrier. Lastly, together with the Si rich film it provides good electronic conditions when applied in PERC structures, as the stack prevents from shunting effects and is well behaved with the metal work function. This helped to achieve solar cells with *a*-SiC rear side passivation above 20% in efficiency.

However, the use of the passivating film (PAS), with undesired absorption of light, is still required to provide good surface passivation, either in *p*-type bases or in n^+-type emitters. Si rich layers thicker than 8 nm prevent from degradation of the surface passivation quality due to de-hydrogenation of the *a*-SiC/*c*-Si interface. This thickness is precisely the optimum for the passivation of n^+-type emitters at the front side, since it reaches a trade-off between surface passivation and optical losses.

CHAPTER 5

Phosphorus doped silicon carbon nitrogen alloys, SiCN(*n*)

5.1 Introduction

In Chapters 3 and 4 we have shown the applicability of phosphorus doped silicon carbide films to perform surface passivation of crystalline silicon. It was already shown in a previous work that the introduction of phosphorus represents a significant improvement respect to intrinsic films [32]. We have been able to resolve partially the absorptive behaviour of the passivating films by reducing their thickness and complete the passivation with antireflective layers. However, to provide enough amount of hydrogen this antireflective film had to be grown at a lower temperature than the passivating film. A process like this, involving two different temperature processes, is clearly far from the objectives of simplicity and robustness claimed for mass production of silicon solar cells. Furthermore, it has been found that when the passivating films are 4 nm or thinner the surface passivation degrades after a period of time at room temperature. Therefore, it would be preferable to find new growing conditions that ensure good surface passivation, antireflective properties and stability.

In the present Chapter, these new growing conditions are focused on the introduction of nitrogen to the silicon carbide material. It has already been demonstrated that intrinsic carbon nitrogen alloys a-SiC$_x$N$_y$(i) represent a further improvement compared to a-SiC(i) for the passivation of n-type wafers [148], reaching values of S_{eff} as low as 16 cm s^{-1}. With the aim combining the benefits of nitrogen and phosphorus, we study phosphorus-doped hydrogenated-amorphous silicon carbon nitrogen alloys, a-SiC$_x$N$_y$:H(n) as a new option for surface passivation. Hence, it represents the mixing between silicon nitride and silicon carbide.

The introduction of a film with five elements (silicon, carbon, nitrogen, phosphorus and hydrogen) could be regarded as complicated and therefore useless for the photovoltaic industry, which is in the search of low-cost and simplified processes for mass production, especially when the silicon nitride has demonstrated excellent capabilities. However, some different properties between silicon nitride and silicon carbide (or silicon carbon nitrogen alloys) can be of interest in certain fabrication processes. Firstly, silicon nitride provides a strong field effect passivation mainly due to a high positive charge that is calculated to be around 2.5×10^{12} cm^{-2} [99], while in silicon carbide it appears to be one order of magnitude lower (see Chapter 3 or reference [149]). A second property is that silicon nitride can be etched in HF, while silicon carbide cannot. A third issue concerns the introduction of phosphorus in the film. It is interesting since it could serve as an emitter layer in a HIT structure, with the benefit of more transparency achieved thanks to the carbon/nitrogen incorporation, thus avoiding loss in photocurrent. Finally, a recovery of surface passivation after long time anneals at high temperature has been recently observed after initial strong degradation at short annealing times [150] (see Chapter 6). Another interesting property of nitrogen in SiC systems is that it acts as a shallow donor impurity of microcrystalline silicon carbide phases [151]. This concept has been used to fabricate n-i-p amorphous silicon solar cells with a μc-SiC n-type region acting as open window and hence allowing a higher short circuit currents than in typically amorphous silicon phases [152] . All this issues make interesting the study of such ternary alloys.

With the aim to investigate the applicability of *a*-SiC_xN_y:H(*n*) films to all kind of concepts of solar cells, the surface passivation is tested on low resistivity *p*-type and *n*-type silicon wafers, as well as on *n*-type emitters. It would be very interesting to study also their possibilities in *p*-type emitters. However, the technical opportunities of our laboratory kept this option unavailable at the moment of performing this work. Variation of the composition from silicon rich (highly absorptive) to carbon or nitrogen rich (highly transparent) films is performed to find optimum surface passivation. As in Chapter 4, stacks of different compositions are applied to combine excellent passivation and good antireflective properties.

5.2 Deposition conditions of SiCN(*n*) films

The purpose of this experiment was to establish a correlation between films composition and surface passivation. Additional interest was focused on finding transparent films (rich in carbon or nitrogen) with good surface passivation.

Except gas flows, all deposition conditions were kept constant and considered to be optimum. Temperature and total pressure in the chamber were set to 400 ºC and 300 mTorr respectively, as they were optimized for the surface passivation of *n*-type wafers by means of intrinsic SiCN(*i*) films in a previous work [148]. RF power was set to 30 W (10% of source) to achieve homogeneity in at least 4” wafers and the deposition time was set to 5 minutes. According to results obtained in Chapter 3, deposition times longer than 5 minutes would lead to thicker films with higher light absorption but without significant improvement in surface passivation. In this configuration, the film thicknesses obtained were around 40 nm for those films rich in silicon, with the usual growing rate of 8 nm min^{-1} found for all silicon rich films in this thesis. As the content of nitrogen or carbon increases the deposition rate decreases monotonically, until 4 nm s^{-1} for films with high content of carbon or nitrogen. In those cases the experiments were repeated doubling deposition time to achieve again thickness of 40 nm. The SiCN(*n*) films are treated in this Chapter as ternary alloys produced by the decomposition of three gases:

- Silane mixed with 5% of phosphine, $SiH_4 + PH_3$
- Methane, CH_4
- Molecular nitrogen, N_2

Phospine was not considered as a separate gas since it was varied by the same proportion than silane. In turn, the amount of hydrogen incorporated in the films cannot be controlled. Instead of nitrogen, ammonia (NH_3) could be used in a further work to explore different alternatives of the ternary alloy.

Gases flows were varied to achieve different film compositions. In these experiments, we used relative flow parameters defined as follows:

$$\mathrm{X} \equiv \mathrm{CH_4} / \left[\mathrm{CH_4} + \left(\mathrm{SiH_4} + \mathrm{PH_3}\right)\right] \qquad (5.1.a)$$

$$\mathrm{Y} \equiv \mathrm{N_2} / \left[\mathrm{CH_4} + \left(\mathrm{SiH_4} + \mathrm{PH_3}\right) + \mathrm{N_2}\right] \qquad (5.1.b)$$

The X parameter takes into account the ratio between methane and silane flows and the parameter Y indicates the relative nitrogen flow to the total gas flow. Both are normalized to 1, then either both X and Y values close to 0 correspond to silicon-rich films, while carbon (nitrogen) rich films are deposited with X (Y) tending to 1. Two scans were performed with the aim to incorporate more carbon or nitrogen to the films. In the first scan, we kept constant the nitrogen flow to 15.7 sccm and the total gas flow to 75 sccm (equivalent to $Y = 0.21$). Then, X was varied between 0.25 and 0.9. For the second scan, X was kept constant to $X = 0.4$ and Y varied between 0.14 and 0.83.

5.3 Surface passivation of on *p*- and *n*-type wafers.

As in the whole thesis, low resistivity substrates were used to focus on the applicability of surface passivation on silicon solar cells. Float zone, <100> oriented, planar silicon wafers were employed, with a resistivity of 0.95 Ω cm for the *p*-type wafers (acceptor density, $N_A = 1.6 \times 10^{16}$ cm^{-3}) and 1 Ω cm for the *n*-type ones (donor density, $N_D = 5 \times 10^{15}$ cm^{-3}). They were cleaned in a piranha solution ended with a HF dip and immediately introduced into the PECVD reactor to perform symmetrical depositions of the a-SiC_xN_y:H(n) films.

An example of lifetime measurement for both wafer types with the corresponding bulk lifetime limits and the values at 1 sun illumination indicated by arrows is given in Fig 5.1. Surface recombination velocities values lower than 10 cm s^{-1} (5 cm s^{-1}) are obtained in a wide injection level range in this case. The lifetime values were converted to surface

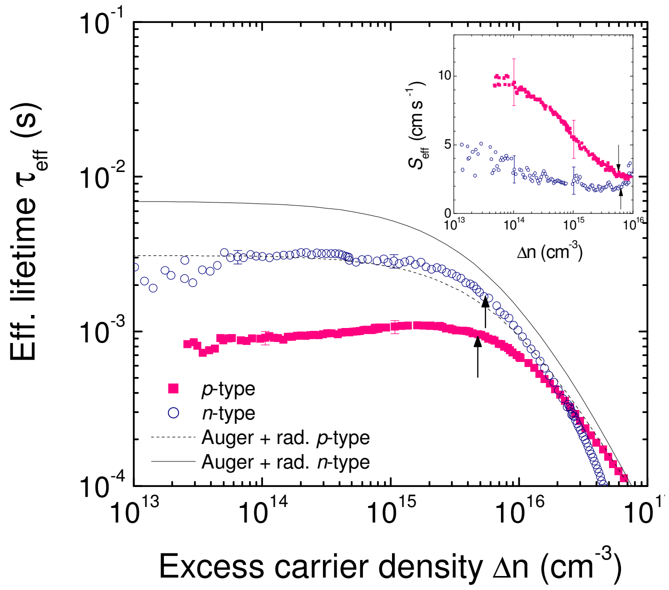

Figure 5.1. Example of lifetime curves for *p* an *n*-type wafers passivated by SiCN(*n*). The Auger plus radiative bulk lifetime are plotted, and the arrows indicate 1 sun illumination levels. The inset shows the corresponding S_{eff} values.

recombination velocity values employing equation (1.66) and are presented as an inset in the Figure.

5.3.1 Dependence on gas flows

Fig 5.2 shows the dependence of S_{eff} values at 1 sun illumination on the refractive index of the deposited film for both types of substrates. The best passivation is obtained by the silicon-richest film in both substrates showing extremely low S_{eff} values of 3 cm s^{-1} for *p*-type wafers and 2 cm s^{-1} for *n*-type wafers. They correspond to open circuit voltages values of 721 and 697 mV, respectively This represents an important improvement compared with the passivation level previously achieved by our silicon carbide material for *p*-type (S_{eff} = 7 cm s^{-1} with *a*-SiC$_x$(*n*) in Chapter 3) and *n*-type (S_{eff} = 16 cm s^{-1} with intrinsic *a*-SiC$_x$N$_y$:H [148]) silicon wafers of similar resistivity. Actually, they offer similar passivation level as intrinsic amorphous silicon reported values, for which in *p*-type 1.5 Ω cm silicon wafers S_{eff} values around 3 cm s^{-1} were obtained [109]. The inconvenience of amorphous silicon is that the low deposition temperatures (around 200 ºC) required to achieve good interface hydrogenation cause instability under high temperature anneals, while our silicon carbide films, grown at 400 ºC, should be in principle more stable. Next Chapter focuses in this issue.

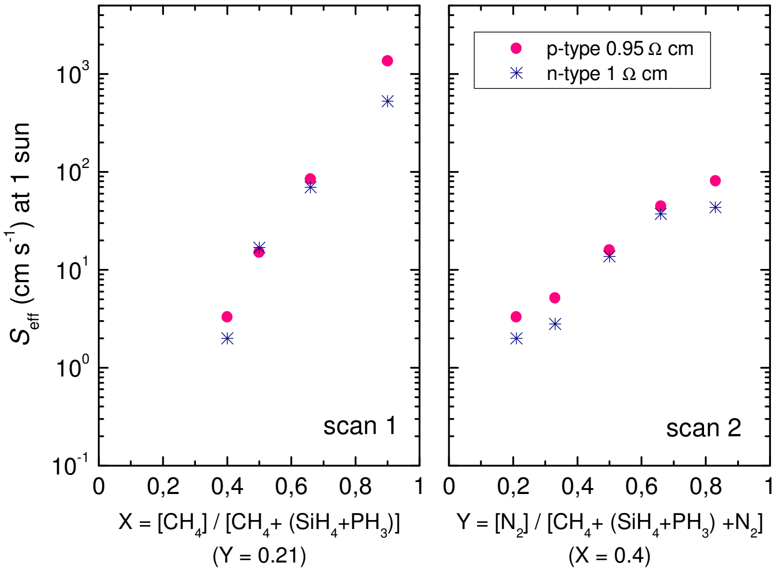

Figure 5.2. Surface recombination velocity as a function of the gas flow ratios X and Y varied in two scans.

5.3.2 Ellipsometry measurements, Tauc-Lorentz parameters and correlation with passivation mechanisms

Spectroscopic ellipsometry measurements were performed in a wide spectral range (from 200 to 1600 nm) with a phase-modulated ellipsometer (UVISEL, Jobin Yvon Horiba). The pseudo dielectric functions measured were fitted using the dispersion law based on the Lorentz oscillator and the Tauc joint density of states for amorphous materials [130]. In this model, the energetic dependence of the imaginary part of the dielectric function (ε_2) is given by:

$$\varepsilon_2(E) = \frac{A\, E_0\, C\, (E - E_g)^2}{(E^2 - E_0^2)^2 + C^2\, E^2}\, \frac{1}{E}, \qquad E > E_g \qquad (5.2)$$

where E is the photon energy, E_g is the optical bandgap, and A, C and E_0 are the amplitude, the broadening term and the center terms of the Lorentz oscillator function, respectively. These four parameters allow the structural characterization of the material and they are plotted in Figure 5.3 as a function of the flux gases ratio, X or Y. The optical bandgap ranges from 1.73 eV to 2.09 eV, the broadening term ranges from 2.66 eV to 6.04 eV, the center term range from 3.47 to 6.72, and finally the amplitude term decreases from 183 to 70 eV as the carbon/nitrogen content increased.

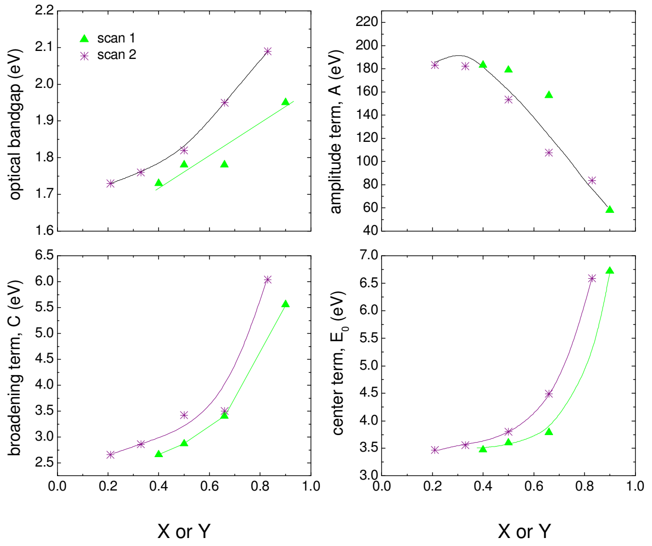

Figure 5.3. Tauc-Lorentz parameters determined from ellipsometry

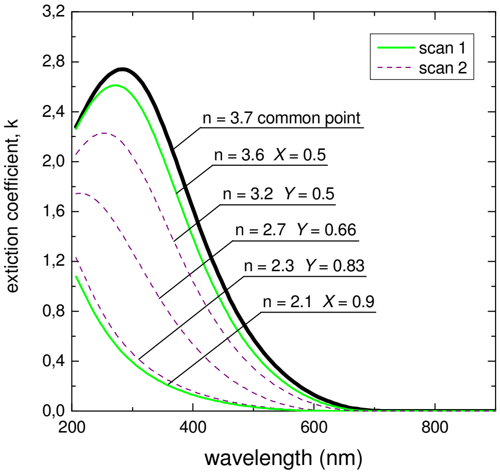

Figure 5.4. Extinction coefficient for several *a*-SiCN(*n*) films. Labels indicate the refractive index measured at 633 nm and the corresponding gas flow ratio.

The real part of the dielectric function, ε_1, is obtained from ε_2 using Kramers-Kronig integration, leading to direct determination of the refractive index, *n*, and the extinction coefficient, *k*. This last value is plotted in Fig 5.4 for several compositions used in the study, labeling the refractive index at 633 nm and the fraction of gases flows X or Y. The common point, which is also the optimum passivating point in this study, presents strong absorption of light due to its silicon rich composition. Fig 5.5 shows the relation between refractive index, *n*, at 633 nm as a function of the X or Y parameters for the two scans. As the carbon or nitrogen content increase (increasing X or Y) the refractive index decreases as expected.

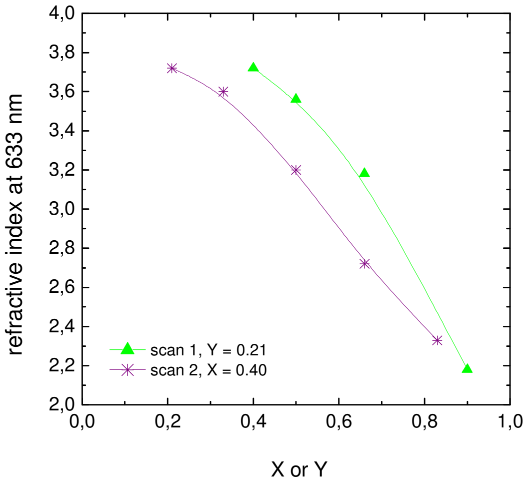

Figure 5.5. Refractive index for the *a*-SiCN(*n*) films measured at 633 nm.

5.3.3 Stacks with SiCN(n) films

In order to reduce light absorption, stacks of silicon rich / carbon rich films were already suggested for silicon carbide films in Chapter 4, obtaining good passivating and antireflective properties applied on *n*-type emitters. The same strategy was used in the present Chapter for *a*-$SiC_xN_y(n)$ films, combining passivating films (n = 3.6, S_{eff} = 5 for *p*-type) and antireflective films (n = 2.3, S_{eff} = 90 for *p*-type). An important advantage in the present case respect to the SiC stacks developed in Chapter 4 is that the processing temperature is the same for both layers (400 ºC) and no FGA treatment was applied, thus simplifying the process. The passivating film thickness was varied from 8 to 24 nm, while the antireflective coating thickness was kept constant at 70 nm. As the passivating film thickness was reduced, the surface recombination velocity increased, as shown in Fig 5.6. The corresponding effective optical constants n_{eff}, k_{eff} and thickness d_{eff}, are calculated from the initial values using equations from the model explained in reference [153]:

$$\left(n_{eff}^2 - k_{eff}^2\right) = \frac{\left(n_1^2 - k_1^2\right) d_1 + \left(n_2^2 - k_2^2\right) d_2}{d_1 + d_2} \tag{5.3.a}$$

$$\left(n_{eff}\ k_{eff}\right) = \frac{\left(n_1\ k_1\right) d_1 + \left(n_2\ k_2\right) d_2}{d_1 + d_2} \tag{5.3.b}$$

$$d_{eff} = d_1 + d_2 \tag{5.3.c}$$

The effective optical constants for the stacks used are summarized in Table 5.1.

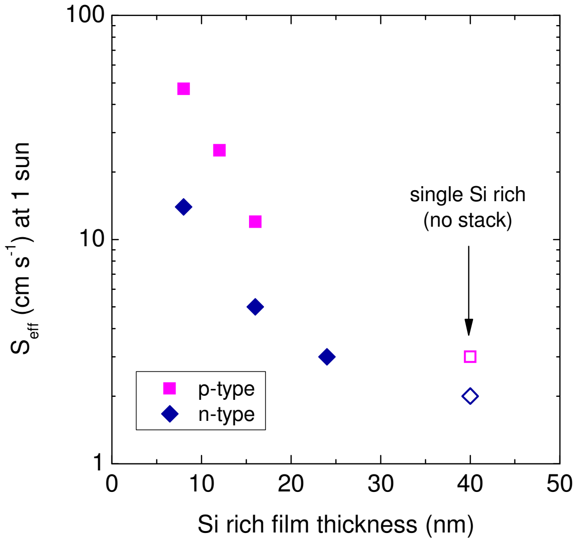

Figure 5.6. Surface recombination velocity at 1 sun of low resistivity wafers (~ 1 Ω cm) achieved by SiCN(*n*) stacks of different thicknesses. The thickness of the antireflective coating is around 70 nm.

Table 5.1. Effective optical constants and thickness at 633 nm for SiCN(*n*) stacks used in Fig 5.6. The antireflective coating thickness is 70 nm.

PAS thickness	n_{eff}	k_{eff}	d_{eff} (nm)
8	2.44	0.005	78
12	2.51	0.008	82
16	2.57	0.010	86
24	2.67	0.013	94

5.3.4 Surface recombination velocity as a function of the refractive index

The S_{eff} values determined in Fig 5.2 (for single SiCN(*n*) films) and 5.7 (for stacks) are repeated in Fig 5.7 for *p*-type wafers and Fig 5.8 for *n*-type wafers as a function of the refractive index at 633 nm. As a comparison, values of S_{eff} at the same resistivity with pure *a*-SiC(*n*) and pure *a*-SiN are plotted, the latter coming from the decomposition of ammonia (NH_3) gas, rather than the nitrogen (N_2) used in this work. For silicon carbide compounds, with or without nitrogen, S_{eff} is minimized for films with refractive index equal to 3.72. This value is close to the refractive index of amorphous silicon, (the literature spreads values between 3.5 and 4.5 at similar grown conditions [123-125,154,155]), indicating that composition for the optimum films is very rich in silicon. However, the presence of nitrogen in the PECVD chamber leads to an important improvement of passivation respect to SiC(*n*), despite their refractive index are identical.

Then, when the carbon or nitrogen flows are increased to diminish the refractive index, the surface recombination velocity is increased. However, while an incorporation of carbon (scan 1) leads to very high values of S_{eff}, nitrogen incorporation (scan 2) leads to values as low as 90 cm s^{-1} (for *p*-type) and 50 cm s^{-1} (for *n*-type), that are acceptable for the passivation of industrial solar cells. In turn, the stacks provide excellent passivation results with refractive indexes that are not far from what it would be desirable (between 1.9 and 2.4).

5.4 Passivation of diffused n^+-emitters by SiCN(*n*) stacks

As in Chapter 5, it is interesting to analyse the passivation properties of *n*-type emitters to be applied at the front side of a working solar cell. Again, stacks of silicon rich / carbon or nitrogen rich layers have to be used in order to combine passivation and antireflective properties. In this case the analysis is performed not only on pre-diffused emitters, but also in emitters with drive-in. All wafers were cleaned using a RCA sequence ended with an HF dip.

5.4.1 Pre-diffused emitters

Phosphorus diffusions using Planar Diffusion Sources [142] were performed on planar, FZ, *p*-type, 0.95 Ω cm, <100> oriented wafers. The process has already been detailed in section 4.5.1. In the present case, emitters with a sheet resistance R_{sheet} = 130 Ω/sq were obtained, without performing a drive-in.

Stacks of SiCN(*n*) films were deposited symmetrically on the wafers. The inner, silicon rich film were deposited for 1 and 2 minutes, with corresponding thickness of 8 and 16 nm, respectively. Figure 5.9 shows the lifetime curves measured by the QSS-PC technique. Lifetime fittings were performed using the two model diodes as explained in section 4.5.2. On the one hand, as can be seen it Fig 5.9, very low values of minority saturation current density, J_{0e}, have been found in both cases. We can be confident in the determination of these values as the fittings agree well with the experimental values at high injection level range, in which the diffusion diode is the dominant mechanism. On

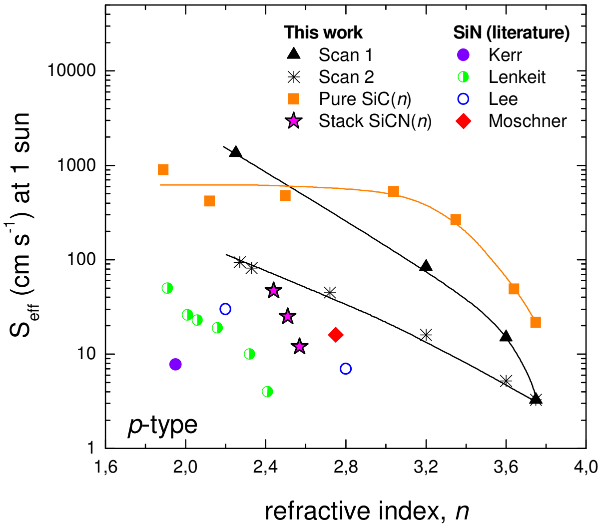

Figure 5.7. S_{eff} **values for low resistivity** p**-type wafers passivated with** a**-**SiC_xN_y**:H(**n**) as a function of the refractive index measured at 633 nm. Values for pure silicon nitride from the literature (**$Y = 0$**) and pure** a**-**SiC_x**(**n**) (**$X = 0$**) are plotted for comparison: Kerr [28], Lenkeit [156], Lee [100], Moschner [141].**

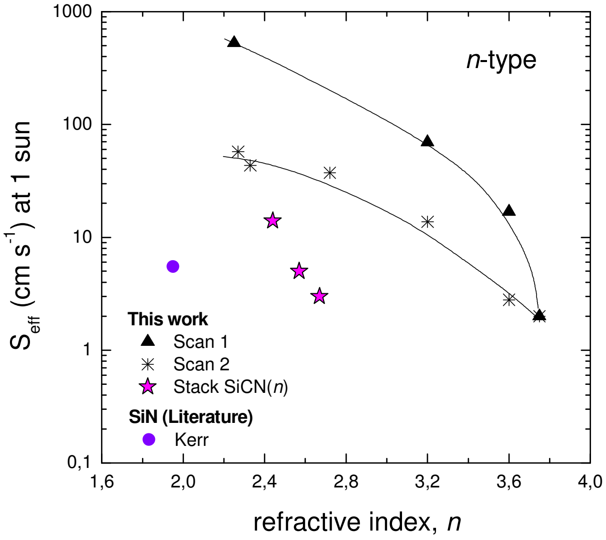

Figure 5.8. S_{eff} **values for 1 Ω cm** n**-type wafers passivated with** a**-**SiC_xN_y**:H(**n**) as a function of the refractive index measured at 633 nm. Values for pure silicon nitride from the literature (**$Y = 0$**) are plotted for comparison: Kerr [28].**

the other hand, certain degree of recombination at the space charge region is found, as relatively high values of J_{rec}, around 2.5 nA cm^{-2}, are encountered. The determination of J_{rec} is unclear as the experimental values at low injection densities, which dominate this recombination mechanism, do not agree well with the experimental values. Even though, we are unable to reproduce accurately the Depletion Region Modulation effect, which in turns is only appreciated in the 1 minute deposition case. The behaviour encountered here differs from that obtained in the previous section for the passivation of of *p* and *n*-type bases. In that case, very low values of S_{eff} were obtained in the whole injection level range, only increasing significantly at the lowest excess carrier densities.

Next step in the analysis of emitter passivation is the determination of S_{eff} at low injection densities. It is required to know the $J_{0\mathrm{e}}(R_{\mathrm{sheet}})$ dependence and the phosphorus profile of the emitter to establish a relation between $J_{0\mathrm{e}}$, R_{sheet} and S_{eff}. Refer to section 5.5.4 for a detailed explanation of the process. Figure 5.10 shows the $J_{0\mathrm{e}}(R_{\mathrm{sheet}})$ dependence for the silicon carbide stacks developed in Chapter 4 and the new stacks with ternary *a*-SiCN(*n*) alloys. Also the theoretical curves for fixed S_{eff} values are plotted. It can be seen that for the *a*-SiCN(*n*) alloys we get a reduction of S_{eff} from 5000 to 1000 cm s^{-1}.

5.4.2 Emitters with drive-in

In this section emitters with four different sheet resistances were used. After the phosphorus diffusion, phosphorus glasses were stripped with a HF dip at 5% and a thermal oxidation at 900ºC for 30 minutes was performed. This process allows excellent passivation at the time that the phosphorus is driven-in to the bulk wafer, thus reducing the phosphorus concentration at the *c*-Si surface, N_s, and enhancing the junction depth. The determination of the final phosphorus profiles was performed by the Electrochemical Capacitance Voltage Profiling (ECV Profiling) technique [157], using a Wafer Profiler CVP21 that was available at the Institut für Solarenergieforschung in Hameln/Emmerthal (ISFH). The profiles for the driven-in emitters are shown in Fig 5.11.

Saturation current densities were measured for the driven-in emitters in four different states: (1) SiO_2 passivated, after thermal oxidation, with a FGA at 400 ºC; (2) Al-annealed, by aluminium evaporation / annealing / aluminium etch, remaining the thermal oxide; (3) Bare emitter, after etching the thermal oxide; (4) After PECVD deposition of SiCN(*n*) stacks (Si rich for 1 and 2 minutes) All results are plotted together in Fig 5.12, with the corresponding theoretical curves for different surface recombination velocities. For comparison, we plot results for silicon nitride that are state in the art for driven in emitters [28].

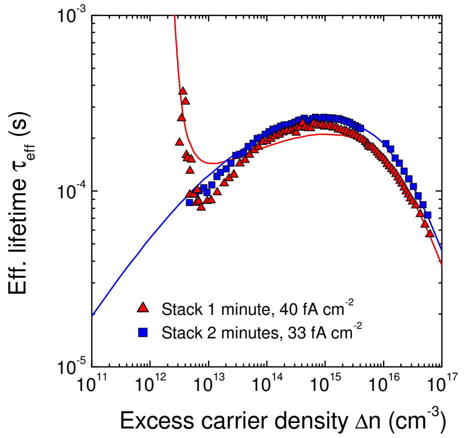

Figure 5.9. Lifetime curves of pre-diffused planar emitters passivated by *a*-SiCN(*n*) stacks, with Si rich film deposited for 1 min (8 nm thick) and 2 min (16 nm). Symbols: experimental curves. Lines: simulated curves.

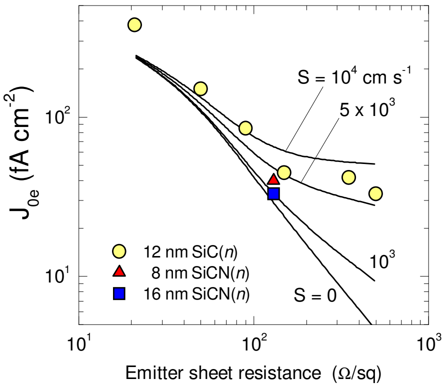

Figure 5.10. J_{0e} – R_{sh} curves for pre-diffused emitters passivated by stacks. The introduction of nitrogen to the SiC material clearly improves surface passivation. Theoretical curves indicate the surface recombination velocity values at low injection densities.

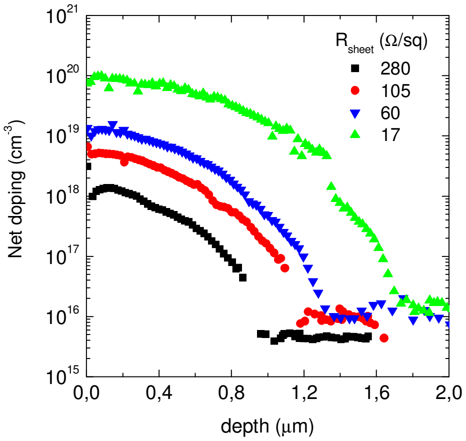

Figure 5.11. Emitter profiles for driven-in emitters measured by the Electrochemical Capacitance Voltage Profiling (ECV Profiling) technique.

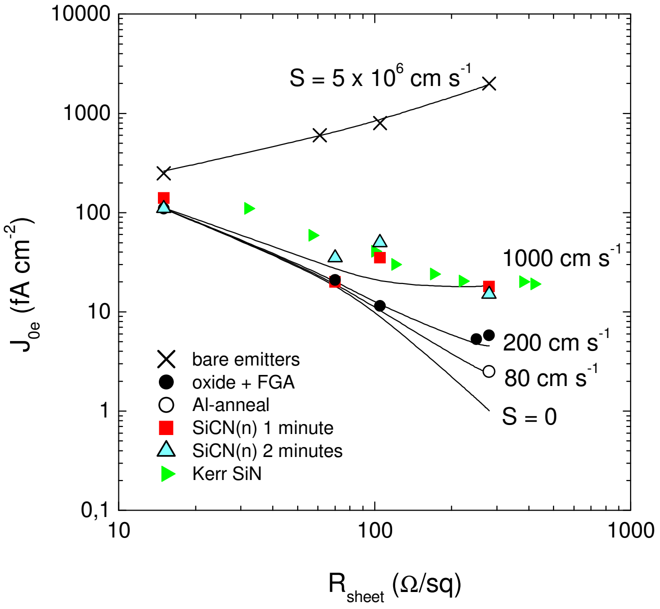

Figure 5.12. Saturation current density, J_{0e}, for driven-in emitters passivated by different configurations. Silicon nitride passivation (Kerr) shown is from reference [28].

The best surface passivation is provided by the al-anneal scheme, followed by the thermal oxidation with FGA. Then, the passivation level achieved by the SiCN(*n*) stacks is slightly inferior and similar to the level achieved by silicon nitride. This demonstrated that the SiCN(*n*) stack could be good candidate to be applied at the front side of solar cells.

5.5 Chapter conclusions

In this Chapter we have explored the passivating properties of silicon, carbon and nitrogen alloys doped with phosphorus. The introduction of nitrogen in the *a*-SiC(*n*) films leads to an important lowering of surface recombination velocity. Excellent surface passivation is possible for both *p*-type and *n*-type wafers at a suitable resistivity around 1 Ω cm. A correlation is observed between increasing refractive index (enhancing undesired absorption in the film) and improvement in surface recombination velocity.

To lower the optical absorption while keeping the surface passivation quality stacks of thin passivating films combined with antireflective films were proposed, with satisfactory results. The same stacks were tested in *n*-emitters with and without a drive-in, achieving extremely low surface recombination velocity values comparable with those provided by thermally oxidation with a FGA process.

CHAPTER 6

Time and thermal time stability of silicon carbide films

6.1 Introduction

When producing electricity from solar energy, both economical costs and the energy used to manufacture the modules have to be taken into account. In general, there is a common agreement that the energy recovery time in silicon solar cells is nowadays less than 3 years and depends on the type of silicon used (ribbon, multicrystalline or monocrystalline) [158,159], while the payback time for economical cost is significantly higher. Strong efforts are being done by the whole photovoltaic community to reduce these payback times with several strategies (thinning wafers, using low cost materials, etc.). In addition, solar cells need to keep a certain degree of stability in efficiency during a minimum period of 20 years working under normal operation conditions (temperatures up to 60 – 70 °C under illumination), which can be indeed very different from standard test conditions (25 °C with 1 sun-AM 1.5 spectrum). Surface passivation must then keep its properties for at least the same period.

On the other hand, the majority of industrial processes use the screen-printing technique to apply the metallic contacts. This is a very robust and well established process that involves high temperature steps after surface passivation. In such scheme metallic pastes are printed through a mesh mask to define the front and rear grids. The n^+-emitter, located at the front side, is usually printed with silver paste, while the rear side is normally printed by aluminium. Then, a co-firing step at high temperatures for a few seconds is performed to simultaneously achieve ohmic contacts at both sides. The process is done in belt furnaces, or in rapid thermal anneal (RTA) furnaces. Firing profiles (peak temperatures, times, number of plateaus and up and down ramps) have been extensively studied (see for instance Ref. [160]), with a general agreement that more than 700 °C (and up to 900 °C) are required for the standard silver pastes, while about 600 °C are enough for good aluminium contact (the temperature that form eutectic between Al and Si is 577 ºC). Despite low temperature pastes are recently being under investigation, at the moment surface passivation techniques with stability under high temperature processes are needed. Silicon nitride passivation has already demonstrated good stability after firing processes, either with single deposition of silicon nitride [106,107] or in combination with thin silicon oxide layer grown by Rapid Thermal Oxidation (RTO) [101].

While stability of silicon nitride passivation has been extensively explored for many years and by many research groups, application of silicon carbide for the passivation of silicon solar cells is still at its most primary state. Therefore, this Chapter presents preliminary research about time and thermal stability of surface passivation by amorphous silicon carbide. Time stability test consists of measuring lifetime as a function of the time passed after film deposition. Thermal stability is explored by firing the lifetime test samples at high temperatures (from 500 to 900 ºC) and at different annealing times. The passivation films are those presented in Chapters 3, 4 and 5. In some cases, the films have been deposited on textured wafers. Texturing treatment is crucial to enhance light absorption, but it presents the inconvenient that the final surface area is approximately 1.3 times higher than in planar surfaces, and the planes exposed are <111> oriented. Both factors can influence on the surface passivation and its stability on time and under high thermal processes.

6.2 Time stability

6.2.1 Stability of different passivation schemes

The problem of lifetime degradation on time has already been observed in Chapter 4 when using stacks of silicon carbide to passivate n^+-type emitters. When the silicon rich film was 8 or 12 nm thick the passivation was stable during the time of analysis (5 months), while when it was 4 nm or did not exist at all, fast degradation of lifetime occurred. In this section we explore the stability on time provided by different configurations of silicon carbide. Symmetrically passivated wafers were simply stored in dark conditions and their lifetimes were measured over a long period of time. The passivation films analysed are the following:

- Intrinsic silicon carbide films, silicon rich, SiC(*i*), [32]
- Phosphorus doped silicon carbide films, silicon rich, SiC(*n*)
- Intrinsic silicon carbon nitrogen alloys, SiCN(*i*), [32]
- Phosphorus doped silicon carbon nitrogen alloys, SiCN(*n*)
- Stacks of Si rich / C rich films

All films analyzed are rich in silicon, and with an optimized FGA treatment applied, except for the SiCN(*n*). The wafers used were Float Zone with planar surfaces. Doping type, resistivity and thickness are detailed in Table 6.1, as well as S_{eff} values. The stacks used for this test have been applied on lightly doped emitters (350 Ω/sq).

To show the degradation of surface passivation, Fig 6.1 plots normalized lifetime values as a function of time for the structures aforementioned. The labels correspond to those in Table 6.1. In some cases the lifetime values increase with time, which we assume to be due to a decalibration of the QSS-PC instrument during the long time performance of the experiment (up to 7 years). The first direct comparison is between intrinsic and phosphorus doped SiC films. It is shown that intrinsic films are much more stable than phosphorus doped films. It has been clearly stated that phosphorus doped SiC produces a better surface passivation, for equivalent doping concentration, than intrinsic SiC [32], and the cause has been attributed to a higher incorporation of hydrogen in the films [129], thus producing more effective saturation of dangling bonds. However, either in molecular or atomic form, hydrogen is very mobile and effuses easily from the interface [161].

Table 6.1. Samples used for analysis of lifetime degradation with time. All of them were subjected to FGA treatment after SiC deposition, except SiCN(*n*).

Film	Wafer			Initial conditions	
	type	ρ (Ω cm)	*W* (μm)	τ (μs)	S_{eff} (cm s^{-1})
SiC(*i*) – Si rich	*p*	3.3	350	214	≤ 82
SiC(*n*) – Si rich	*p*	0.85	400	825	12
SiCN(*i*) – Si rich	*n*	1.9	365	1060	12
SiCN(*n*) – Si rich – without FGA	*p*	0.95	300	878	6
Stack 4 nm – SiC(*n*) Si rich / C rich	*p*	0.95	300	41	*N.A.* (emitter)
Stack 8 nm – SiC(*n*) Si rich / C rich	*p*	0.95	300	111	*N.A.* (emitter)

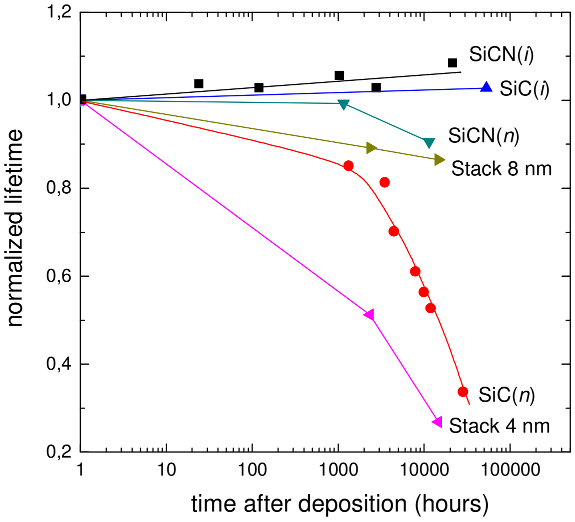

Figure 6.1. Lifetime degradation with time in structures passivated by silicon carbide films. Details of the different layers are shown in Table 6.1.

For the phosphorus doped SiC(*n*) passivated wafer the decay time has been analysed employing exponential decay behaviour (see Fig 6.2). The time constant is around 11000 hours and the final lifetime values (after infinite time after the deposition) would be around 250 μs. In this case it would represent, at 1 sun illumination, an implied open circuit voltage $V_{oc} \approx$ 670 mV, that is still a reasonably good value for industrial type solar cells (the initial value was 702 mV).

When analyzing ternary SiCN alloys, the same direct comparison between intrinsic and phosphorus doped films can be done, i.e. intrinsic films keep more stable surface passivation. However, in the present case the degradation in phosphorus doped films is not as strong as in SiC(*n*) films. Clearly, the introduction of molecular nitrogen (N_2) in

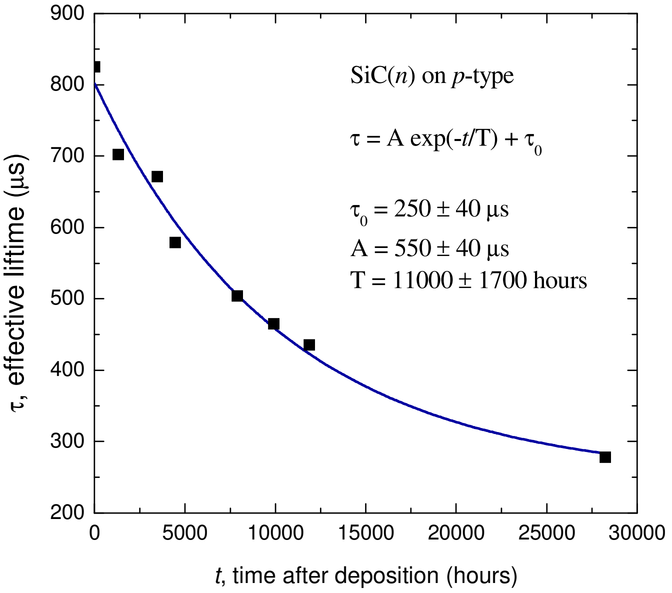

Figure 6.2. Temporal decay for *p*-type wafer (0.85 Ω cm) passivated by phosphorus doped amorphous silicon carbide SiC(*n*).

the PECVD chamber to promote SiCN alloys has some benefits with still unknown causes. One of them could be a higher amount of charge density provided by nitrogen (the reported values of fixed charge in silicon nitride system is 2.5×10^{12} cm^{-2} [99]) being therefore less sensitive to the presence of dangling bonds and reducing the importance of hydrogen at the interface. Another effect could be related to the structure of the compound. Actually silicon nitride deposited with diluted silane in molecular nitrogen produces better results in surface passivation than that produced only from decomposition of silane and ammonia [28].

Finally, the stacks present a semi-stable behaviour when the silicon rich film thickness is 8 nm, and a fast degradation when it is only 4 nm. This is again in agreement with the effusion of hydrogen, which plays a major role for passivation of stacks with thin Si rich films and a minor role in thick ones.

Despite intrinsic silicon carbide films offer excellent time stability, the initial surface passivation is in general lower than that offered by the phosphorus doped films once they are degraded. Therefore, the best solution to achieve good initial conditions and time stability would be by using silicon carbide stacks (with or without nitrogen) or intrinsic silicon carbon nitrogen alloys.

6.2.2 Influence of FGA on time stability

The forming gas anneal (FGA) plays an important role in surface passivation by SiC. In Chapter 4 and 5 we have analysed extensively this behaviour and shown that the same treatment in FGA can lead to very different results depending on the structure (single layers or stacks), thickness, and composition of the SiC films. In polished wafers passivated by silicon rich SiC(*n*) we have already shown that lifetime can increase to a factor up 1.3 after FGA. In the next section we will see that this factor can be much more important in textured samples. It would be interesting to find out if any delay between deposition and FGA treatment affect on the final passivation level or on the time stability.

Four *p*-type polished wafers (0.95 Ω cm) were passivated by silicon rich SiC(n) films grown at 400 ºC (similar conditions than in Chapter 4). The lifetimes were measured 30 minutes after deposition. A FGA treatment at 400 ºC for 20 minutes was applied to all wafers, but at different times:

Wafer 1: 1 hour after deposition
Wafer 2: 1day after deposition
Wafer 3: 1 week after deposition
Wafer 4: no FGA

The lifetime was then measured regularly to see changes with the FGA and degradation effects. Figure 6.3 is summarizing the whole process, indicating the lifetime at usual 1 sun illumination.

In all cases, the initial lifetime values are significantly lower than expected for this type of wafers and passivating film, indicating that the experiment is affected by some contamination. What is more, the initial lifetime values are not equal, indicating small non-homogeneities in the process. However, with the precision of the experiment, the test is valid to see that in all cases the degradation is starting to be significant 1000 hours after deposition and that the time in which the FGA is applied is not relevant for the surface passivation stability. The order of magnitude for the time constant ($1/e$) is around 10^4 hours (~ 400 days) in all cases, but with considerably high uncertainty (around 7000 hours).

In the end, it can be concluded that a time delay between deposition and FGA treatment does not affect either the final passivation level or the time stability.

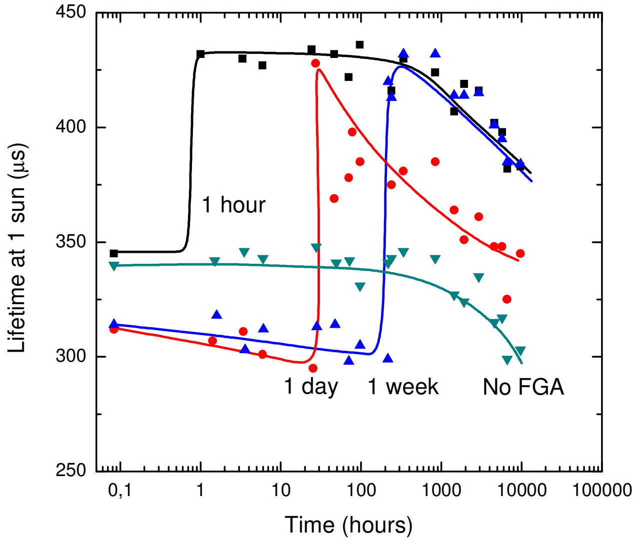

Figure 6.3. Temporal decay for *p*-type wafer (0.95 Ω cm) passivated by phosphorus doped amorphous silicon carbide SiC(*n*) and with the FGA treatment performed at different times after the PECVD deposition.

6.3 Thermal stability at high temperatures

In the present section we provide extensive analysis of surface passivation dependence under high temperature (above 500 ºC) anneals. Different test samples and test films are used. In order to clarify the reader, a brief summary of every experiment is presented hereafter:

Section 6.3.1 studies silicon carbide films developed in Chapters 3 and 4. The process is as follows:

1. Sample preparation
    a. Substrate
        i. All wafers are textured
        ii. Doping: *p*-type bases (40 Ω cm) and n^+-type emitters (60 Ω/sq)
    b. Films depositions
        i. Single Si rich SiC(*n*)
        ii. Stacks of Si rich SiC(*n*) and C rich SiC(*i*)
    c. Forming Gas Anneal (FGA) treatment to enhance lifetime before thermal stress. Previous experiments are done to choose optimum annealing time.

At the end of sample preparation process there are 4 different types of structures to be tested: single films on *p*-type wafers, single films on n^+-type emitter, stacks on *p*-type wafers, and stacks on n^+-type emitters.

2. Thermal stress in RTA furnace
    a. Temperatures 500, 600, 700 and 900 ºC
    b. Annealing times from 3 s to more than 3 h

Section 6.3.2 studies annealing effects on silicon carbon nitrogen alloys developed in Chapter 5:

1. Sample preparation
    a. Substrate
        i. All wafers are planar
        ii. Doping: *p*-type bases and *n*-type bases, both 1 Ω cm, and n^+-type emitters (130 Ω/sq)
    b. Films depositions
        i. Single silicon rich films, SiCN(*n*)
        ii. Stack of Si rich C rich films, SiCN(*n*)
    c. No FGA applied
2. Thermal stress in belt furnace (equivalent to firing after screen printing)
    a. Temperature 720 °C, for 35 s
    b. Temperature 900 °C, for 10 s

6.3.1 Thermal stability of SiC(n), single and stacks

Films developed in Chapter 3 and 4 have been deposited on *p*-type wafers and n^+-type emitters, both with textured surfaces. Except silicon carbide depositions, samples preparation, thermal treatments and characterization were lead in the Engineering Department at the Australian National University.

6.3.1.1 Sample preparation

As starting material, we used <100> oriented, Float Zone, *p*-type, 40 Ω cm, *c*-Si wafers, with an initial size of 12.5 × 12.5 cm. The wafers were then subjected to an alkaline saw Damage Removal Etch (DRE) for 13 min, which produced truncated pyramids, thus providing a partial texturing treatment and a final thickness of 270 μm.

To prepare n^+-p-n^+ structures, half of the wafers were cleaned in a RCA solution and inserted into a tube furnace for phosphorus diffusion at 855 ºC for 30 minutes using $POCl_3$ as the dopant source and resulting in 60 Ω/sq emitters. Then the phosphorus glass was stripped in buffered HF.

After another RCA cleaning step the sample preparation ended with an HF dip to remove any grown oxide. Silicon carbide deposition of films followed. To clarify the different structures tested we establish a nomenclature as in Chapter 4. Then, the phosphorus-doped silicon-rich layer is labelled as PAS, remarking its passivating properties, while the carbon rich layer is labelled as ARC, indicating that it acts as an antireflective coating. When only Si rich layers are produced the scheme will be called ***single***, while PAS + ARC structure will be labelled as ***stack***. The deposition parameters are very similar to those employed in Chapter 4. The differences are the growing temperature for the Si rich film (400 ºC in the present case, previously 350 ºC) and the thickness for this film in the stack (16 nm in the present case, previously from 4 to 12 nm). All parameters are summarized in Table 6.1. Therefore, four different structures are analysed: *p*-type bare wafers and emitters passivated by single layers and stacked layers. Figure 6.4 shows a schematic of the four different configurations tested. After silicon carbide depositions the wafers were cut into 2.5 × 2.5 cm samples, to provide possibilities of different tests.

Before starting the firings at high temperature it would be convenient to maximize the lifetime of the test samples, so that any probable degradation caused by the thermal stress can be more easily observed. Therefore, series of anneals in Forming Gas at low temperature were performed at 400 ºC in steps of 10 minutes.

Fig 6.4 plots the evolution of lifetime as a function of the FGA time. In bare *p*-type wafers, the lifetime increases after 10 minutes by a factor about 8 and 15 for *single* and *stack* schemes, respectively. Surprisingly, after the first FGA the stack structure gives much better passivation quality than the single layer, which in principle contains the best composition to this end. Then for the PAS layer saturation is reached and finally a small degradation after 60 minutes is found. This behaviour is slightly different from the experiment performed in Chapter 4 on planar surfaces, in which the evolution is less

Table 6.1. Deposition parameters for the PAS and ARC films

		PAS (Si rich)	ARC (C rich)
RF power	(W cm^{-2})	0.043	0.086
temperature	(ºC)	400	300
pressure	(mTorr)	335	315
SiH_4+PH_3	(sccm)	29.5	-
SiH_4	(sccm)	-	2.8
CH_4	(sccm)	24.3	32
deposition time	(min)	5 (*single*) 2 (*stack*)	11
thickness	(nm)	40 (*single*) 16 (*stack*)	70

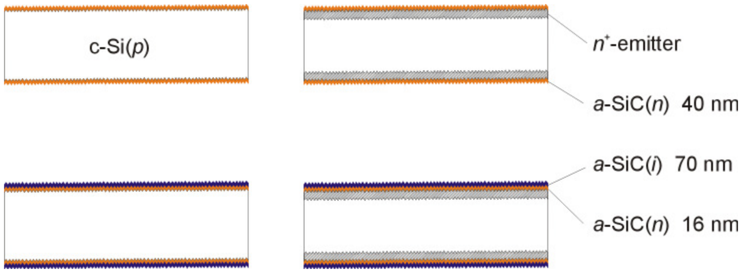

Figure 6.4. Schematic of the four structures for thermal test on textured wafers.

pronounced and a clear maximum at 20 minutes is reached. The difference may arise from the different surface treatment, exhibiting in the present case the truncated pyramids. Performed anneals under nitrogen atmosphere led to similar evolution as the FGA (not shown), indicating that the forming gas plays a minor role than the high hydrogen concentration present in the silicon carbide layers.

For the stacks, the maximum lifetime is found at 30 minutes of anneal, although the strongest increase results again for 10 minutes. Then the behaviour is in essence the same as for the single layers. The lowest values for the surface recombination velocity are 16 and 8 cm s^{-1} (at $\Delta n = 10^{14}$ cm^{-3}) respectively for the single and stacked layers.

Additional anneals in Forming Gas were also applied to the n^+-type emitters. The evolution is essentially the same as reported for *p*-type wafers (not shown), i.e. a fast improvement after 10 minutes, and with better surface passivation for the stack structures.

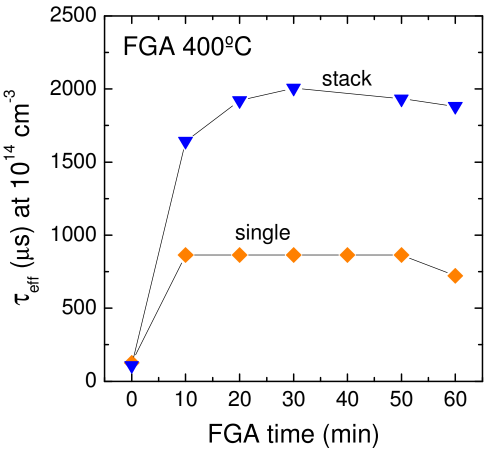

Figure 6.4. Evolution of lifetime as a function of the FGA time in *p*-type, textured wafers (40 Ω cm) for *single* and *stack* deposited films.

Regarding the evolution of lifetime shown in Fig 6.4 samples to be tested at high temperatures were subjected to FGA at 400 ºC for 10 minutes in order to achieve good initial surface passivation.

6.3.1.2 Thermal stress

Once textured, passivated and with a FGA treatment to enhance lifetime, the samples were to perform analysis of lifetime dependence with thermal processes. Simulations of a screen printing cofiring process were performed in a Rapid Thermal Anneal (RTA) furnace as explained hereafter. A typical screen printing firing temperature profile (see Fig 6.5) was chosen with a initial ramp at 21 ºC s^{-1}, a plateau at 450 ºC for 50 seconds, another ramp at 50 ºC s^{-1}, a peak temperature (T_{peak}) for a peak time (t_{peak}) and finally a very fast decrease. The peak temperatures employed were 500, 600, 700, 800 and 900 ºC, while the duration of the peak ranged from 3 s to more than 3 h in some cases.

The firing steps for *p*-type wafers are summarized in Figures 6.6 and 6.7. They provide information about what would be the interface quality of the rear side of a solar cell if it was fired after screen printing metallization. For the single layer fast degradation is found even at short times (less than 10 seconds) of the peak temperature. This degradation is faster for higher temperatures. However, a recovering seems to start at long firing times. This is especially noticeable for the firing at 600 ºC.

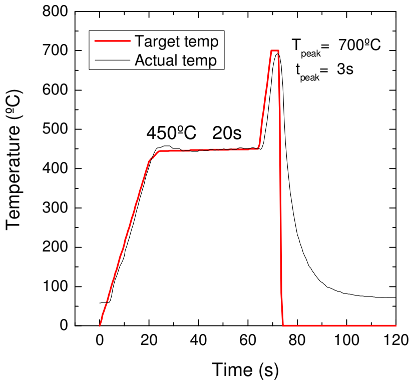

Figure 6.5. RTA profile used for the high temperature experiments. In this case the peak is at 700ºC for 3 s. A previous plateau at 450ºC for 20 s is present in all the firing steps.

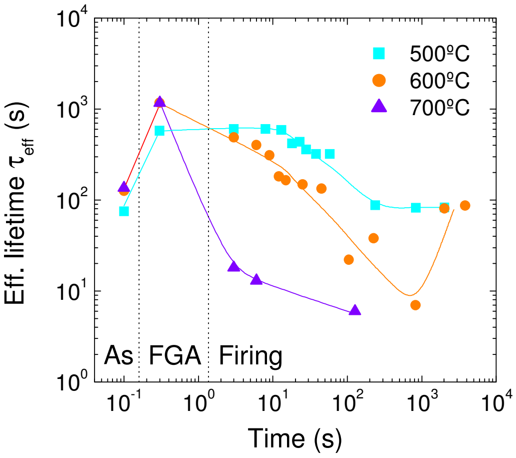

Figure 6.6. Evolution of lifetime in *p*-type, textured wafers (40 Ω cm) passivated with *single* layers after the simulation of a cofiring process at several peak temperatures.

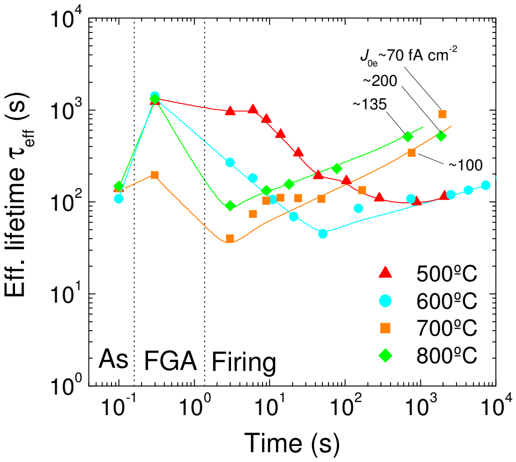

Figure 6.7. Evolution of lifetime in *p*-type, textured wafers (40 Ω cm) passivated with *stacks* single layers after the simulation of a cofiring process at several peak temperatures.

The same scenario is shown for the stack structure, but in this case the recovering is much more noticeable. After an initial strong degradation, a recovering in lifetime is early observed at few seconds from the initial firing, especially when the firing temperature increases. This recovering can be attributed to the phosphorus diffusion coming from the phosphorus doped silicon rich layer (PAS), thus creating a *p-n* floating junction that establish a field effect passivation, as explained in reference [162]. The purpose of that work was the fabrication of n^+-type emitters from the amorphous silicon carbide layer, diffusing the phosphorus to the *c*-Si and/or re-crystallizing the film. Thus, passivated emitters were obtained skipping conventional phosphorus diffusion in tube furnace, and with the additional benefit of using a material with higher bandgap acting as window layer. In the present case it is interesting to note that the highest lifetime is provided by the stacks structures, which seems to indicate better phosphorus diffusion than the single layers. This seems to be contradictory because the single phosphorus doped layers are thicker than the phosphorus doped layers in the stacks, and therefore contain a bigger doping source. An explanation for this could be that the ARC layers may act as barriers for the phosphorus diffusion, thus avoiding the effusion to the exterior.

Simulations of the $\tau(\Delta n)$ curves were performed using the two diodes model (section 1.2.4, formula (1.36)). Values of the emitter saturation current density (J_{0e}) for the diffusion diode are indicated in Fig 6.7 for the longest annealed points, i.e. it is assumed that those points correspond to structures with emitter behaviour. The best J_{0e} value is 70 fA cm^{-2}, which corresponds to firing at 700 ºC for 42 minutes. This low value suggests the formation of a lightly doped emitter. Regarding the system as a passivated interface (i.e. not considering the emitter) and applying formula (1.66) the resulting S_{eff} is less than 15 cm s^{-1}, a value that can be considered sufficiently good for wafers of this resistivity. The analysis of the complete curve reveal that it is not possible to fit the curves using an ideality factor $n = 2$ for the recombination diode, which is in principle the normal value for crystalline silicon *p-n* junctions. Instead, a factor $n < 2$ needs to be employed. This reinforces the hypothesis that the emitter is lightly doped and thin, so that the space charge region may contact the surface, allowing an increase of the recombination. Therefore, these junctions could act as good Back Surface Field (BSF) structures, but not as proper emitters in solar cell structures.

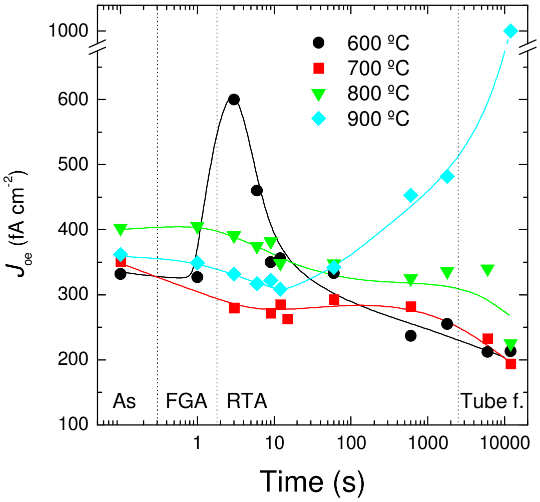

Figure 6.8. Evolution of minority saturation current density (J_{0e}) in *n*-type emitters (60 Ω/sq) passivated with *single* layers after the simulation of a cofiring process at several peak temperatures.

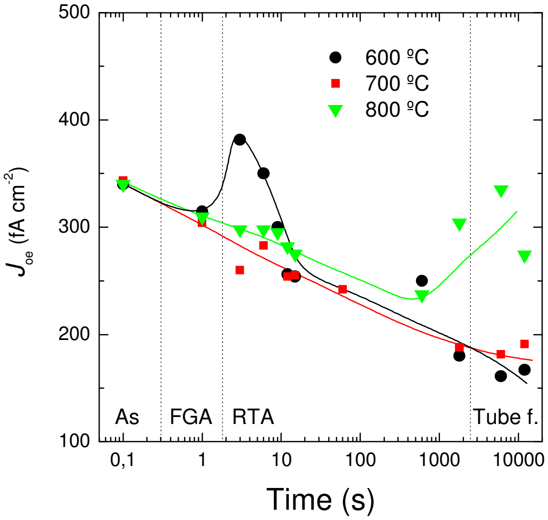

Figure 6.9. Evolution of minority saturation current density (J_{0e}) in *n*-type emitters (60 Ω/sq) passivated with *stacks* layers after the simulation of a cofiring process at several peak temperatures.

The results of thermal stress on n^+-type emitters are summarized in Figs 6.8 and 6.9, showing the J_{0e} evolution after every firing process. As for the p-type wafers, an initial FGA for 10 min was applied, followed by subsequent firings in RTA furnace. However, the latest anneals resulted to be very long and were completed in a conventional tube furnace, as indicated in the Figures.

In the case of PAS layers (Fig 6.8), short times do not seem to affect strongly the quality of passivation. Only at 600 ºC there is an initial increase of J_{0e} that recovers at about 10 seconds. Longer time anneals decrease the J_{0e} when the temperatures range between 600 and 800 ºC, probably due to a combined reduction of the surface doping at the interface due to a drive in of the conventionally pre-diffused emitter. At 900 ºC there is a clear degradation of the electronic properties when the firing time exceeds more than 100 seconds. Such degradation could be attributed to diffusion of contaminants in the furnaces into the bulk material. To confirm or reject this possibility we applied the so-called iron test [163], which consists of subjecting a certain wafer to light soaking. If interstitial iron is present in the bulk silicon the lifetime of a wafer after light soaking is higher than the lifetime of the same wafer stored in the dark. In our case the diffusion of contaminants was confirmed by the iron test.

Concerning the stack layers (Fig 6.9), the evolution is in essence the same as with PAS layers, but providing better results. When the firing is done at more than 700 ºC a change in colour of the layer is observed, indicating a changing of the antireflective properties. Further investigations are required to determine whether there is an effect on the layer thickness or its composition, and how to correct the initial deposition conditions so that good antireflective properties are kept after the firing.

6.3.2 Thermal stability of SiCN(n)

In this section thermal stress has been applied in wafers passivated by the ternary alloys developed in Chapter 5. Simulation of firing was lead in a belt furnace typically used after a screen printing of the metallic pastes. Such experiments were performed at the University of Basque Country (UPV), Department of Engineering (TIM group).

The thermal stress was applied to *p*-type and *n*-type wafers and to *n*-type emitters with the following features:

- *p*-type Float Zone wafers, <100>, 300 µm, 1 Ω cm, double side polished
- *n*-type Float Zone wafers, <100>, 575 µm, 1 Ω cm, single side polished
- *n*-type emitters (130 Ω/sq)on the *p*-type wafers aforementioned. They were pre-diffused by Planar Diffusion Sources (PDS) under the same conditions detailed in Chapter 4. The final sheet resistance was 130 Ω/sq.

All substrates were passivated by single and stacks ternary alloys of SiCN(*n*). The nomenclature for the deposited films is similar to the employed for the whole thesis:

- PAS (*number*). Indicates silicon rich films (refractive index at 633 nm is $n = 3.6$) that supply good surface passivation. The *number* in brackets indicates the deposition time for this film. The film thickness is easily determined considering that the deposition time is approximately 8 nm min^{-1}.
- ARC. Indicates a carbon rich film ($n = 2.3$) and its thickness was kept at 70 nm.

Two different firing profiles, typically used at UPV, were applied:

1. Peak temperature at 720 °C for 35 s
2. Peak temperature at 900 °C for 10 s

Figure 6.10 summarizes the processes done for *p*- and *n*-type wafers, indicating in any case the passivation schemes and the thermal process applied. The *n*-type emitters were only passivated by stacks films and their results are expressed in Table 6.2. The first thing that can be concluded from this experiment is that the configurations with single PAS films are highly instable under high temperature process at short times, as the effective surface recombination velocities reach high values. These are especially high for *p*-type wafers (around 10^4 cm s^{-1}). On the other hand, when applying thermal stress to stacks it is possible to keep S_{eff} under 200 cm s^{-1} for *p*-type wafers and under 20 cm s^{-1} for *n*-type if the PAS film is deposited for at least 2 minutes (~ 16 nm thick). For the emitters (Table 6.2) the results appear to be even better, as the minority saturation current density is kept under 50 fA cm^{-2} in all processes.

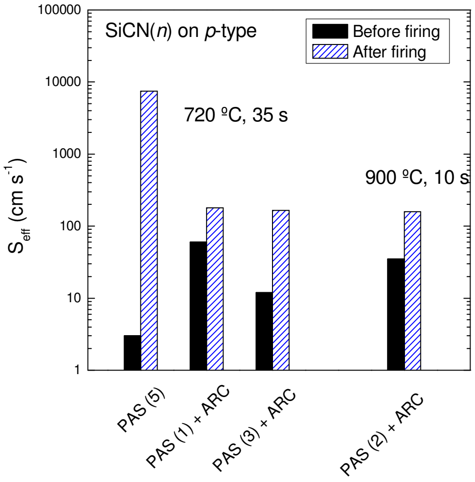

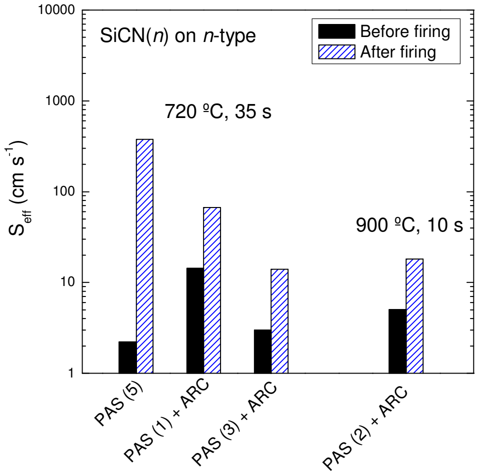

Figure 6.10. Firing of *p*- and *n*-type wafers passivated with differents schemes of ternary alloys SiCN(*n*).

Table 6.2. Firing of pre-diffused *n*-emitters (130 Ω/sq) passivated with ternary alloys SiCN(*n*).

SiCN(*n*) film	**J_{0e} fA cm^{-2} before**	**firing process**	**J_{0e} fA cm^{-2} after**
PAS (2) + ARC	35	900 ºC 10 s	< 50
PAS (1) + ARC	40	720 ºC 35 s	< 50

6.4 Chapter conclusions

In this Chapter we have explored the stability of surface passivation provided by different passivation schemes, as a function of the time after being deposited and under several thermal stresses applied.

The phosphorus-doped silicon carbide films exhibit better surface passivation than the intrinsic films. However, certain degradation on time is observed for these layers, while intrinsic ones appear to be much more stable in the period of time analysed (6 years). Introducction of nitrogen leads to better stabilities of lifetime, although some degradation is still observed for SiCN(*n*) passivation schemes.

Extensive analysis of thermal stress at low and high temperature has been performed for silicon carbide films (without nitrogen) on textured wafers, including *p*-type bases and *n*-type emitters. High temperature anneals in *p*-type bases present a recovery of lifetime after an initial fast degradation. This is probably due to the creation of a *p*-*n* junction that performs a field effect passivation. For *n*-type emitters a general and slight improvement in surface passivation was observed in all cases, except for those at the highest temperature used (900 ºC), in which degradation was attributed to diffusion of contaminants. All the experiments performed on textured wafers were done with single and stack films, the latest showing in all cases better stability and surface passivation properties.

Simulation of screen printing firing process in phosphorus-doped, ternary silicon carbide alloys, SiCN(*n*), present strong degradation when using single films. This process is equivalent to that analysed for the textured wafers subjected at high temperatures for short times (around seconds). On the other hand, the firing applied to stacks shows relatively good stability, which is especially given in *n*-type wafers (1 Ω cm) and in n^+-type emitters (130 Ω/sq).

Regarding the whole Chapter, it is clear that the use of stacks of silicon rich/carbon rich films provides better stability against thermal processes, regardless the films contain phosphorus or nitrogen. At the same time, the introduction of nitrogen to the SiC material is in any case beneficial as it offers best surface passivation level and posterior stability. Therefore, we can conclude for this Chapter, as well as for the whole thesis, that stacks of passivating and transparent phosphorus doped ternary silicon carbon nitrogen alloys is the best configuration for surface passivation by means of silicon carbide material.

CHAPTER 7

Conclusions and future work

7.1 Conclusions

The present work has been focused in the passivation of crystalline silicon by amorphous silicon carbide with three main objectives:

1. Consolidate silicon carbide as good candidate in photovoltaic solar cells passivation by achieving very low values of effective surface recombination velocity in low resistive wafers.
2. Perform passivation of phosphorus doped emitters by means of transparent and antireflective silicon carbide films to be applied at the front side of solar cells.
3. Demonstrate durability of passivation properties as well as stability under high temperature processes.

To achieve the three of them a series of experiments have been developed, discovering at the same time some interesting properties of the material:

- ✓ The level of passivation has been characterized by means of the Quasi-Steady State Photo Conductance (QSS-PC) technique to measure the effective lifetime of minority carriers. The lifetime vs. excess carrier density curves have been fitted using the Girisch model to extract the important recombination parameters of charge density and fundamental recombination velocity of electrons (or holes). Including the Depletion Region Modulation (DRM) effect into the simulations has been very helpful to enhance the accuracy of the fittings.

- ✓ The best surface passivation for the amorphous silicon carbide films is achieved by phosphorus-doped silicon-rich films, achieving in low resistive *p*-type substrates effective surface recombination values as low as 7 cm s^{-1} at 1 sun illumination, which corresponds to 709 mV in implied open circuit voltage. Unfortunately, the films cannot be applied at the front side of solar cells because the Si rich composition leads to strong light absorption in the film that does not contribute to the photocurrent.

- ✓ One important property of these films is that surface passivation improves with the film thickness by diminishing the fundamental recombination velocity. The charge density, which is responsible for the field effect passivation, is kept constant. Experiments in Forming Gas Anneal (FGA) to provide hydrogenation of the *a*-SiC/*c*-Si interface are in agreement with such behaviour. Thin films are not able to keep good surface passivation in long annealing times, while thick films resist better to long anneals.

- ✓ The value of the charge density created in the amorphous film seems to be dependent only on the doping type and doping density of the *bulk crystalline silicon*. For all deposition conditions (even for those who led to very different composition) the charge was invariable at a given resistivity.

- ✓ The lifetime dependence on the corona charge density applied to different wafers passivated by different silicon carbide films is not a peak, as it would have been expected, but a step that has been also observed in *p-n* junctions passivated by silicon oxide. This result and the previous one enumerated suggest that the charge density of the *a*-SiC/*c*-Si system depends on the filled interface states density, i.e., on the Fermi level position, rather than on a fixed charge stored in the *a*-SiC film.

- ✓ It was not possible to develop a transparent (carbon rich) film with a good surface passivation level. The only solution to achieve passivation with antireflective properties has been provided by stacks of thin (less than 16 nm, to minimize absorption) silicon rich films with carbon rich films. Not only is the carbon rich film transparent but it provides more stability under long FGA treatments. It is believed that this layer acts as a barrier for hydrogen, avoiding its effusion from the interface, and therefore keeping the saturation of dangling bonds.

- ✓ The stacks have resulted in very good surface passivation level on n^+-type emitters. Experimental measurements of surface passivation and optical properties have been used to calculate the efficiency of a solar cell passivated by stacks of different Si rich film thickness. The optimum thickness that reaches a trade-off between optical losses and surface passivation is 8 nm for planar wafers.

- ✓ The stacks are also especially useful when applied at the rear side of a PERC solar cell. Beside of being transparent, the carbon rich layer is a good dielectric and isolates the metal from the crystalline silicon. Without this layer shunting and coupling between metal and c-Si appear, leading to lower open circuit voltage values. The causes seem to be related to the work function value of the metal. The practical application of the stacks has been the development of a PERC solar cell with efficiency above 20%. It was developed in collaboration with the Fraunhofer Institut Solare Energiesysteme (ISE).

- ✓ The passivation level provided by the silicon carbide can further be improved by introducing nitrogen during the deposition of the films. This leads to phosphorus-doped ternary silicon carbon nitrogen alloys. Excellent surface passivation has been achieved in low resistive wafers, with surface recombination velocity values of 3 and 2 cm s^{-1} for *p*-type and *n*-type wafers, respectively.

- ✓ As in the case for pure silicon carbide, stacks of silicon rich / carbon (or nitrogen) rich films provided excellent surface passivation with antireflective properties, especially when applied to n^+-emitters.

- ✓ Although phosphorus doped films provided much better surface passivation than intrinsic films, they degrade much faster with time. The problem of degradation is less sensitive when a stack is used.

- ✓ Thermal stress experiments at high temperatures (> 500 °C) demonstrate that short times anneals provoke a strong degradation of the surface passivation properties. However, when anneals are produced at long times there is a recovering of the lifetime. The most probable cause is the formation of an emitter due to the phosphorus content in the silicon carbide film (by diffusing towards the *c*-Si or by crystallization of the *a*-SiC film), establishing a field effect passivation. It could also be related to a densification of the film that would help to diminish the number of non-saturated defects at the interface. The behaviour is anyhow more favourable when stacks are used.

- ✓ In ternary silicon carbon nitrogen alloys the thermal stress leads to a strong degradation for single silicon rich samples, while stacks of carbon (or nitrogen) rich samples degrade weakly and keep good surface passivation level.

To summarize all the work developed in this thesis, we can conclude that within the family of amorphous silicon carbide compounds the best option for surface passivation of crystalline silicon solar cells is apply stacks of phosphorus-doped silicon rich / carbon rich films. The properties can be further improved if such stacks are made of phosphorus-doped ternary silicon carbon nitrogen alloys. Therefore, the three main objectives announced above have been accomplished.

7.2 Further work

There are many ideas and experiments that came into my mind (and of course also into my colleagues' minds) during the development of this work. Most of them were simply stored in the draw waiting for "a better occasion", others could not be processed due to the lack of some resources in our modest group, especially when compared to big Institutes that nowadays are really favoured by the expansion of the photovoltaic market. However, it is clear that the contribution of my group has been decisive to introduce silicon carbide for surface passivation in the photovoltaic community. And I strongly believe that this group can still provide interesting ideas, despite we are not alone now with this material and our own surface passivation level has been overcome [164].

The ideal case for silicon carbide would be to find a film that was intrinsic, well-dielectric, with good passivation properties, transparent, resistive to thermal processes, able to solve what silicon nitride has not solved yet (passivation of boron-doped emitters and extinction of field effect passivation due to shunting effects) and, finally, cheap. Of course, it is more than probable that this long list of requirements will never be accomplished due to intrinsic properties of the material. Nevertheless, some interesting ideas that can be developed still by our group are list hereafter:

- Explore the capabilities of surface passivation in all kind of solar grade substrates and development of classical solar cells concepts. Surface passivation of multicrystalline silicon was applied in wafers provided by Fraunhofer Institute, achieving reasonably good results. Screen printed solar cells with passivated n^+-type emitters using stacks were developed at the Australian National University. For both issued we still need further research.

- Investigate the dependence of intrinsic silicon carbide films under high temperatures and compare the results with the behaviour obtained for phosphorus doped films. This could provide useful information about the origin of lifetime recovering explained in section 6.3.1.2.

- Fabrication of n^+-type emitters from the phosphorus doped layer by annealing silicon carbide films (see Ref [162,165,166]) and development of solar cells with such emitters. This process would allow avoiding the use of conventional phosphorus diffusion, which implies stripping the phosphorus glass and etching of the parasitic *p-n* junction grown at the rear side of the wafer. An very interesting option would be perform passivation by thermally-well behaved silicon nitride on one side [106,107] and phosphorus doped silicon carbide on the other side. Anneal and metallization could complete the process.

APPENDIX I

Determination of charge density through corona charge measurements

In Chapters 3 and 4 the Girisch model has been used to evaluate the recombination parameters and the origin of surface passivation. For wafers with resisitivities around 1 Ω cm a charge density of about 3×10^{11} cm^{-2} was predicted and was almost independent of any deposition conditions. On the other hand, it was very dependent on the resistivity of the bulk region, suggesting that the origin of this charge is not a fixed charge, Q_f, but the contribution of a density of states at the interface, Q_{it}. Anyway, the determination of the charge density through lifetime measurements is a very indirect method, since it is based on the fitting of a model that can be incomplete, and it gives only a single value for the charge density that is equal to $Q = Q_f + Q_{it}$. Hence, it would be convenient to confirm or reject the validity of the model with an independent measurement technique.

Corona charge is in principle a suitable technique to work with lifetime test samples because no MIS capacitors are required and light and dark conditions can be analysed. The procedure is normally combined with measurements of the charge using Kelvin probes. This has been applied for the study of SiO_2/*c*-Si interfaces [89], determining that a *fixed* charge $Q_f = 3 \times 10^{11}$ cm^{-2} was present in the SiO_2. Also a *fixed* charge was found for silicon nitride films that was calculated at $Q_f = 2.5 \times 10^{12}$ cm^{-2}, regardless the wafer was under dark or light conditions [99]. Additionally, when those films were annealed at 850 ºC for 20 s the value of the fixed charge decreased to 1.5×10^{12} cm^{-2}.

With the corona instrument electrostatic charge is deposited on top of the wafer by ionizing the atoms of the surrounding atmosphere through a high electric field. The instrument releases CO_3^- or H_3O^+ species in order to deposit negative or positive ions, respectively while determining the lifetime wafer at every step. The experiments here presented were carrier out at the Institut für Solarenergieforschung in Hameln/Emmerthal (ISFH). Lifetime measurements were taken in their commercial µW-PCD instrument. As the corona charge is incorporated the *c*-Si/*a*-SiC_x interface goes from inversion to accumulation. A minimum of passivation is expected when Flat Band (FB) conditions are matched, so that a maximum in the $S_{eff}(Q)$ at a given position Q_{max} should be observed and would indicate the value of the charge density in the *a*-SiC layers under normal conditions, i.e. $Q_{max} = Q_f$.

The charge deposited onto the films is determined by a Kelvin probe. One of the sides is grounded, while the other side is under a vibrating probe that measures contactlessly the voltage between two electrodes. The instrument allows adjusting the potential to zero when no corona charge is deposited, so that the measured potential is directly the surface potential related to the capacity of the film. The capacity of the film has to be measured independently, building a metal-insulator-metal capacitor, usually employing aluminium. The corona charge is then determined through

$$Q_c = CV \tag{6.1}$$

where C is the capacity of the film and V is the surface potential. For more information about corona charge and Kelvin probe techniques see for example reference [167].

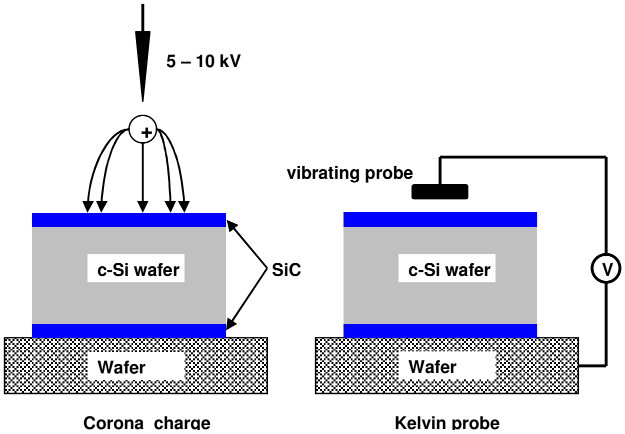

Figure A.1. Schematic of the corona charge and Kelvin probe instruments.

Float zone, double side polished silicon wafers were used for the present experiments with the following doping: *p*-type 0.95 and 6 Ω cm and *n*-type 1 Ω cm. Different approaches were tried for the type of passivation films to be analyzed. A first experiment was tried with phosphorus-doped silicon-rich films, which are of special interest due to their good passivation properties. However, the relatively high conductivity made impossible to change the surface voltage of those films when the corona charge was applied. The problem is similar to leakage currents in capacitors. Therefore, intrinsic carbon rich films with good dielectric properties were prepared. The drawback for using those films is that significant poorer passivation properties are obtained. The films were grown at 300 ºC and a FGA for 20 minutes was applied with the aim to minimize interface state density. Those films exhibited refractive indexes n = 2.0 and a relative dielectric constant, $\varepsilon_r = 5.2$.

Before starting corona charge, lifetime measurements by means of QSS-PC technique were performed on some wafers in order to fit the complete $\tau(\Delta n)$ curve with the Girisch model. Apart from the impossibility to use silicon rich films, other problems were found at the time to apply corona charge. First, a fast light induced degradation of the surface potential was observed. Second, grounding one of the charged sides was necessary to apply corona or to measure the potential of the other side, degrading again the surface potential. The first problem was solved by measuring the lifetime without any white bias light, using only the microwave of the µW-PCD instrument. With this configuration the degradation of the surface potential was slow enough to perform the measurements. The second problem was solved by applying corona charge only to one of the two sides, so that it was not contacted at any step of the experiment. Due to the poor passivation properties that offer the carbon rich films, another set of samples was prepared with asymmetrical structures. In those samples the front side had the carbon rich layer to be analysed, while the rear side was passivated with a silicon rich sample in order to minimize the recombination at this side and to enhance the recombination properties of the front side. The test led to similar qualitative results and, surprisingly, to similar passivation levels.

The experimental lifetime curves with the corresponding fittings for *p*-type wafer passivated with symmetrical depositions are shown in Fig A.2 and A.3 for *p*-type wafers or 0.95 and 6 Ω cm, respectively. All simulated curves are able to reproduce the experimental values very accurately in a very wide injection level range. The Depletion Region Modulation (DRM) effect is manifested in all curves except for the 6 Ω cm wafer passivated by phosphorus-doped silicon-rich films. The simulated values, expressed in Table A.1, evidence that the charge is relatively independent of the deposition conditions for the 0.95 Ω cm wafers, with a value around 3×10^{11} cm^{-2}. This is the same value observed in the whole thesis for this resistivity. On the other hand, for 6 Ω cm wafers it seems to be an influence of the growing conditions, with a higher value of the charge density for the intrinsic SiC films. Concerning the values for the fundamental recombination of holes, they are very dependent on the deposition conditions, indicating again that the improvement of passivation is due to saturation of dangling bonds at the interface, and it is much better when phosphorus-doped, silicon-rich films are used.

The application of corona charge measurements to silicon carbide and silicon nitride leads to different behaviours, as shown in Fig A.4. While in silicon nitride there is a maximum of surface recombination velocity, indicating Flat Band conditions and therefore the value of the fixed charge within the film, for silicon carbide the shape of the curve is a step. This behaviour has been reported for silicon *p*-*n* junctions passivated by SiO_2 [89]. The same trend is observed for *p*-type 6 Ω cm and *n*-type 1 Ω cm wafers (Figure A.5). Such behaviour might indicate that the charge density depends on the Fermi level position, and therefore it could be related to the interface states density, D_{it}. The shape of the step is independent of the doping type, with S_{eff} maximized at the negative region of the $S_{eff} - Q_c$ plot. This suggests that the sign of the effective charge is positive for both doping types.

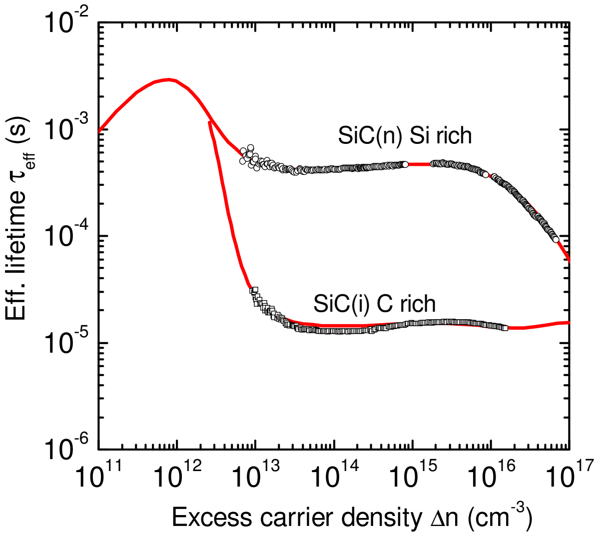

Figure A.2. Experimental and simulated lifetime curves for p-type 0.95 Ω cm wafers passivated by Si-rich phosphorus-doped and C-rich intrinsic films.

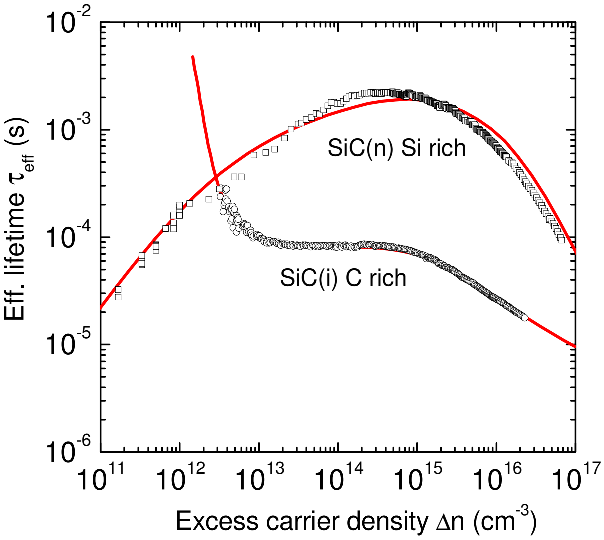

Figure A.3. Experimental and simulated lifetime curves for p-type 6 Ω cm wafers passivated by Si-rich phosphorus-doped and C-rich intrinsic films.

The results on corona charge show another argument in favour of a charge density related to the interface states density. Nevertheless, they have to be taken carefully before more evidences are presented. Concretely, experiments of *C-V* measurements on MIS capacitors are in progress at UPC.

Table A.1 Simulation parameters for samples deposited with different silicon carbide films and annealed in FG for 20 minutes. They correspond to Figures A.2 and .3.

ρ (Ω cm)		Q (× 10^{11} cm^{-2})	S_{p0} (cm^{-2})
0.95	Si rich – *n* doped	2.8	250
	C rich – intrinsic	3.2	14000
6	Si rich – *n* doped	6.8	25
	C rich – intrinsic	12.1	2485

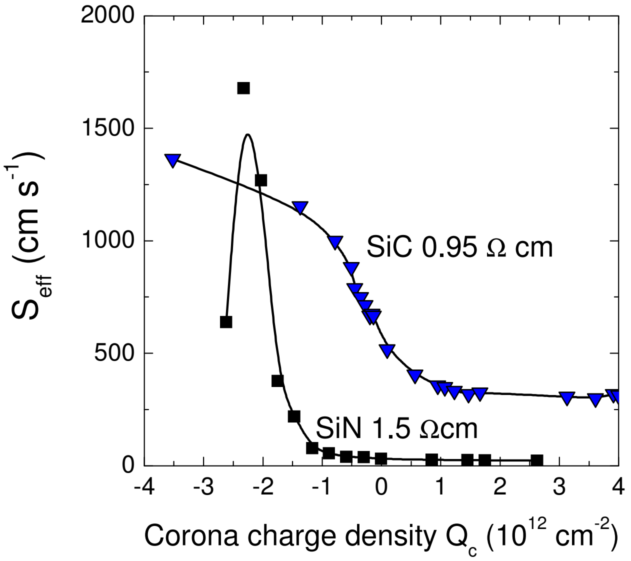

Figure A.4. Corona charge measurents. Comparison between silicon nitride (reference [99]) and silicon carbide (this work).

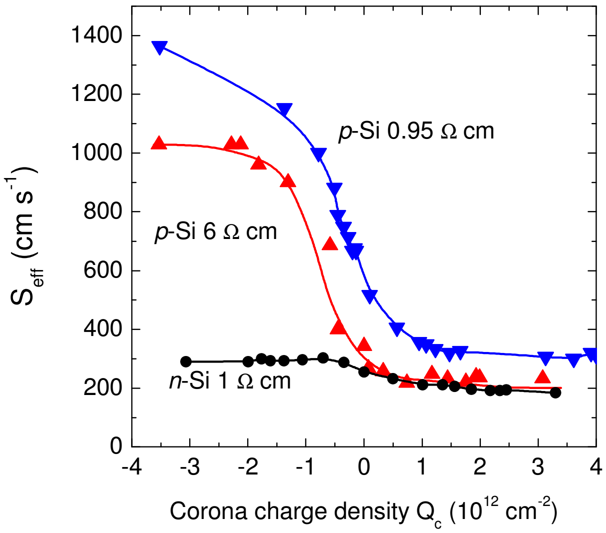

Figure A.5. Corona charge measurements applied to silicon wafers with different resisistivities passivated by C-rich and intrinsic *a*-SiC films.

List of publications

Refereed journal papers

(1) R. Ferre, A. Orpella, D. Munoz, I. Martín, F. Recart, C. Voz, J. Puigdollers, P. Roca, R. Alcubilla, *Very low surface recombination velocity of crystalline silicon passivated by phosphorus-doped* $a\text{-}SiC_xN_y\text{:}H(n)$ *alloys*, Prog. Phot. Res. Appl. (available on-line from Dec. 2007)

(2) R. Ferre, I. Martín, P. Ortega, M. Vetter, I. Torres, R. Alcubilla, *n-type emitter surface passivation in c-Si solar cells by means of antireflective amorphous silicon carbide layers*, J. Appl. Phys. **100**, 073703 (2006)

(3) M. Vetter, C. Voz, R. Ferre, I. Martín, A. Orpella, J. Puigdollers, J. Andreu, R. Alcubilla, *Electronic properties of intrinsic and doped amorphous silicon carbide films*, Thin Solid Films **511**, 290 (2006)

(4) M. Vetter, I. Martín, R. Ferre, M. Garín, and R. Alcubilla, *Crystalline silicon surface passivation by amorphous silicon carbide films*, Sol. En. Mat. Sol. Cells **91**, 174 (2007)

(5) R. Ferre, I Martín, M. Vetter, M. Garín, and R. Alcubilla, *Effect of amorphous silicon carbide layer thickness on the passivation quality of crystalline silicon surface*, Appl. Phys. Lett. **87**, 202109 (2005)

(6) A. Orpella, M. Vetter, R. Ferre, I. Martín, J. Puigdollers, C. Voz, M. Garín, and R. Alcubilla, *Phosphorus-diffused silicon solar cell emitters with plasma enhanced chemical vapor deposited silicon carbide*, Sol. En. Mat. Sol. Cells **87**, 667 (2005)

Conferences

(7) M. Vetter , R. Ferre, I. Martín, and R. Alcubilla, *Dielectric passivation layers for high efficient c-Si solar cells*, Presented at the 22nd European Photovoltaic Solar Energy Conference, Milan, Italy, 3 – 7 Sept 2007, (WIP-Renewable Energies, 2007), p.

(8) R. Ferre, I. Martín, P. Ortega, M. Vetter, M. Garín, and R. Alcubilla, *c-Si surface passivation for photovoltaic applications by means of antireflective amorphous silicon carbide layers*, Proc. 6th Spanish Conference on Electronic Devices, San Lorenzo de El Escorial (Madrid) Spain, 30 Jan – 2 Feb 2007, (IEEE, 2007), p. 238

(9) R. Ferre, I. Martín, M. Vetter, D. Baetzner, J. Tan, A. Cuevas, and R. Alcubilla, *Surface and emitter passivation of crystalline silicon by amorphous silicon carbide: evolution with annealing*, 21st European Photovoltaic Solar Energy Conference and Exhibition, Dresden, 4 – 8 Set. 2006 (WIP-Renewable Energies, 2006), p. 919

(10) R. Petres, J. Libal, T. Buck, R. Kopecek, M. Vetter, R. Ferre, I. Martín, D. Borchert, and P. Fath, *Improvements in the passivation of* p^+*-Si surfaces by PECVD silicon carbide films,* Proc. IEEE 4th World Conference on Photovoltaic Conversion, Hawaii, May 8-12, 2006

(11) M. Vetter, I. Martín, R. Ferre, and R. Alcubilla, *Review on Crystalline Silicon Surface Passivation by Amorphous Silicon Carbide Films*, 15th International Photovoltaic Science and Engineering Conference & Exhibition, Shangai, 10-15 Oct. 2005

(12) R. Petres, J. Libal, R. Kopecek, M. Vetter, R. Ferre, I. Martín, D. Borchert, I. Röver, K. Wambach, and P. Fath, *Passivation of p^+-Surfaces by PECVD silicon carbide films – A Promising Method for industrial silicon solar cell applications*, Technical Digest of the 15th International Photovoltaic Science and Engineering Conference & Exhibition, 10 – 15 October 2005, Shangai (Shangai Scientific and Technical Publishers, Shangai, China, 2005), p. 128

(13) J. Libal, R. Petres, T. Buck, R. Kopecek, G. Hahn, R. Ferre, M. Vetter, I. Martín, K. Wambach, Ingo Roever, and P. Fath, *n-type multicrystalline silicon solar cells: BBr_3-diffusion and passivation of p^+-diffused silicon surfaces*, Proc. 20th European Photovoltaic Solar Energy Conference, Barcelona, 6 – 10 Jun. 2005 (WIP-Renewable Energies, 2005), p.793

(14) D. L. Bätzner, J. Tan, K. Hanton, R. Ferre, D. Macdonald, A. Cuevas, S. Peters, D. H. Neuhaus, and M. Ghosh, *Dependence of phosphorous gettering of multicrystalline silicon on diffusion sheet resistance and ingot position*, Proc. 20th European Photovoltaic Solar Energy Conference, Barcelona, 6 – 10 Jun. 2005 (WIP-Renewable Energies, 2005), p. 655

(15) S. W. Glunz, A. Grohe, M. Hofmann, S. Janz, O. Schultz, M. Vetter, R. Ferre, W. Wolke, W. Warta, R. Preu, and G. Willeke, *Comparison of different dielectric passivation layers for application in industrial feasible silicon high-efficiency cells*, Proc. 20th European Photovoltaic Solar Energy Conference, Barcelona, 6 – 10 Jun. 2005 (WIP-Renewable Energies, 2005), p. 572

(16) R. Ferre, I. Martín, M. Vetter, A. Orpella, and R. Alcubilla, *Influence of RF power on c-Si surface passivation by amorphous a-SiCx:H layers deposited by PECVD*, Electron Devices, 2005 Spanish Conference on, 2 – 4 Feb. 2005, p. 243

(17) M. Vetter, Y. Touati, I. Martín, R. Ferre, R. Alcubilla, J. Alonso, and M. A. Vázquez, *Characterization of Industrial p-type CZ Silicon Wafers Passivated with a-SiCx:H Films*, 5ª Conferencia de Dispositivos Electrónicos, Tarragona, 2 – 4 February 2005 (IEEE, 2005)

(18) M. Vetter, R. Ferre, A. Orpella, I. Martín, J. Puigdollers, C. Voz, and R. Alcubilla, *Development of solar cells solar cells with annealed $a\text{-}Si_{0,8}C_{0,2}/c\text{-}Si$ emitter*, Proc. 19th European Photovoltaic Solar Energy Conference, Paris, 7 – 11 June 2004 (WIP-Renewable Energies, 2004), p. 1189

Bibliography

[1] H. Scheer, *Economía solar global* (Galaxia Gutenberg. Círculo de Lectores, Barcelona, 2000), p. 12 and p. 355. Title of original edition: *Solare Weltwirtschaft*

[2] *El sueño del dinosaurio*, Photon – La revista de fotovoltaica, March (2007), p. 42

[3] J. Zhao, A. Wang, and M. A. Green, *High-efficiency PERL and PERT silicon solar cells on FZ and MCZ substrates*, Sol. En. Mat. Sol. Cells **65**, 429 (2001)

[4] R. M. Swanson, *Approaching the 29% limit efficiency of silicon solar cells*, Proc. Photovoltaic Specialists Conference, 2005. Conference Record of the Thirty-first IEEE, 3-7 Jan. 2005, p. 889

[5] http://rredc.nrel.gov/solar/spectra/

[6] T. Tiedje, E. Yablonovitch, G. D. Cody, and B. G. Brooks, *Limiting Efficiency of Silicon Solar Cells*, IEEE Trans Elec Dev **ED-31** (5), pp. 711 – 716 (1984)

[7] W. Michaelis and M. H. Pilkhun, *Radiative recombination in silicon p-n junctions*, Phys. Stat. Sol. A, **36** (1), pp. 311 – 319, (1969)

[8] H. Schlangenotto, H. Maeder, and W. Gerlach, *Temperature Dependance of the Radiative Recombination Coefficient in Silicon*, Physica Status Solidi A, **21**, 357 (1974)

[9] W. Gerlach, H. Schlangenotto, H. Maeder, *On the radiative recombination rate in silicon*, Physica Status Solidi (a) **13**, 277 (1972)

[10] M. A. Green, *Silicon Solar Cells: Advanced Principles and Practice*, Sydney: UNSW, (1995)

[11] Y. P. Varshni, B*and-to-band radiative recombination in groups IV, VI, and III-V semiconductors (I)*, Physica Status Solidi B **19**, 459 (1967)

[12] W. Michaeli, M. H. Pilkuhn, *Radiative recombination in silicon p-n junctions*, Physica Status Solidi **36**, 311 (1969)

[13] T. Trupke, M. A. Green, P. Würfel, P. P. Altermatt, A. Wang, J. Zhao, and R. Corkish, *Temperature dependence of the radiative recombination coefficient of intrinsic crystalline silicon*, J. Appl. Phys. **94**, 4930 (2003)

[14] P. P. Altermatt, F. Geelhaar, T. Trupke, X. Dai, A. Neisser, and E. Daub, *Injection dependence of spontaneous radiative recombination in crystalline silicon: Experimental verification and theoretical analysis*, Appl. Phys. Lett. **88**, 261901 (2006)

[15] A. Hangleiter and R. Häcker, *Enhancement of band-to-band Auger recombination by electron-hole correlations*, Phys. Rev. Lett. **65**, 215 (1990)

[16] M. S. Tyagi and R. Van Overstraeten, *Minority carrier recombination in heavily-doped silicon*, Solid State Electronics **26**, 577 (1983)

[17] J. Dziewior and W. Schmid, *Auger coefficients for highly doped and highly excited silicon*, Appl. Phys. Lett. **31**, 346 (1977)

[18] J. del Alamo, S. Swirhun, and R. M. Swanson, *Simultaneous measurement of hole lifetime, hole mobility and bandgap narrowing in heavily doped n-type silicon*, International Electron Devices Meeting Technical Digest, Washington (1985), p. 290

[19] S. E. Swirhun, Y. H. Kwark, and R. M. Swanson, *Measurement of electron lifetime, electron mobility and bandgap narrowing in heaviliy doped p-type silicon*, International Electron Devices Meeting Technical Digest, Washington, p. 24 (1986)

[20] P. P. Altermatt, J. Schmidt, G. Heiser, and A. G. Aberle, *Assessment and parameterisation of Coulomb-enhanced Auger recombination coefficients in lowly injected crystalline silicon*, J. Appl. Phys. **82**, 4938 (1997)

[21] S. E. Swirhun, *Characterization of majority and minority carrier transport in. heavily doped silicon*, Ph.D. thesis, Stanford University

[22] P. Jonsson, H. Bleichner, M. Isberg, and E. Nordlander, *The ambipolar Auger coefficient: Measured temperature dependence in electron irradiated and highly injected n-type silicon*, J. Appl. Phys. **81**, 2256 (1997)

[23] P. P. Altermatt, J. Schmidt, M. J. Kerr, G. Heiser, and A. G. Aberle, *Exciton-enhanced Auger recombination in crystalline silicon under intermediate and high injection conditions*,16th European Photvoltaic Solar Energy Conference, Glasgow, Scotland, (2000)

[24] P. P. Altermatt, R. A. Sinton, and G. Heiserc, *Improvements in numerical modelling of highly injected crystalline silicon solar cells*, Sol. En. Mat. Sol. Cells **65**, 149 (2001)

[25] J. Schmidt, M. Kerr, and P. P. Altermatt, *Coulomb-enhanced Auger recombination in crystalline silicon at intermediate and high injection densities*, J. Appl. Phys. **88**, 1494 (2000)

[26] P. A. Basore, PC-1D Install. Manual & User's Guide, Sandia Laboratory Report 91-0516.UC-274, 1992.

[27] M. J. Kerr and A. Cuevas, *General parameterization of Auger recombination in crystalline silicon*, J. Appl. Phys. **91**, 2473 (2002)

[28] M. J. Kerr, PhD thesis, Australian National University (2002)

[29] S. M. Sze, *Physics of semiconductor devices*, John Wiley & Sons, 2nd ed. (1981)

[30] W. Shockley and W.T. Read, *Statistics of the recombinations of holes and electrons*, Phys. Rev. **87**, 935 (1952)

[31] R. N. Hall, *Electron-hole recombination in germanium*, Phys. Rev. **87**, 387 (1952)

[32] I. Martín Thesis. (Universitat Politècnica de Catalunya, Barcelona, 2004)

[33] S. R. Dhariwal, L.S. Kothari and S.C. Jain, *On the recombination of electrons and holes at traps with finite relaxation time*, Solid-State Electr. **24**, 749 (1981)

[34] J. Knobloch, S. W. Glunz, D. Biro, W. Warta, E. Schaffer, and W. Wettling, *Solar cells with efficiencies above 21% processed from Czochalski grown silicon*, Proc. of the 25th IEEE Photovoltaic Specialist Conference, 1996, p. 405

[35] J. Schmidt, A. G. Aberle, and R. Hezel, *Investigation of carrier lifetime instabilities in Cz-grown silicon*, Proc. of the 26th IEEE Photovoltaic Specialist Conference, 1997, p. 13

[36] J. Zhao, A. Wang, and M. A. Green, *Performance degradation in CZ(B) cells and improved stability high efficiency PERT and PERL silicon cells on a variety of SHE MCZ(B), FZ(B) and CZ(Ga) substrates*, Prog. Phot. Res. Appl. **8**, 549 (2000)

[37] A. G. Aberle, S. Glunz, and W. Warta, *Impact of illumination level and oxide parameters on Shockley-Read-Hall recombination at the Si-SiO$_2$ interface*, J. Appl. Phys. **71**, 4422 (1992)

[38] Y. S. Kim, C. I. Drowly and C. Hu, *A new method of measuring diffusion length and surface recombination velocity*, Conf. Record 14th IEEE Photovoltaic Specialists Conference, San Diego, p. 560 (1980).

[39] A. Cuevas and R. A. Sinton, *Prediction of the open-circuit voltage of solar cells from the steady-state photoconductance*, Prog. Photovolt. Res. Appl. **5**, 79 (1997)

[40] M. Shur, *Physics of semiconductor devices*, Prentice Hall, 1990. ISBN 0136664962

[41] I. Martín, M. Vetter, A. Orpella, J. Puigdollers, C. Voz, R. Alcubilla, J. Damon Lacoste, P. Roca i Cabarrocas, *Development of emitters based on a-Si (n^+)/a-Si (i)/ c-Si (p) heterojunctions through lifetime spectroscopy*, Proc. 19th European Photovoltaic Solar Energy Conference, 7-11 June 2004, Paris (WIP-Munich and ETA-Florence, Munich, Germany, 2004), p. 1185

[42] A. G. Aberle, *Crystalline Silicon Solar Cells – Advanced Surface Passivation and Analysis*, (Center for Photovoltaic Engineering, University of New South Wales, Sydney, 1999)

[43] W. Kern and D. A. Puotinen, *Cleaning solutions based on hydrogen peroxide for use in silicon semiconductor technology*, RCA Rev. **31**, 187 (1970)

[44] E. Yablonovitch, D.L. Allara, C.C. Chang, T. Gmitter and T.B. Bright, *Unusually low surface recombination velocity on silicon germanium surfaces*, Phys. Rev. Lett. **57**, 249 (1986)

[45] D. H. Macdonald, A. Cuevas, M. J. Kerr, C. Samundsett, D. Ruby, S. Winderbaum, and A. Leo, *Texturing industrial multicrystalline silicon solar cells*, Solar Energy **76**, 277 (2004)

[46] M. Schnell, R. Ludemann, and S. Schaefer, *Plasma surface texturization for multicrystalline silicon solar cells*, Proc. Photovoltaic Specialists Conference, 2000. Conference Record of the Twenty-Eighth IEEE, Anchorage, AK, USA (IEEE, 2000), p. 367

[47] I. Martín, M. Vetter, A. Orpella, C. Voz, J. Puigdollers, R. Alcubilla, A. V. Kharchenko, and P. Roca i Cabarrocas, *Improvement of crystalline silicon surface passivation by hydrogen plasma treatment*, Appl. Phys. Lett. **84**, 1474 (2004)

[48] H. Nagel, C. Berge, and A. G. Aberle, *Generalized analysis of quasi-steady-state and quasi-transient measurements of carrier lifetimes in semiconductors*, J. Appl. Phys. **86**, 6218 (1999)

[49] M. S. Tyagi, J. F. Nijs, and R. J. Van Overstraeten, *Effect of surface recombination velocity on the transient decay of excess carriers produced by short-wavelength laser pulses*, Solid-State Electron. **25**, 411 (1982)

[50] J. Brody, A. Rohatgi, and A. Ristow, *Review and comparison of equations relating bulk lifetime and surface recombination velocity to effective lifetime measured under flash lamp illumination*, Sol. En. Mat. Sol. Cells **77**, 293 (2003)

[51] G.D. Masseti, M. Severi and S. Solmi, *Modeling of carrier mobility against carrier concentration in arsenic-, phosphorus- and boron-doped silicon*, IEEE Trans. Electron Dev. **ED-30**, 764 (1983)

[52] F. Dannhäuser, *Die abhangigkeit der tragerbeweglichkeit in silizium von der konzentration der freien ladungstrager-I*, Solid-State Elec. **15**, 1371 (1972)

[53] J. Krause, *Die abhangigkeit der tragerbeweglichkeit in silizium von der konzentration der freien ladungstrager-II*, Solid-State Elec. **15**, 1577 (1972)

[54] D. B. M. Klaassen, *A unified mobility model for device simulation-I. Model equations and concentration dependence*, Solid-State Elec. **35**, 953 (1992)

[55] S. Yamakawa, H. Ueno, K. Taniguchi, C. Hamaguchi, K. Miyatsuji, K. Masaki, and U. Ravaioli, *Study of interface roughness dependence of electron mobility in Si inversion layers using the Monte Carlo method*, J. Appl. Phys. **79**, 911 (1996)

[56] J. R. Elmiger and M. Kunst, *Investigation of charge carrier injection in silicon nitride/silicon junctions*, App. Phys. Lett. **69,** 517 (1996)

[57] D. T. Stevenson and R. J. Keyes, *Measurement of Carrier Lifetimes in Germanium and Silicon*, J. Appl. Phys. **26**, 190 (1955)

[58] S. Deb and B. R. Nag, *Measurement of Lifetime of Carriers in Semiconductors through Microwave Reflection*, J. Appl. Phys. **33**, 1604 (1962)

[59] M. Kunst and G. Beck, *The study of charge carrier kinetics in semiconductors by microwave conductivity measurements*, J. Appl. Phys. **60**, 3558 (1986)

[60] J. Schmidt and A.G. Aberle, *Accurate method for the determination of bulk minority-carrier lifetimes of mono- and multicrystalline silicon wafers*, J. Appl. Phys. **81**, 6186 (1997)

[61] S. W. Glunz, A. B. Sproul, W. Warta, and W. Wettling, *Injection-level-dependent recombination velocities at the Si-SiO$_2$ interface for various dopant concentrations*, J. Appl. Phys. **75**, 1611 (1994)

[62] J. Schmidt, T. Lauinger, A.G. Aberle and R. Hezel, *Light-biased phtoconductance decay measurements on silicon-nitride passivated silicon surfaces*, Proc. 13th European Photovoltaic Solar Energy Conference, Nice, France, p. 1287 (1995)

[63] T. Maekawa and Y. Shima, *Effect of steady bias light on carrier lifetime in silicon wafers with chemically passivated surfaces*, Jpn. J. Appl. Phys. **35**, L133 (1996)

[64] A. W. Stephens and M.A. Green, *Effectiveness of 0.08 molar iodine in ethanol solution as a means of chemical surface passivation for photoconductance decay measurements*, Sol. En. Mat. Sol. Cells **45**, 255 (1997)

[65] P. A. Basore and B.R. Hansen, *Microwave-detected photoconductance decay*, Proc. 21st IEEE Photovoltaic Specialists Conference, Orlando, p. 374 (1990)

[66] R. Brendel, *Note on the interpretation of injection level dependent surface recombination velocities*, Appl. Phys. A **60**, 523 (1995)

[67] J. Schmidt, *Measurement of differential and actual recombination parameters on crystalline silicon wafers*, IEEE Trans. Electron Dev. **ED-46**, 2018 (1999)

[68] R. A. Sinton and A. Cuevas, *Contactless determination of current–voltage characteristics and minority-carrier lifetimes in semiconductors from quasi-steady-state photoconductance data*, Appl. Phys. Lett. **69**, 2510 (1996)

[69] http://www.sintonconsulting.com

[70] J. Schmidt, *Temperature- and injection-dependent lifetime spectroscopy for the characterization of defect centers in semiconductors*, Appl. Phys. Lett. **82**, 2178 (2003)

[71] J. A. Hornbeck and J.R. Haynes, *Trapping of Minority Carriers in Silicon. I. P-Type Silicon*, Phys. Rev. **97**, 311 (1955)

[72] H.Y. Fan, *Effect of traps on carrier injection in semiconductors*, Phys. Rev. **92**, 1424 (1953)

[73] D. Macdonald and A. Cuevas, *Trapping of minority carriers in multicrystalline silicon*, Appl. Phys. Lett. **74**, 1710 (1999)

[74] A. Cuevas, M. Stocks, D. Macdonald, M. Kerr, and C. Samundsett, *Recombination and trapping in multicrystalline silicon*, IEEE Trans. Electron Dev. **46**, 2026 (1999)

[75] R. A. Sinton, *Possibilities for process-control monitoring of electronic material properties during solar-cell manufactur*e, Proc. 9th Workshop Role of Impurities and Defects in Silicon Device Processing, Golden, Colorado, p. 67 (1999)

[76] D. Macdonald, R. A. Sinton, and A. Cuevas, *On the use of a bias-light correction for trapping effects in photoconductance-based lifetime measurements of silicon*, J. Appl. Phys. **89**, 2772 (2001)

[77] M. Bail, M. Schulz, and R. Brendel, *Space-charge region-dominated steady-state photoconductance in low-lifetime Si wafers*, Appl. Phys. Lett. **82**, 757 (2003)

[78] D. H. Neuhaus, P. J. Cousins, and A. G. Aberle, *Trapping and junction-related perturbations of the effective excess carrier lifetime*, Proc. 3rd World Conference on Photovoltaic Energy Conversion, 11 – 18 May 2003, Osaka (IEEE, 2003)

[79] P. J. Cousins, D. H. Neuhaus, and J. E. Cotter, *Experimental verification of the effect of depletion-region modulation on photoconductance lifetime measurements*, J. Appl. Phys. **95**, 1854 (2004)

[80] M. Garin, I. Martín, S. Bermejo, and R. Alcubilla, *Fixed charge density in dielectrics deposited on c-Si using space charge region dominated lifetime measurements*, J. Appl. Phys. **101**, 123716 (2007)

[81] T. Trupke, R. A. Bardos, F. Hudert, P. Würfel, A. Wang, J. Zhao, and M. A. Green, *Effective excess carrier lifetimes exceeding 100 milliseconds in Float Zone silicon determined from photoluminescence*, Proc. 19th European Photovoltaic Solar Energy Conference, 7 – 11 June 2004, Paris (WIP-Munich and ETA-Florence, Munich, Germany, 2004), p. 758

[82] T. Trupke, R. A. Bardos, M. D. Abbott, and J. E. Cotter, *Suns-Photoluminescence: Contactless determination of current-voltage characteristics of silicon wafers*, Appl. Phys. Lett. **87**, 093503 (2005)

[83] R. A. Bardos, T. Trupke, M. C. Schubert, and T. Roth, *Trapping artifacts in quasi-steady-state photoluminescence and photoconductance lifetime measurements on silicon wafers*, Appl. Phys. Lett. **88**, 053504 (2006)

[84] A. S. Grove and D. J. Fitzgerald, *Surface effects on p-n junctions: characteristics of surface space-charge regions under non-equilibrium conditions*, Solid-State Electr. **9**, 783 (1968)

[85] D. J. Fitzgerald and A. S. Grove, *Surface recombination in semiconductors*, Surf. Sci. **9**, 347 (1968)

[86] R. B. M. Girisch, R. P. Mertens, and R. F. Keersmaecker, *Determination of Si-SiO$_2$ interface recombination parameters using a gate-controlled point-junction diode under illumination*, IEEE Trans. Electron Dev. **35**, 203 (1988)

[87] J. Brody and A. Rohatgi, *Analytical approximation of effective surface approximation velocity of dielectric-passivated p-type silicon*, Solid-State Electr. **45**, 1549 (2001)

[88] B.E. Deal and A. S. Grove, *General Relationship for the Thermal Oxidation of Silicon*, J. Appl. Phys **36**, 3770 (1965)

[89] S. W. Glunz, D. Biro, S. Rein, and W. Warta, *Field-effect passivation of the SiO_2-Si interface*, J. Appl. Phys. **86**, 683 (1999)

[90] H. Sai, R. Imai, N. Yamamoto, T. Ishiwata, K. Arafune, Y. Ohshita, and M. Yamaguchi, *Surface recombination at Si/SiO2 interface with various interface state densities and oxide charges*, Proc. 21st European Photovoltaic Solar Energy Conference, 3 – 6 September 2006, Dresden, Germany, (WIP-Renewable Energies Munich, Germany, 2006), p. 915

[91] P. E. Gruenbaum, J. Y. Gan, R. R. King and R. M. Swanson, *Stable passivation for high-efficiency silicon solar cells*, Proc. 21st IEEE Photovoltaic Specialist Conference, Orlando, p. 317 (1990)

[92] A. W. Stephens, A. G. Aberle, and M. A. Green, *Surface recombination velocity measurements at the silicon-silicon dioxide interface by microwave-detected photoconductance decay*, J. Appl. Phys. **76**, 363 (1994)

[93] R. R. King, R. A. Sinton, R. M. Swanson, *Low surface recombination velocities on doped silicon and their applications for point contact solar cells*, Proc. 19th IEEE Photovoltaic Specialist Conference, New Orleans, (1987), p. 1168

[94] P. P. Altermatt, H. Plagwitz, R. Bock, J. Schmidt, R. Brendel, M. J. Kerr, and A. Cuevas, *The surface recombination velocity at boron-doped emitters: comparison between various passivation techniques*, Proc. 21st European Photovoltaic Solar Energy Conference, 3 – 6 September 2006, Dresden, Germany, (WIP-Renewable Energies Munich, Germany, 2006), p. 647

[95] B. Hoex, F. J. J. Peeters, M. Creatore, M. A. Blauw, W. M. M. Kessels, and M. C. M. van de Sanden, *High-rate plasma-deposited SiO2 films for surface passivation of crystalline silicon* J. Vac. Sci. Technol. A **24**, 1823 (2006)

[96] J. Zhao, A. Wang, P. Altermatt, and M. A. Green*, Twenty-four percent efficient silicon solar cells with double layer antireflection coatings and reduced resistance loss*, Appl. Phys. Lett. **66**, 3636 (1995)

[97] M. Vetter, C. Voz, R. Ferre, I. Martin, A. Orpella, J. Puigdollers, J. Andreu and R. Alcubilla, *Electronic properties of intrinsic and doped amorphous silicon carbide films*, Thin Solid Films **511**, 290 (2006)

[98] A. G. Aberle, *Overview on SiN surface passivation of crystalline silicon solar cells*, Sol. En. Mat. Sol. Cells **65**, 239 (2001)

[99] S. Dauwe, J. Schmidt, A. Metz, and R. Hezel, *Fixed charge density in silicon nitride films on crystalline silicon surfaces under illumination*, Photovoltaic Specialists Conference, 2002. Conference Record of the Twenty-Ninth IEEE, 19 – 24 May 2002, p. 162

[100] J. Y. Lee and S. W. Glunz, *Investigation of various surface passivation schemes for silicon solar cells*, Sol. En. Mat. Sol. Cells **90**, 82 (2006)

[101] A. Rohatgi, P. Doshi, J. Moschner, T. Lauinger, A.G. Aberle and D.S. Rudy, *Comprehensive study of rapid, low-cost silicon surface passivation technologies*, IEEE Trans. Electron Dev. **47**, 987 (2000)

[102] H. Jin, K. J. Weber, and A. W. Blakers, *Silicon/silicon oxide/LPCVD silicon nitride stacks: the effect of oxide thickness on bulk damage and surface passivation*, Proc. 20th European Photovoltaic Solar Energy Conference, 6 – 10 June 2005, Barcelona, Spain, (WIP-Renewable Energies Munich, Germany, 2005), p. 230

[103] M. Vetter, *Surface passivation of silicon by rf magnetron-sputtered silicon nitride films*, Thin Solid Films **337**, 118 (1999)

[104] M. Vetter, M. Rojahn, *Properties of amorphous Si-rich silicon nitride prepared by rf-magnetron sputtering*, Mat. Sci. Eng. B **71**, 321 (2000)

[105] W. Wolke, J. Catoir, R. Preu, G. Emanuel, J. Liu, and M. Ruske, *Surface passivation for solar cells by large scale inline sputtering of silicon nitride*, Proc. 20th European Photovoltaic Solar Energy Conference, 6 – 10 June 2005, Barcelona, Spain, (WIP-Renewable Energies Munich, Germany, 2005), p. 733

[106] S. Winderbaum, A. Cuevas, F. Chen, J. Tan, K. Hanton, D. Macdonald, and K. Roth, *Industrial pecvd silicon nitride: surface and bulk passivation of silicon*, Proc. 19th European Photovoltaic Solar Energy Conference, 7 – 11 June 2004, Paris, France, (WIP-Renewable Energies Munich, Germany, 2004), p. 576

[107] J. Schmidt, J. D. Moschner, J. Henze, S. Dauwe and R. Hezel, *Recent progress in the surface passivation of silicon solar cells using silicon nitride*, Proc. 19th European Photovoltaic Solar Energy Conference, 7 – 11 June 2004, Paris, France, (WIP-Renewable Energies Munich, Germany, 2004), p. 391

[108] F. W. Chen, J. E. Cotter, A. Cuevas, S. Winderbaum, and K. Roth, *Anomalous thermal behaviour of surface passivation by PECVD silicon nitride on p-type crystalline silicon*, Proc. 20th European Photovoltaic Solar Energy Conference, 6 – 10 June 2005, Barcelona, Spain, (WIP-Renewable Energies Munich, Germany, 2005), p. 1419

[109] M. Schaper, J. Schmidt, H. Plagwitz, R. Brendel, *20.1%-efficient crystalline silicon solar cell with amorphous silicon rear-surface passivation*, Prog. Phot. Res. Appl. **13**, 381 (2005)

[110] D. Muñoz, C. Voz, I. Martin, A. Orpella, J. Puigdollers, R. Alcubilla, F. Villar, J. Bertomeu, J. Andreu, J. Damon-Lacoste, and P. Roca i Cabarrocas, *Progress in a-Si:H / c-Si heterojunction emitters obtained by Hot-Wire CVD at 200 ºC*, Thin Solid Films **516**, 761 (2008)

[111] R. A. Street, J. Kakalios, C. C. Tsai and T. M. Hayes, *Thermal-equilibrium processes in amorphous silicon*, Phys. Rev. B **35**, 1316 (1987)

[112] B. Hoex, W. M. M. Kessels, M. D. Bijker, and M. C. M. van de Sanden, *Excellent surface passivation by hydrogenated amorphous silicon deposited at rates > 1 nm/s by the Expanding Thermal Plasma technique*, Proc. 21st European Photovoltaic Solar Energy Conference, 3 – 6 September 2006, Dresden, Germany, (WIP-Renewable Energies Munich, Germany, 2006), p. 576

[113] H. Plagwitz, Y. Takahashi, B. Terheiden, R. Brendel, *Amorphous Si/SiN double layer: A low-temperature passivation method for diffused phosphorus as well as boron emitters*, Proc. 21st European Photovoltaic Solar Energy Conference, 3 – 6 September 2006, Dresden, Germany, (WIP-Renewable Energies Munich, Germany, 2006), p. 688

[114] M. Tanaka, S. Okamoto, S. Tsuge, and S. Kiyama, *Development of HIT solar cells with more than 21% conversion efficiency and commercialization of highest performance HIT modules*, Proc. 3rd World Conference on Photovoltaic Energy Conversion, 11 – 18 May 2003, Osaka (IEEE, 2003), p. 955

[115] I. Martín, M. Vetter, A. Orpella, J. Puigdollers, A. Cuevas, and R. Alcubilla, *Surface passivation of p-type crystalline Si by plasma enhanced chemical vapor deposited amorphous* SiC_x*:H films*, Appl. Phys. Lett. **79**, 2199 (2001)

[116] I. Martín, M. Vetter, A. Orpella, C. Voz, J. Puigdollers, and R. Alcubilla, Proc. 17th European Photovoltaic Solar Energy Conference, Munich, Germany, 2001 (Mani Fotolito, Florence, 2002) p. 2954

[117] R. Petres, J. Libal, T. Buck, R. Kopecek, M. Vetter, R. Ferre, I. Martín, D. Borchert, P. Fath, *Improvements in the passivation of p^+-Si surfaces by PECVD silicon carbide films*, Proc. IEEE 4th World Conference on Photovoltaic Conversion, Hawaii, May 8-12 (2006)

[118] U. Coscia, G. Ambrosone, P. Rava, P. Rivolo, F. Ferrazza, L. Serenelli, S. De Iuliis, and M. Tuci, *Surface passivation of p- and n-type crystalline silicon wafers by SiN_x/a-SiC_x:H layers*, Proc. 21st European Photovoltaic Solar Energy Conference, 3 – 6 September 2006, Dresden, Germany, (WIP-Renewable Energies Munich, Germany, 2006), p. 1623

[119] R. Ferre, I. Martín, P. Ortega, M. Vetter, M. Garín, and R. Alcubilla, *c-Si surface passivation for photovoltaic applications by means of antireflective amorphous silicon carbide layers*, 6th Spanish Conference on Electronic Devices, San Lorenzo de El Escorial (Madrid) Spain, 30 Jan – 2 Feb 2007, p. 238

[120] J. Libal, R. Petres, T. Buck, R. Kopecek, G. Hahn, R. Ferre, M. Vetter, I. Martín, K. Wambach, I. Roever, P. Fath, Proc. 20th European Photovoltaic Solar Energy Conference, Barcelona, Spain, 2005 (WIP-Renewable Energies, 2005), p. 793

[121] R. Petres, J. Libal, R. Kopecek, M. Vetter, R. Ferre, I. Martín, D. Borchert, I. Röver, K. Wambach, and P. Fath, *Passivation of p^+-Surfaces by PECVD silicon carbide films – A Promising Method for industrial silicon solar cell applications*, Technical Digest of the 15th International Photovoltaic Science and Engineering Conference & Exhibition, 10 – 15 October 2005, Shangai (Shangai Scientific and Technical Publishers, Shangai, China, 2005), p. 128

[122] F. Duerinckx and J. Szlufcik, *Defect passivation of industrial multicrystalline solar cells based on PECVD silicon nitride*, Sol. En. Mat. Sol. Cells **72**, 231 (2002)

[123] N. Do, L. Klees, P. T. Leung, F. Tong, and W. P. Leung, *Temperature dependence of optical constants for amorphous silicon* Appl. Phys. Lett. **60**, 2186 (1992)

[124] R. J. Severens, G. J. H. Brussaard, M. C. M. van de Sanden, and D. C. Schram, *Characterization of plasma beam deposited amorphous hydrogenated silicon.* Appl. Phys. Lett. **67**, 491 (1995)

[125] A. H. M. Smets, D. C. Schram, and M. C. M. van de Sanden, *In situ single wavelength ellipsometry studies of high rate hydrogenated amorphous silicon growth using a remote expanding thermal plasma*, J. Appl. Phys. **88**, 6388 (2000)

[126] A. Fontcuberta i Morral and P. Roca i Cabarrocas, *Structure and hydrogen content of polymorphous silicon thin films studied by spectroscopic ellipsometry and nuclear measurements*, Physical Review B **69**, 125307 (2004)

[127] R. M. Young and W. D. Partlow, *Amorphous silicon, amorphous carbon and amorphous silicon carbide deposited by remote chemical vapor deposition*, Thin solid films **213**, 170 (1992)

[128] F. W. Smith, *Optical properties and local atomic bonding in hydrogenated amorphous carbon and silicon-carbon alloys*, Mat. Sci. Forum **52**, 323 (1990)

[129] M. Vetter, I. Martín, A. Orpella, C. Voz, J. Puigdollers, and R. Alcubilla, *Characterization of a-SiC_x:H films for c-Si surface passivation*, Mat. Res. Soc. Sym. Proc. **715**, 539 (2002)

[130] G. E. Jellison, Jr. and F. A. Modine, *Parameterization of the optical functions of amorphous materials in the interband region*, Appl. Phys. Lett. **69,** 371 (1996)

[131] D. Daineka, V. Suendo, and P. Roca i Cabarrocas, *Temperature dependence of the optical functions of amorphous silicon-based materials: application to in situ temperature measurements by spectroscopic ellipsometry*, Thin Solid Films **468**, 298 (2004)

[132] S. Dauwe, L. Mittelstädt, A. Metz, and R. Hezel, *Experimental evidence of parasitic shunting in silicon nitride rear surface passivated solar cells*, Prog. Phot. Res. Appl. **10**, 271 (2002)

[133] M. Vetter, R. Ferre, I. Martín, and R. Alcubilla, *Dielectric passivation layers for high efficient c-Si solar cells*, Presented at the 22nd European Photovoltaic Solar Energy Conference, Milan, Italy, 2007, (WIP Renewable Energies, 2007), p.

[134] S. W. Glunz, A. Grohe, M. Hofmann, S. Janz, O. Schultz, M. Vetter, R. Ferre, W. Wolke, W. Warta, R. Preu, and G. Willeke, *Comparison of different dielectric passivation layers for application in industrial feasible silicon high-efficiency cells*, Proc. 20th European Photovoltaic Solar Energy Conference, Barcelona, 6- 10 Jun. 2005 (WIP-Renewable Energies), p. 572

[135] D. Macdonald and A. Cuevas, *The trade-off between phosphorus gettering and thermal degradation in multicrystalline silicon*, Proc. 16th European Photovoltaic Solar Energy Conference, 1 – 5 May 2000, Glasgow, (James & James, London, UK, 2000), p. 1707

[136] O. Schultz, S. W. Glunz, and G. P. Willeke, *Multicrystalline silicon solar cells exceeding 20% efficiency*, Prog. Phot. Res. Appl. **12**, 553 (2004)

[137] O. Schultz, S. W. Glunz, J. C. Goldschmidt, H. Lautenschlager, A. Leimenstoll, E. Schneiderlöchner, and G. P. Willeke, *Thermal oxidation processes for high-efficiency multicrystalline silicon solar cells*, Proc. 19th European Photovoltaic Solar Energy Conference, 7 – 11 June 2004, Paris (WIP-Munich and ETA-Florence, Munich, Germany, 2004), p. 604

[138] M. J. Kerr, J. Schmidt, A. Cuevas, J. H. Bultman, *Surface recombination velocity of phosphorus-diffused silicon solar cell emitters passivated with plasma enhanced chemical vapor deposited silicon nitride and thermal silicon oxide*, J. Appl. Phys. **89**, 3821 (2001)

[139] A. G. Aberle and R. Hezel, *Progress in Low-temperature Surface Passivation of Silicon Solar Cells using Remote-plasma Silicon Nitride*, Prog. Phot. Res. Appl. **5**, 29 (1997)

[140] B. Lenkeit, T. Lauinger, A. G. Aberle, and R. Hezel, *Comparison of remote versus direct PECVD silicon nitride passivation of phosphorus-diffused emitters of silicon solar cells*, Proc. 2nd World Conference on Photovoltaic Solar Energy Conversion, 6–10 July 1998, Vienna (EC Joint Research Center, Ispra, Italy), p. 1434

[141] J. D. Moschner, J. Henze, J. Schmidt, and R. Hezel, *High-quality surface passivation of silicon solar cells in an industrial-type inline plasma silicon nitride deposition system*, Prog. Photovoltaics **12**, 21 (2004)

[142] www.bn.saint-gobain.com. N-Type Planar Diffusion Source (PDS) products technical data PDS planar solid diffusion sources phosphorus

[143] P. Ortega, M. Vetter, S. Bermejo, I. Torres, and R. Alcubilla, *Injection-Dependent Lifetime Spectroscopy and PC-1D simulations of phosphorus emitters doped with solid diffusion sources*, Proc. 20th European Photovoltaic Solar Energy Conference, 6 – 10 June 2005, Barcelona (WIP-Renewable Energies, Munich, Germany, 2005), p. 1228

[144] L. M. Castañer, P. Ashburn, L. Prat, and G. R. Wolstenholme, *The asymptotes of the base current in bipolar devices* IEEE Trans. Electron Dev. **35**, 1902 (1988)

[145] R. Alcubilla and J. Pons, Solid-State Electron. **34**, 1001 (1991)

[146] R. E. I. Schropp and M. Zeman. *Amorphous and microcrystalline silicon solar cells. Modeling, materials and device technology*, Kluwer Academic Publishers, The Netherlands, 1998, p. 156

[147] B. S. Richards, *Single-material TiO_2 double-layer antireflection coatings*, Sol. En. Mat. Sol. Cells **79**, 369 (2003)

[148] I. Martín, M. Vetter, A. Orpella, C. Voz, J. Puigdollers, and R. Alcubilla, *Surface passivation of n-type crystalline Si by plasma-enhanced-chemical-vapor-deposited amorphous SiC_x:H and amorphous SiC_xN_y:H films*, Appl. Phys. Lett. **81**, 4461 (2002)

[149] I. Martín, M. Vetter, M. Garín, A. Orpella, C. Voz, J. Puigdollers, and R. Alcubilla, *Crystalline silicon surface passivation with amorphous SiCx:H films deposited by plasma-enhanced chemical-vapor deposition*, J. Appl. Phys. **98**, 114912 (2005)

[150] R. Ferre, I. Martín, M. Vetter, D. Baetzner, J. Tan, A. Cuevas, and R. Alcubilla, *Surface and emitter passivation of crystalline silicon by amorphous silicon carbide: evolution with annealing*, Proc. 21th European Photovoltaic Solar Energy Conference and Exhibition, Dresden, Germany, 2006, (WIP-Renewable Energies, 2006), p. 919.

[151] W. J. Choyke, H. Matsunami, and G. Pensl, *Silicon Carbide: Recent Major Advances* (Springer, Berlin, 2004), p. 163

[152] Y. Huang, A. Dasgupta, A. Gordijn, F. Finger, and R. Carius, *Highly transparent microcrystalline silicon carbide grown with hot wire chemical vapor deposition as window layers in n-i-p microcrystalline silicon solar cells*, Appl. Phys. Lett. **90**, 203502 (2007)

[153] A. J. Abu El-Haija, *Effective medium approximation for the effective optical constants of a bilayer and a multilayer structure based on the characteristic matrix technique*, J. Appl. Phys. **93**, 2590 (2003)

[154] S. Adachi, *Calculation model for the optical constants of amorphous semiconductors*, J. Appl. Phys. **70**, 2304 (1991)

[155] M. Fried and T. Lohner, *Determination of complex dielectric functions of ion implanted and implanted-annealed amorphous silicon by spectroscopic ellipsometry*, J. Appl. Phys. **71**, 5260 (1992)

[156] B. Lenkeit, S. Steckemetz, F. Artuso, R. Hezel, *Excellent thermal stability of remote plasma-enhanced chemical vapour deposited silicon nitride flms for the rear of screen-printed bifacial silicon solar cells*, Sol. En. Mat. Sol. Cells **65**, 317 (2001)

[157] http://www.wepcontrol.com/cv-profiler/

[158] K. Peter, E. Enebakk, K. Friestad, R. Tronstad, and C. Dethloff, *Investigation of multicrystalline silicon solar cells from solar grade silicon feedstock*, Proc. 20th European Photovoltaic Solar Energy Conference, Barcelona, Spain, 2005 (WIP-Renewable Energies, 2005), p. 615

[159] V. M. Fthenakis and H. C. Kim, *Quantifying the life-cycle environmental profile of photovoltaics and comparisons with other electricity-generating technologies*, Proc. IEEE 4th World Conference on Photovoltaic Conversion, Hawaii, May 8-12 (2006)

[160] K. Nakayashiki, V. Meemongkolkiat, and A. Rohatgi, *High efficiency screen-printed EFG Si solar cells through rapid thermal processing-induced bulk lifetime enhancement*, Prog. Phot. Res. Appl. **13**, 17 (2005)

[161] H. Plagwitz, PhD Thesis, University of Hannover, 2007

[162] A. Orpella, M. Vetter, R. Ferre, I. Martín, J. Puigdollers, C. Voz, M. Garín, and R. Alcubilla, *Phosphorus-diffused silicon solar cell emitters with plasma enhanced chemical vapor deposited silicon carbide*, Sol. En. Mat. Sol. Cells **87**, 667 (2005)

[163] D. H. Macdonald, L. J. Geerligs, and A. Azzizi, *Iron detection in crystalline silicon by carrier lifetime measurements for arbitrary injection and doping*, J. Appl. Phys. **95**, 1021 (2004)

[164] S. Janz, S. Riepe, M. Hofmann, S. Reber, and S. Glunz, *Phosphorus-doped SiC as an excellent p-type Si surface passivation layer*, Appl. Phys. Lett. **88**, 133516 (2006)

[165] A. Orpella, D. Bardes, R. Alcubilla, L. F. Marsal, J. Pallares, *In situ-doped amorphous* $Si_{0.8}C_{0.2}$ *emitter bipolar transistors*, IEEE Electron Dev. Lett. IEEE **20**, 592 (1999)

[166] A. Orpella, D. Bardés, R. Alcubilla, L. F. Marsal, J. Pallarès, *Fabrication and characterization of in situ-doped a-*$Si_{0.8}C_{0.2}$ *emitter bipolar transistors*, Solid-State Electron. **44**, 1543 (2000)

[167] D. K. Schroder, *Surface voltage and surface photovoltage: history, theory and applications*, Meas. Sci. Technol. **12**, R16 (2001)